ORTA DOĞU TEKNİK ÜNİVERSİTESİ
FEN BİLİMLERİ ENSTİTÜSÜ MÜDÜRLÜĞÜ

TEZ ŞABLONU ONAY FORMU
THESIS TEMPLATE CONFIRMATION FORM

1. Şablonda verilen yerleşim ve boşluklar değiştirilmemelidir.
2. **Jüri tarihi** Başlık Sayfası, İmza Sayfası, Abstract ve Öz'de ilgili yerlere yazılmalıdır.
3. İmza sayfasında jüri üyelerinin unvanları doğru olarak yazılmalıdır. Tüm imzalar **mavi pilot kalemle** atılmalıdır.
4. **Disiplinlerarası** programlarda görevlendirilen öğretim üyeleri için jüri üyeleri kısmında tam zamanlı olarak çalıştıkları anabilim dalı başkanlığının ismi yazılmalıdır. Örneğin: bir öğretim üyesi Biyoteknoloji programında görev yapıyor ve biyoloji bölümünde tam zamanlı çalışıyorsa, İmza sayfasına biyoloji bölümü yazılmalıdır. İstisnai olarak, disiplinler arası program başkanı ve tez danışmanı için disiplinlerarası program adı yazılmalıdır.

5. Tezin **son sayfasının sayfa** numarası Abstract ve Öz'de ilgili yerlere yazılmalıdır.
6. Bütün chapterlar, referanslar, ekler ve CV sağ sayfada başlamalıdır. Bunun için **kesmeler** kullanılmıştır. **Kesmelerin kayması** fazladan boş sayfaların oluşmasına sebep olabilir. Bu gibi durumlarda paragraf (¶) işaretine tıklayarak kesmeleri görünür hale getirin ve yerlerini **kontrol edin**.
7. Figürler ve tablolar kenar boşluklarına taşmamalıdır.
8. Şablonda yorum olarak eklenen uyarılar dikkatle okunmalı ve uygulanmalıdır.

9. Tez yazdırılmadan önce PDF olarak kaydedilmelidir. Şablonda yorum olarak eklenen uyarılar PDF dokümanında yer almamalıdır.
10. **Bu form aracılığıyla oluşturulan PDF dosyası arkalı-önlü baskı alınarak tek bir spiralli cilt haline getirilmelidir.**
11. Spiralli hale getirilen tez taslağınızdaki ilgili alanları imzalandıktan sonra, Tez Juri Atama Formu ile birlikte bölüm sekreterliğine teslim edilmelidir.

12. Tez taslaklarının kontrol işlemleri tamamlandığında, bu durum öğrencilere METU uzantılı öğrenci e-posta adresleri aracılığıyla duyurulacaktır.
13. Tez yazım süreci ile ilgili herhangi bir sıkıntı yaşarsanız, **Sıkça Sorulan Sorular (SSS)** sayfamızı ziyaret ederek yaşadığınız sıkıntıyla ilgili bir çözüm bulabilirsiniz.

1. Do not change the spacing and placement in the template.
2. Write **defense date** to the related places given on Title page, Approval page, Abstract and Öz.
3. Write the titles of the examining committee members correctly on Approval Page. **Blue ink** must be used for all signatures.
4. For faculty members working in **interdisciplinary programs**, the name of the department that they work full-time should be written on the Approval page. For example, if a faculty member staffs in the biotechnology program and works full-time in the biology department, the department of biology should be written on the approval page. Exceptionally, for the interdisciplinary program chair and your thesis supervisor, the interdisciplinary program name should be written.
5. Write **the page number of the last page** in the related places given on Abstract and Öz pages.
6. All chapters, references, appendices and CV must be started on the right page. **Section Breaks** were used for this. **Change in the placement** of section breaks can result in extra blank pages. In such cases, make the section breaks visible by clicking paragraph (¶) mark and **check their position.**
7. All figures and tables must be given inside the page. Nothing must appear in the margins.
8. All the warnings given on the comments section through the thesis template must be read and applied.
9. Save your thesis as pdf and Disable all the comments before taking the printout.
10. **Print two-sided the PDF file that you have created through this form and make a single spiral bound.**
11. Once you have signed the relevant fields in your thesis draft that you spiraled, submit it to the department secretary together with your Thesis Jury Assignment Form.
12. This will be announced to the students via their METU students e-mail addresses when the control of the thesis drafts has been completed.
13. If you have any problems with the thesis writing process, you may visit our **Frequently Asked Questions (FAQ)** page and find a solution to your problem.

☒ **Yukarıda bulunan tüm maddeleri okudum, anladım ve kabul ediyorum. / I have read, understand and accept all of the items above.**

```
Name      : Lütfi Koray
Surname   : İroç
E-Mail    : korayiroc@gmail.com
Date      :
Signature : _____
```

DEVELOPMENT AND PRODUCTION OF DUCTILE TIZRNBHFTA
REFRACTORY HIGH ENTROPY ALLOY SYSTEM FOR EXTREME
ENVIRONMENTS

A THESIS SUBMITTED TO
THE GRADUATE SCHOOL OF NATURAL AND APPLIED SCIENCES
OF
MIDDLE EAST TECHNICAL UNIVERSITY

BY

LÜTFİ KORAY İROÇ

IN PARTIAL FULFILLMENT OF THE REQUIREMENTS
FOR
THE DEGREE OF MASTER OF SCIENCE
IN
METALLURGICAL AND MATERIALS ENGINEERING

January 2022

Approval of the thesis:

DEVELOPMENT AND PRODUCTION OF DUCTILE TIZRNBHFTA REFRACTORY HIGH ENTROPY ALLOY SYSTEM FOR EXTREME ENVIRONMENTS

submitted by **LÜTFİ KORAY İROÇ** in partial fulfillment of the requirements for the degree of **Master of Science** in **Metallurgical and Materials Engineering, Middle East Technical University** by,

Prof. Dr. Halil Kalıpçılar
Dean, Graduate School of **Natural and Applied Sciences**   _____

Prof. Dr. Cemil Hakan Gür
Head of the Department, **Metallurgical and Materials Eng.**   _____

Assist. Prof. Dr. Eda Aydoğan Güngör
Supervisor, **Metallurgical and Materials Eng., METU**   _____

Prof. Dr. Yunus Eren Kalay
Co-Supervisor, **Metallurgical and Materials Eng., METU**   _____

Examining Committee Members:

Prof. Dr. Arcan Dericioğlu
Metallurgical and Materials Engineering, METU   _____

Assist. Prof. Eda Aydoğan Güngör
Metallurgical and Materials Engineering, METU   _____

Prof. Dr. Yunus Eren Kalay
Metallurgical and Materials Engineering, METU   _____

Assoc. Prof. Caner Şimşir
Metallurgical and Materials Engineering, METU   _____

Prof. Dr. Ziya Esen
Department of Inter-Curricular Courses, Cankaya University   _____

Date: 13.01.2022

I hereby declare that all information in this document has been obtained and presented in accordance with academic rules and ethical conduct. I also declare that, as required by these rules and conduct, I have fully cited and referenced all material and results that are not original to this work.

Name Last name : Lütfi Koray İroç

Signature :

ABSTRACT

DEVELOPMENT AND PRODUCTION OF DUCTILE TIZRNBHFTA REFRACTORY HIGH ENTROPY ALLOY SYSTEM FOR EXTREME ENVIRONMENTS

İroç, Lütfi Koray
Master of Science, Metallurgical and Materials Engineering
Supervisor: Assist. Prof. Eda Aydoğan Güngör
Co-Supervisor: Prof. Dr. Yunus Eren Kalay

January 2022, 117 pages

High entropy alloy (HEA) is a trending material class that was discovered in the early 2000s. By definition, it consists of a single or dual phase by combining 5-13 elements with a 5-35% atomic ratio. They exhibit extraordinary properties, such as structural, mechanical, corrosive and thermal. Moreover, this field gives an opportunity to combine infinite number of elements with infinite compositions. These properties and opportunities make them candidates for various extreme application areas, which will grow further in the future. Among the HEAs, Refractory High Entropy Alloys (RHEAs) are considered as future materials for high-temperature and nuclear applications due to their thermal stability and high-temperature mechanical properties. This study focuses on improving structural and mechanical properties and understanding the high-temperature and irradiated characteristics of RHEAs. By using CALPHAD modeling and thermophysical

parameter optimization, two alloys were designed as oxygen-doped and undoped compositions. These alloys were produced by vacuum arc melting (VAM), and the structural characterization was performed using X-ray diffraction (XRD), scanning electron microscopy (SEM), and transmission electron microscopy (TEM). It has been found that both alloys consist of a single solid solution with BCC structure without any ordered phase, as designed. Besides, micro-indentation was performed to understand their hardness. It has been observed that oxygen-doped and undoped alloys exhibit hardness values of 440HV and 321HV, respectively and oxygen-doped alloy exhibited 1240 MPa compressive yield strength with a ductile behavior. The high-temperature behavior of promising oxygen-doped alloy is investigated by differential scanning calorimetry (DSC), in-situ XRD and TEM analyses. The results revealed that oxygen-doped RHEA contains a single BCC structure above 1000 °C without any metallic oxide. Also, oxygen doping does not make any significant structural or morphological difference compared to undoped alloy, similar to the simulation results. Eventually, considering the room temperature structure and mechanical improvements of oxygen-doping, the results are encouraging for the high-temperature applications of oxygen-doped RHEAs. Finally, to understand the radiation resistance, the oxygen-doped alloy is irradiated at three dosages (3, 10 and 30 dpa) and two temperatures (room temperature and 450 °C). Radiation effects are investigated using transmission electron microscopy (TEM) and nanoindentation. Mechanical and dislocation loops analyses revealed that there is no phase transformation, structural change, void formation as well as low hardening for all conditions. The observed high resistance under radiation makes oxygen-doped RHEA a good candidate for nuclear applications.

Keywords: Refractory High Entropy Alloys (RHEA), Oxygen-doping, Alloy Design, Thermal Stability, Radiation Resistance.

ÖZ

EKSTREM KOŞULLARA DAYANIKLI VE SÜNEK TİZRNBHFTA REFRAKTER YÜKSEK ENTROPİ ALAŞIMI SİSTEMİNİN GELİŞTİRİLMESİ VE ÜRETİLMESİ

İroç, Lütfi Koray
Yüksek Lisans, Metalurji ve Malzeme Mühendisliği
Tez Yöneticisi: Yrd. Doç. Eda Aydoğan Güngör
Ortak Tez Yöneticisi: Prof. Dr. Yunus Eren Kalay

Ocak 2022, 117 sayfa

Yüksek entropi alaşımları (YEA), 2000'li yılların başında keşfedilmiş, popüler bir konu ve malzeme sınıfıdır. Tanım olarak, 5-13 elementin %5-35 atomik oranlı kombinasyonu ile meydana gelir ve tek veya çift fazdan oluşur. Bu alaşımları farklı kılan yapısal, mekanik, aşındırıcı ve termal anlamda alışılagelmişin dışında özellikler sergilemesidir. Ayrıca bu alan, sonsuz kompozisyon oluşturma fırsatı verir. Bu özellikler ve avantajlar çeşitli uygulama alanlarında kullanımına olanak sağlar. YEA'ların popüler olan alt gruplarından biri, Refrakter yüksek entropi alaşımlarıdır (RYEA). Yüksek termal kararlılıkları ve yüksek sıcaklıktaki mekanik özellikleri nedeniyle yüksek sıcaklık uygulamaları için geleceğin malzemeleri olarak kabul edilirler. Bu çalışma, yapısal ve mekanik özelliklerin geliştirilmesine ve RYEA'ların yüksek sıcaklık ve radyasyon altındaki özelliklerinin anlaşılmasına odaklanmıştır. CALPHAD modellemesi ve termofiziksel parametre optimizasyonu

kullanılarak oksijen katkılı ve katkısız olmak üzere iki alaşım tasarlanmıştır. Bu alaşımlar, vakumlu ark eritme ile üretilip X-ışını kırınımı (XRD), taramalı elektron mikroskobu (SEM) ve geçirimli elektron mikroskobu (TEM) ile yapısal karakterizasyonu yapılmıştır. Alaşım tasarımında amaçlandığı gibi her iki alaşımın da herhangi bir düzenli faz olmaksızın BCC yapılı tek bir katı çözeltiden oluştuğu görülmüştür. Ayrıca mikro sertlik testleri sonucu oksijen katkılı ve katkısız alaşımların sırasıyla 440HV ve 321HV sertlik değerleri sergiledikleri ve sünek bir davranış gösterdikleri gözlemlenmiştir. Oksijen katkılı alaşımın yüksek sıcaklık davranışı, diferansiyel taramalı kalorimetri (DSC) ve yüksek sıcaklık XRD analizleri ile araştırılmıştır. Sonuçlar, oksijen katkılı RYEA'nın 1000 °C'nin üzerinde herhangi bir metalik oksit içermeyen tek bir BCC yapısı içerdiğini ortaya koymuştur. Ayrıca oksijen katkısı, simülasyonlarla ilişkilendirilirken katkısız alaşıma kıyasla yapısal veya morfolojik farklılık yaratmamaktadır. Sonuç olarak, oda sıcaklığı yapısı ve oksijen katkılı mekanik iyileştirmeler göz önüne alındığında, yüksek sıcaklık analizlerinin sonuçları, oksijen katkılı RYEA'ların yüksek sıcaklık uygulamalarını teşvik etmektedir. Son olarak, oksijen katkılı RYEA'nn radyasyona karşı direncini araştırmak amacıyla 3 doz (3, 10 ve 30 dpa) ve 2 sıcaklıkta (oda sıcaklığı ve 450 °C) alaşıma radyasyon uygulanmış ve sonuçlar geçirimli elektron mikroskobu (TEM) ve nano sertlik ölçümleriyle incelenmiştir. Yapısal, mekanik ve dislokasyon analizleri sonucu 6 durumda faz değişimi, yapısal değişim, boşluk oluşumu görülmemiş ve düşük sertlik artışı eğilimi görülmüştür. Bu sonuçlar doğrultusunda oksijen katkılı RYEA'ların yüksek radyasyon dayancı onu gelecekteki nükleer uygulamalarda kullanılması için iyi bir aday haline getirmiştir.

Anahtar Kelimeler: Refrakter Yüksek Entropi Alaşımları, Oksijen-doplama, Alaşım Dizaynı, Termal Kararlılık, Radyasyon Direnci

To every graduate student who dreads writing their thesis

ACKNOWLEDGMENTS

TABLE OF CONTENTS

LIST OF TABLES

TABLES

LIST OF FIGURES

FIGURES

xvi

xviii

LIST OF ABBREVIATIONS

HEA	High Entropy Alloy
THEA	Transition High Entropy Alloy
RHEA	Refractory High Entropy Alloy
MEA	Medium Entropy Alloy
CCA	Complex Concentrated Alloy
FCC	Face Centered Cubic
BCC	Body Centered Cubic
HCP	Hexagonal Close Packed
VEC	Valence Electron Concentration
SS	Solid Solution
IC	Intermetallic Compound
ODS	Oxide Dispersion Strengthened
HIP	Hot Isostatic Pressing
VAM	Vacuum Arc Melting
DBTT	Ductile to Brittle Transition Temperature
RT	Room Temperature
SEM	Scanning Electron Microscopy
EDS	Energy Dispersive Spectroscopy
FIB	Focused Ion Beam
TEM	Transition Electron Microscopy
SAED	Selected Area Electron Diffraction
HT-XRD	High-Temperature X-ray Diffraction
DSC	Differential Scanning Calorimetry
CALPHAD	Calculation of Phase Diagram
SRIM	Spotting and Range of Ions in Matter
PKA	Primary Knock-on Atom
dpa	Displacement per atom
ROM	Rule of Mixture
OOC	Oxygen Ordered Complex

LIST OF SYMBOLS

Å	Angstrom
°C	Degree Celsius
K	Kelvin
δ	Atomic Size Difference
Ω	Omega Parameter
T_m	Melting Temperature
ΔS_{mix}	Entropy of Mixing
ΔH_{mix}	Enthalpy of Mixing
ΔG_{mix}	Gibbs Free Energy of Mixing

CHAPTER 1

INTRODUCTION

Alloy design has always been a challenging subject for humankind. Today, conventional strategy on alloy design is based on the selection of one or two principal elements and the addition of alloying elements in small amounts. Even though they are defined as multicomponent alloys, they are still based on one or two main elements. This strategy has a limitation of improving the final properties since the principal alloy(s) is compositionally dominant, and the effects of alloying elements are obligated. The recent advent of high entropy alloys (HEAs) removes this limitation and brings excessive combinations to the alloy design concept.

Historically, the idea of multi-principal element alloys is not ancient at all. The first idea of multicomponent metallic alloy is proposed with FeCrMnNiCo alloy by Cantor in the 1970s and developed through the years[1]. However, the HEA concept is extended in the studies in the early 2000s and publications of these studies in 2004[2]–[4]. According to the definition of Yeh in one of these works, HEAs consist of 5-13 principal elements within the amounts of 5-35%[2]. Also, it might contain minor elements to improve the properties of the base HEA. What makes them interesting is that the number of possible binary or ternary phases increases with the increasing number of principal elements, but HEAs consist of simple solid solutions like FCC or BCC. It is also stated that all atoms are randomly distributed through the lattice without defining any "matrix element". Besides this compositional definition, another one is entropy-based, which classifies alloys according to their total configurational entropy as high ($\Delta S_{conf} > 1.61R$), medium ($1.61R > \Delta S_{conf} > 0.69R$), and low ($\Delta S_{conf} > 0.69R$) entropy

1

alloys[5]. For comparison, this value is 0.22R for 4340 steel and 0.43R for 7075 aluminum alloy, while it is 1.61R for a 5-component equimolar HEA. This value increases for HEA with the addition of more components but decreases when equimolarity is disturbed by varying compositions. In addition to these definitions, a microstructural definition states that at least 5 elements must form a single solid solution[6]. The formation of any intermetallic compound (IC) would violate this definition of HEA. In addition to these HEA definitions, there are also similar systems that dissociate from HEA through structure or composition. For example, the terms for concentrated ternary and quaternary alloys are Multi Principal Element Alloys (MPEA) and Medium Entropy Alloys (MEA). Also, another material group called Complex Concentrated Alloy (CCA) has 3 or more principal elements and the amounts can be higher than 35 at%. CCAs differ from HEAs by containing intentionally formed multiphases instead of a single solid solution.

As defined in Yeh's entropy-based definition, one of the most significant differences between conventional alloys and HEAs is the very high configurational entropy value of HEAs. The motivation of increasing the constitute number is maximizing the configurational entropy of mixing. Therefore, the solid solution phase will be stabilized instead of binary or ternary intermetallic compounds. These compounds are undesirable due to their brittleness accompanied by nearly zero ductility. On the contrary, the simplicity of a single solid solution provides a wide range of mechanical properties. Including this structural behavior, HEAs show unusual thermodynamic and kinetic properties, which separate them from conventional alloys. These properties are explained as "4 Core Effects of HEA".

Since the discovery of HEAs in 2004, various compositions have been proposed. The reason behind the acceleration in HEA studies is their unexpectedly promising properties. Depending on composition, these properties include high strength and hardness[7], biocompatibility [8], high corrosive[9], thermal[10], irradiation[11],

fatigue[12] and wear[13] resistance. Refractory High Entropy Alloys (RHEAs) are projected as promising candidates for refractory applications due to their heavily distorted lattice and sluggish diffusion[4][14]. Also, the effect of configurational entropy is expected to increase at higher temperatures, resulting in high phase stability[15]. The first studies on RHEAs were reported on NbMoTaW and VNbMoTaW compositions in 2010 and they exhibited promising properties, such as extreme hardness values at room temperature and high strength up to 1600 °C without any sudden drop[16], [17]. After the first proposal of HEAs in refractory applications, several compositions are designed with the combinations of 9 elements from group IV, V and VI (Ti, V, Cr, Zr, Nb, Mo, Hf, Ta and W). However, their lack of ductility (below 5% elongation) restricts their usage for structural applications. There are several studies focused on improving the ductility of RHEAs intrinsically[18], [19] and extrinsically[2], [20]. In 2016, it was shown that the ductility of the BCC RHEAs is closely related to their valence electron concentration (VEC)[19]. In other words, there is an instinct ductility for a few RHEAs with VEC values lower than 4.4, showing elongation between 6-18.8%[19], [21], [22]. Recently, the ductility of the low VEC system has been reported to be improved by oxygen doping while enhancing the strength simultaneously[20]. Lei et al.[20] has reported that the introduction of a small amount of oxygen (2 at%) into TiZrNbHf medium entropy alloy (MEA) increased the strength by ~50% (from 750 MPa to 1110 MPa) and ductility ~95% (from 14.2% elongation to 27.7%) simultaneously. However, there is no thermal study on this promising material system, whether it is suitable for refractory applications or not, which is one of the research questions of this study.

Another research question of this study will be the characteristics of oxygen-doped RHEAs under irradiation. For nuclear applications, structural stability and low hardening behavior are desired for a sufficient lifetime. RHEAs are considered as promising radiation-resistant materials due to their core effects; sluggish kinetics

and distorted lattices[23]–[27], with addition to their significant self-healing feature[27]–[30]. Radiation-induced damage can be characterized by using TEM and nanoindentation. Oxygen-doping into RHEAs is a new concept that improves mechanical properties without any structural drawback[20][31]. Besides their high-temperature behavior, their irradiation characteristics are also never studied.

The motivation of this study is understanding the structure-property-production triangle of oxygen-doped RHEAs with various characterization tools. Oxygen-doped RHEAs are promising in structural and mechanical manner, however, there is no study for high-temperature and radiation resistance for this material group. This study aims to design an oxygen-doped RHEA to be used in high-temperature and nuclear applications. For that purpose, the steps of this study are shown in Figure 1.1 as a storyboard.
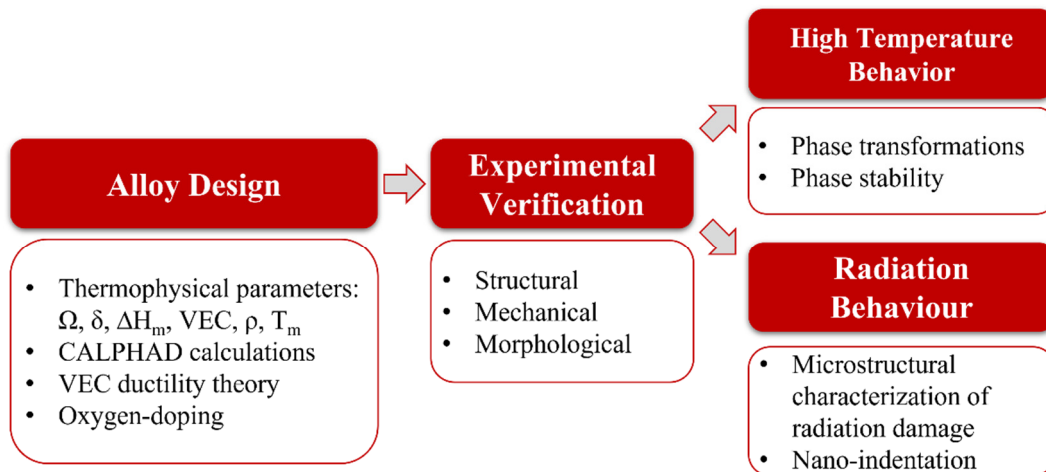
Figure 1.1. Storyboard of this study

CHAPTER 2

LITERATURE REVIEW

2.1   Formation of HEAs

2.1.1   Thermodynamics

Classical thermodynamic theories for conventional alloys, are not valid for HEAs, since they accept equal-sized atoms in the mixture. Moreover, the configurational entropy term is more effective for HEAs than the alloys with one dominating element, so that this term cause the thermodynamical differences for HEAs. Therefore, the prediction of the phases and crystal structure becomes important for HEAs. Several models and parameters are proposed for the estimation of solid solution phase (SS) and intermetallic compounds (IC) [32]–[38]. These models are based on Hume-Rotary rules; they include geometrical and thermodynamical relations of the constituent elements. For these models, the higher coherency of the constituent elements (small atomic size difference and low enthalpy of mixing) leads to tendency to form a random SS.

Atomic size difference (δ) is a geometric factor. It indicates the dimensional variations on lattice sites. Therefore, a small atomic size difference means less lattice distortion related to the dimensional fluctuations; leading to a regularly distributed, random, disordered solution. It is expressed in Eq.2.1, where c_i is the amount of element "i" in at%, r_i is the atomic radius of element "i" and $\bar{r}$ is the average radius.

$$\delta = 100 \, x \sqrt{\sum_{i=1}^{N} c_i \, (1 - \frac{r_i}{\bar{r}})^2} \qquad \text{Eq.2.1}$$

For the thermodynamical relations, the most accepted parameter is the enthalpy of mixing (ΔH_{mix}) in Eq.2.2. Various ranges are proposed for the formation of SS and these ranges evolved through the time [32][33][34]. The larger negative value of ΔH_{mix} means attraction, so it leads to short-range ordering (like IC) due to stronger bonds, while the larger positive value means repulsion, so it leads to phase segregation due to less miscibility. In the case of zero enthalpy of mixing (like in an ideal solution), the distribution of atoms is in complete randomness. However, it is not common for HEAs since ΔH_{mix} is not zero most of the time and atomic distribution is nearly in complete randomness like it is in the regular solutions. Therefore, HEAs are considered as regular solutions while defining mixing entropy (ΔS_{mix}) parameter in the Eq.2.5.

In 2008, Zhang proposed that ΔH_{mix} must be between -15 kJ/mol and 5 kJ/mol and $\delta<6.2\%$ to form a disordered single solid solution[33]. Also, in the same study, it is stated that ordered solid solution may form when $\delta>4.3\%$, which creates an intersection area between SS and IC limits at the range of 4.3%-6.2% (Figure 2.1). This model focuses on the enthalpy and not include the entropic effect.

$$\Delta H_{mix} = \sum_{i<j} 4H_{ij}c_i c_j \qquad \text{Eq.2.2}$$

6
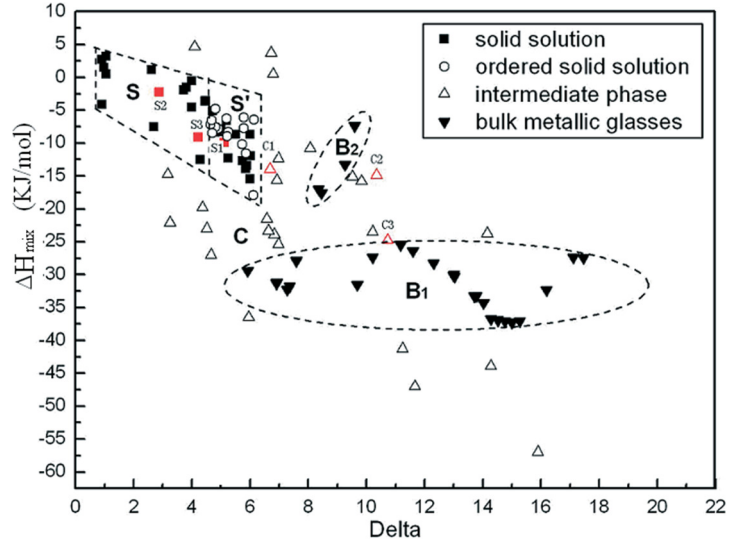
Figure 2.1. ΔH_{mix} and Delta parameters for HEAs, MPEAs and bulk metallic glasses [33]

Later on, a more comprehensive approach; Ω parameter (Eq.2.3) is proposed by Yang[35], which is formed by converting the parameters of Gibbs free energy (Eq.2.4); ΔH_{mix} (Eq.2.2), ΔS_{mix} (Eq.2.5) and T_m. The principle is the same for both formulations; minimization of entropic term and maximization of enthalpic term induce the stabilization of the disordered phase. In other words, lower free energy and higher Ω parameter increase the tendency for the HEA formation. To minimize entropic term, temperature and/or number of the components must be maximized, which is the motivation behind the HEA concept. Several studies were plotted on Figure 2.2, determining the solid solution formation parameters as $\Omega > 1.1$ and $\delta < 6.6\%$ and IC range as ($\Omega < 10$ or $\delta > 4\%$), which, again intersects with SS region.

$$\Omega = \frac{T_m \, \Delta S_{mix}}{|\Delta H_{mix}|} \qquad \text{Eq.2.3}$$

$$\Delta G_{mix} = \Delta H_{mix} - T\Delta S_{mix} \qquad \text{Eq.2.4}$$

$$\Delta S_{mix} = -R \sum_{i=1}^{N} x_i \, lnx_i \qquad \text{Eq.2.5}$$
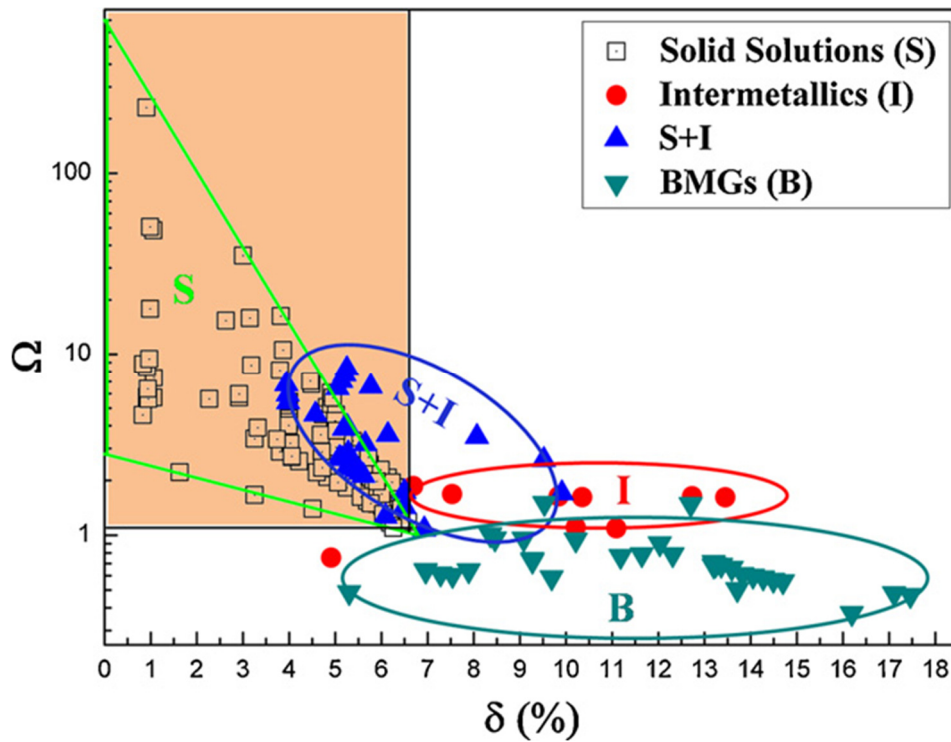
Figure 2.2. δ and Ω parameters of multicomponent alloys and resulting phases[35]

According to a study[39], these two models, which are proposed by Zhang and Yang, have the highest accuracies of predicting SS formation among 5 models; 93% for ΔH_{mix} model and 98% for Ω model. However, accuracies for IC formation of these models are not high enough. Because their limits are set for SS region and there is an intersection range of SS and IC formation regions at all proposed models [32]–[35]. This situation creates a critical uncertainty of structure, which directly affects the properties and performance of the HEA.

2.1.2 Four Core Effects

By compositional definition, HEAs consist of at least 5 principal elements and form a single solid solution. Compared to conventional alloys, it generally does not obey the thermodynamic rules. For example, the Gibbs phase rule expresses the maximum number of possible phases (P) for an equilibrium system, depending on its degree of freedom (F) and the number of components (C) (Eq.2.6). This rule indicates that, for example, a ternary phase cannot have more than 4 phases in equilibrium. On the other hand, HEAs can consist of single FCC or BCC structures, which is less than the maximum number of phases indicated by Gibbs Phase Rule. This is attributed to the large configurational entropy resulting in mutual solubility of constituent atoms on each other and limiting the various phase formation, while supported by sluggish kinetics.

$$P + F = C + 1 \qquad\qquad Eq.2.6$$

"4 Core Effects" explain the uncommon structural and mechanical behaviors of high entropy alloys, such as disobeying Gibbs phase rule. These distinct effects separate HEAs from conventional alloys. For thermodynamics, 'High Entropy Effect' explains the disagreement with Gibbs phase rule and the formation of random solid solution. For kinetics, 'Sluggish Diffusion' explains the effect of slow atomic motion on phase formation. For structural effects, 'Severe Lattice Distortion' is the reason for strengthened mechanical behavior. For properties, 'Cocktail Effect' explains why properties of HEAs are much different than the constituent elements.

2.1.2.1   High Entropy Effect

Mixing entropy has four components as configurational, vibrational, magnetic, and electronic entropy terms. Especially for HEA studies, configurational entropy is very dominant and it is considered as equal to total mixing entropy[40], [41]. Configurational entropy (ΔS_{conf}) is the formulation of positional elemental disorder in a mixture and it is independent of material properties (Eq.2.5). When the constituent elements have an equal atomic percentage (also called equiatomic), this formula is simplified and turns into; $\Delta S_{mix} = RlnN$, where N is the number of elements present in alloy and R is the gas constant.

HEAs can be distinguished from conventional alloys by their ΔS_{mix} values. According to relation in Eq.2.4, the phases with higher mixing or configurational entropy (ΔS_{mix}) have lower Gibbs free energy (ΔG_{mix}), and they are stabilized, which is the fundamental of HEAs. For the entropy concept, while defining ΔS_{mix}, electronic, magnetic and vibrational components are neglected because the configurational term is more dominant for thermodynamical approach. This value is 0.22R, 0.43R and 1.61R for 4340 low-alloy steel, 7075 series aluminum and equiatomic 5-element HEA, respectively[41]. Also, atoms are displaced from their lattice sites due to severe lattice distortion, which gives an additional configurational entropy. Table 2.1 gives the comparison for thermodynamic states of different possibilities; elements keep their elemental phase, they form compounds and they dissolve into a random solid solution (HEA case). It can be seen that the difference in ΔS_{mix} leads to a larger negative value for ΔG_{mix} of solid solution, therefore random solid solution phase forms by suppressing other possibilities.

Table 2.1 Comparison of thermodynamic data for multicomponent possibilities[41]

	Elemental Phases	Compound	Solid Solution
ΔH_{mix}	~0	Large negative	Medium negative
ΔS_{mix}	~0	~0	Eq.2.5
ΔG_{mix}	~0	Large negative	**Larger negative**

To form intermetallic compounds, the formation enthalpy of the IC must overcome the entropic effect. When an element has a high ΔH_{mix} with other elements, the high entropy effect cannot be dominant. Therefore, the element applies a repulsion force and causes segregation, which disturbs single phase formation. As an example, Weh et al. have reported the formation of the Cu-rich phase at interdendrites by segregation of Cu from AlCoCrCuFeNi alloy. This phenomenon is explained by binary ΔH_{mix} values. Cu has high mixing enthalpy with all elements, resulting in an alternative phase[42]. High Entropy Effect cannot guarantee the formation of a single solid solution by itself. Previously mentioned thermophysical parameters, like ΔH_{mix}, Ω and δ should also be taken into consideration.

2.1.2.2 Sluggish Diffusion Effect

Diffusion and phase transformation kinetics of HEAs are slower than conventional alloys. Thermal diffusivities (T_D) of 4 AlCrFeMnNiMo family HEAs and aluminum are plotted in Figure 2.3. It clearly indicates that HEAs show slow (sluggish) kinetics [43]. This effect can be investigated under two aspects: path of the motion and properties of travelling atom.
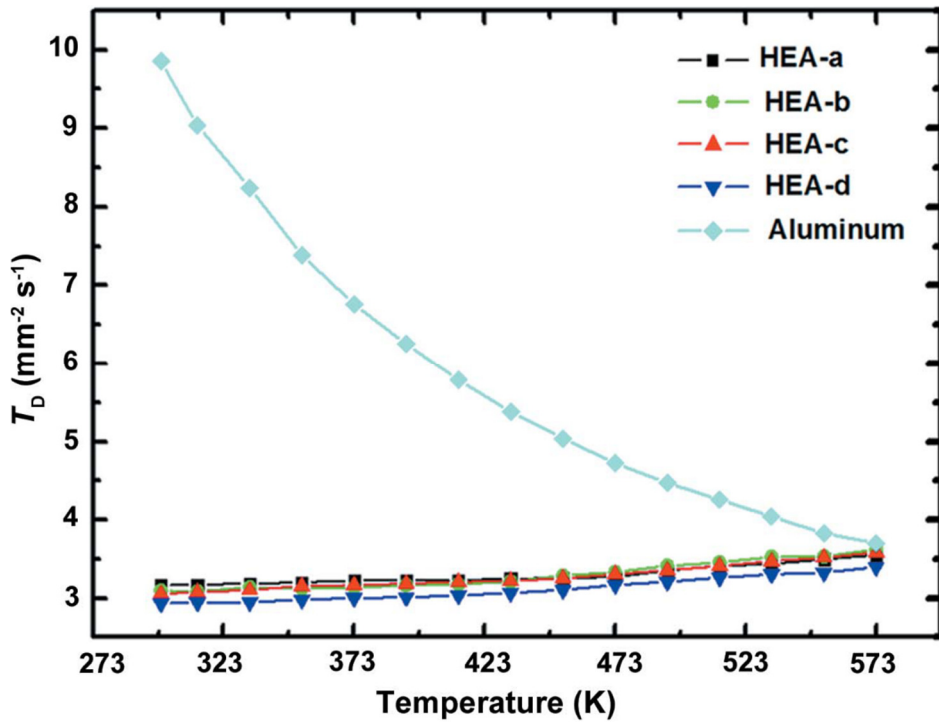
Figure 2.3. Thermal diffusivities (T_D) of Al and 4 AlCrFeMnNiMo group HEAs [43]

First, different kinds of atoms are distributed randomly on lattice sites. They create a variation of atomic potential energy through the diffusion path. It is proven that these variations create traps for mobile atoms, which restrain atomic motion[44]. Figure 2.4 shows the variation of site energy through the path of diffusion and deep traps occurring due to this variation on HEAs. For a pure element, each lattice site must have equal potential energy.

Secondly, mobile atoms show different diffusion rates due to their different atomic radii and mobility. The activation energy of the motion varies depending on the type of the atom. A detailed work on sluggish diffusion compares the CoCrFeMnNi HEA with conventional FCC alloys. This work proves that; diffusion coefficient is lower, while activation energy is higher in HEAs[45].
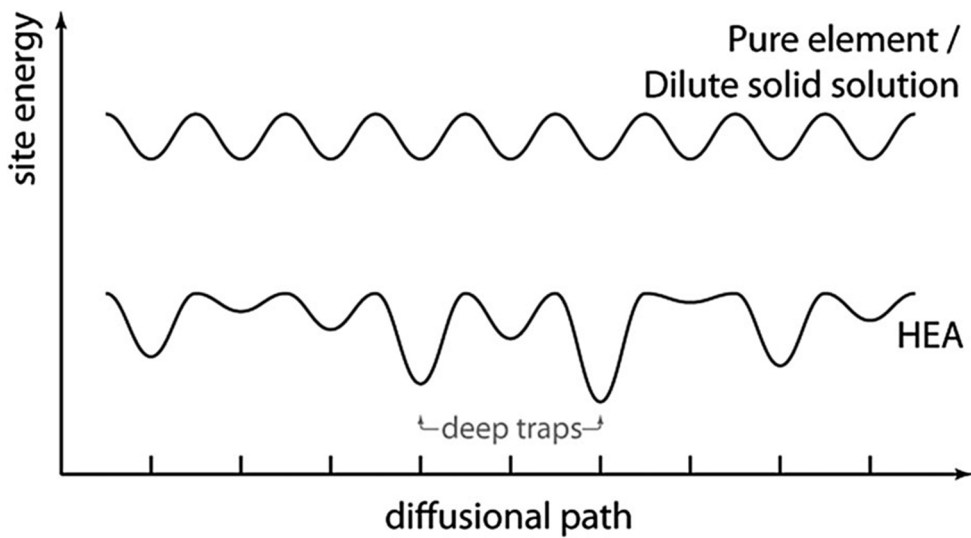
Figure 2.4. Diffusion profiles of pure element (top) and HEA matrix (bottom)[44]

The most distinctive effect of sluggish diffusion is helping the "high entropy effect" on restraining the formation of alternative phases. In addition to that, slow kinetics promotes structural stability at elevated temperatures.

2.1.2.3 Severe Lattice Distortion Effect

A substitutional solute atom generates a tensional or compressive strain field due to its atomic size difference with neighbor matrix atoms. These stresses create solid solution strengthening to the alloy. For the HEA case, at least 5 different kinds of atoms are distributed randomly through the matrix. None of the atoms fit perfectly on the lattice site without creating tension or compression, which is illustrated in Figure 2.5. This distortion is more severe than conventional alloys since every atom act like a substitutional impurity to each other and create stress that distorts the lattice. The presence of distorted lattice can be proved by low peak intensity in XRD data since the strain field creates more scattering in diffracted X-Rays[2].

13
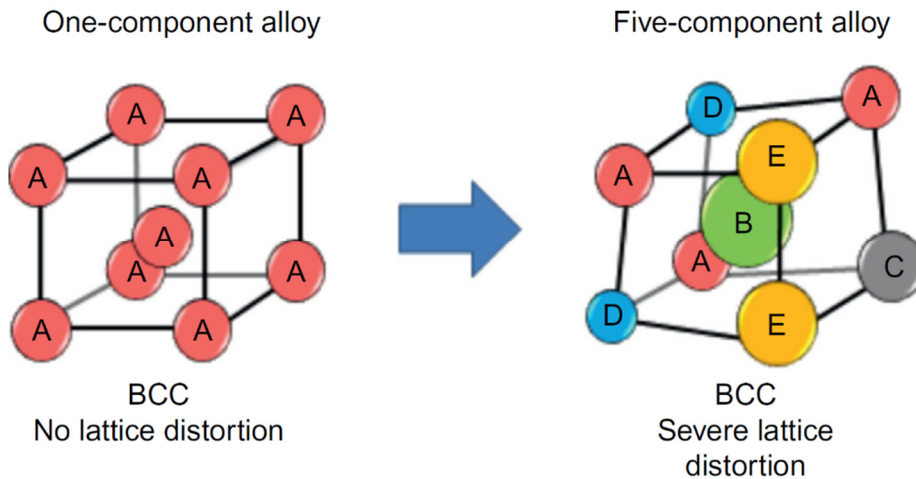
Figure 2.5. Distortion of the unit cells, pure element (left), HEA (right) [41]

Lattice distortion affects both mechanical and thermal properties. Hardness and strength considerably increase due to distorted lattice. Zhang et al. produced single BCC phase AlCoCrFeNi HEA with yield strength around 1500 MPa and explained this high mechanical property as the blockage of dislocation motion by the distortion of crystal lattice due to local elastic stress fields[46]. Also, thermal and electrical resistivity is high for HEAs due to high scattering of distorted lattice.

2.1.2.4   Cocktail Effect

The cocktail effect is used for explaining the extraordinary properties of HEAs. The properties of any alloy are undoubtedly related to its constituent elements, but the cocktail effect also considers the effect of interactions among atoms. Since the atoms of any constituent element are distributed throughout the lattice randomly, instead of forming an elemental phase, they must be considered to act as individual atoms. Therefore, HEA shows different properties than its constituent elements' properties in their pure state. Also, the cocktail effect explains why the overall

14

effect of composing elements brings excess values for HEA, instead of average values that are calculated from mixture rule.

To demonstrate this effect, a study on gradually addition of aluminum into CoCrCuFeNi alloy and their hardness are shown in Figure 2.6. Aluminum is FCC and relatively soft metal in its pure state, so it is expected that the addition of aluminum makes HEA softer. However, the results show the opposite; the addition of aluminum increases hardness due to strong bond energy, larger atomic radius and lower valence electron value[7].
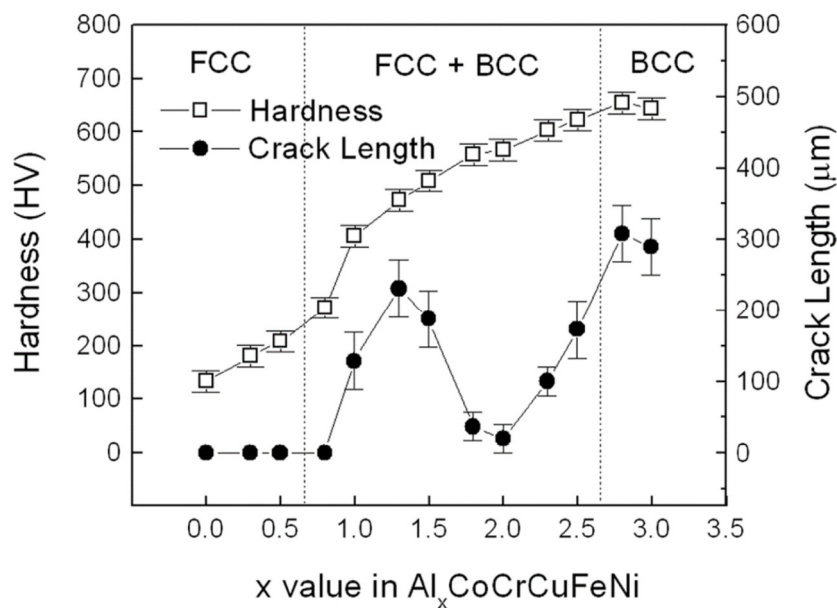
Figure 2.6. Hardness vs. Al% plot of AlxCoCrCuFeNi alloy[7]

This effect is clearly seen in hardness or wear resistance behavior, such as having hardness values 2-4 times higher than the average value. Nevertheless, for some properties where atomic interaction is not important, like density, the final value is simply the average depending on composition. It is hard to determine a scale for this effect, so it can be said that; it is the overall effect of structure, composition and microstructure. It can also be said that mutual atomic interactions are more important than atomic properties while determining the HEA properties.

2.2 Production of HEAs

To produce HEAs, classic metal production routes such as casting are not applicable. More controllable and small-scale methods are preferred for precision. Depending on the state of constituent materials during the production, these routes can be divided into 3; solid, liquid and gas state production techniques. Liquid state production is the most popular one among those. In addition to that, additive manufacturing techniques are successfully used to produce HEAs and gathers attention in recent years. During additive manufacturing, the powders are melted and solidified, but there will be an extra chapter due to its different method and kinetics.

2.2.1 Solid State Production

Solid-state production techniques can be defined as mechanical alloying (MA). It is a series of mechanical treatments to mix and blend the ingredients. Therefore, they form an alloy by diffusing into each other without changing their solid-state.

A standard mechanical alloying process can be seen in Figure 2.7. It starts with ball milling, which is a commonly used technique for powder metallurgy and production of the ODS alloys. Pure elements are charged into the mill with hard balls and rotated together. During rotation, particle size decreases, particle shape changes and constituents diffuse into each other. When the ball milling step is over, additional heat treatments are applied to improve final properties by consolidation. For instance, hot isostatic pressing (HIP) and spark plasma sintering (SPS) are thermomechanical post processes to create denser products by sintering. Finally, stress relief treatment can be applied to eliminate internal stress occurred during previous steps. One benefit of mechanical alloying is that structures with ultrafine grains can be achieved.
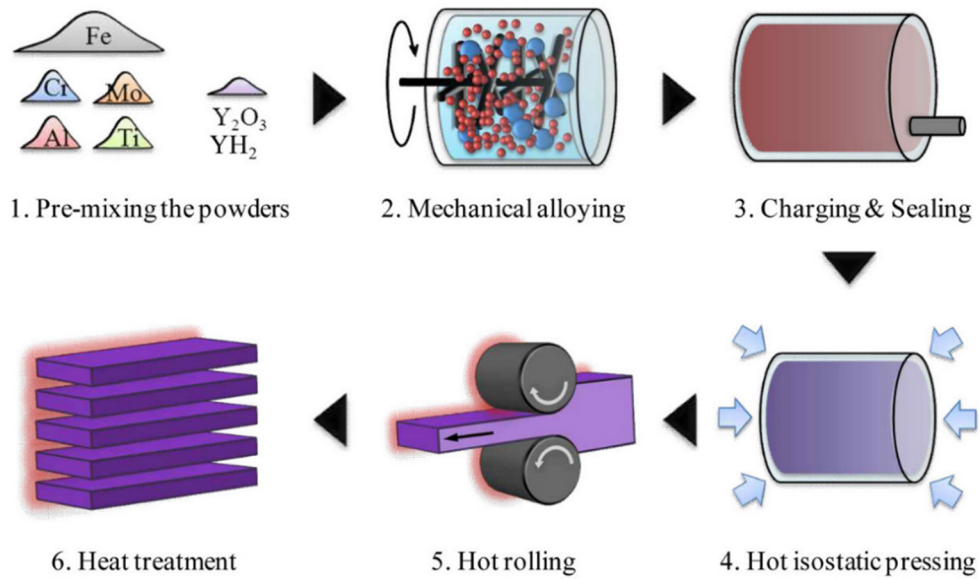
Figure 2.7. Mechanical alloying (MA) production steps for an ODS steel[47]

Wang et al. used mechanical alloying to produce single-phase CoCrFeNiMnAl HEA from powders smaller than 45 µm [48]. Figure 2.8 shows the transformation of elemental phases into a single solution phase from 6 to 60 hours. MA can achieve homogeneity, but it takes very long times, 30 hours in this study. However, due to ultra-fine grains (20 nm), high hardness value of 662 HV and compressive yield strength around 2100 MPa is achieved after the SPS post treatment.

The main problem with solid-state production is contamination due to the absorbent milling environment and active surfaces of the powders. For instance, a study on TiZrNbHfTa alloy discusses extending the production routes from liquid state to solid-state techniques[49]. It has revealed that, possible combinations of mechanical alloying techniques and post-processes could not eliminate the oxidation in the form of HCP precipitation or HfO_2 intermetallic compound, which is detrimental for the mechanical properties.
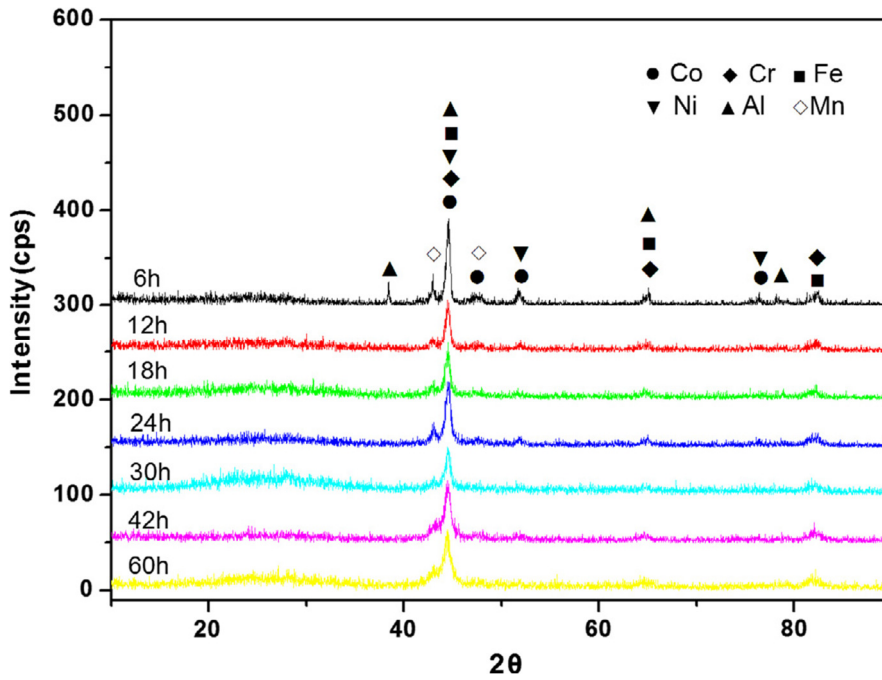
Figure 2.8. Effect of MA time on the structure of CoCrFeNiMnAl HEA[48]

In conclusion, considering the contamination, porosity and long times of milling and post treatment, solid-state production is more unprofitable with respect to liquid state production. However, it has the advantage of wider composition variety, which limits the liquid state production. Also, it can eliminate the dendritic structure, which is a very common result for liquid-state production techniques on HEAs. Therefore, it can be concluded that solid-state production techniques are problematic in many aspects and can be preferred only for specific compositions over liquid-state techniques.

2.2.2   Liquid State Production

Liquid state production is the most preferred method for the production of HEAs, almost 75% of the published papers are related to liquid state production techniques[41]. It consists of melting the solid constituents together, mixing in the

18

liquid state and finally solidification. Since the oxygen affinity of metals increases at elevated temperatures, these processes are applied under a protective atmosphere. Liquid production methods diversify by their energy source for melting, such as arc, induction, laser and electric resistance melting.
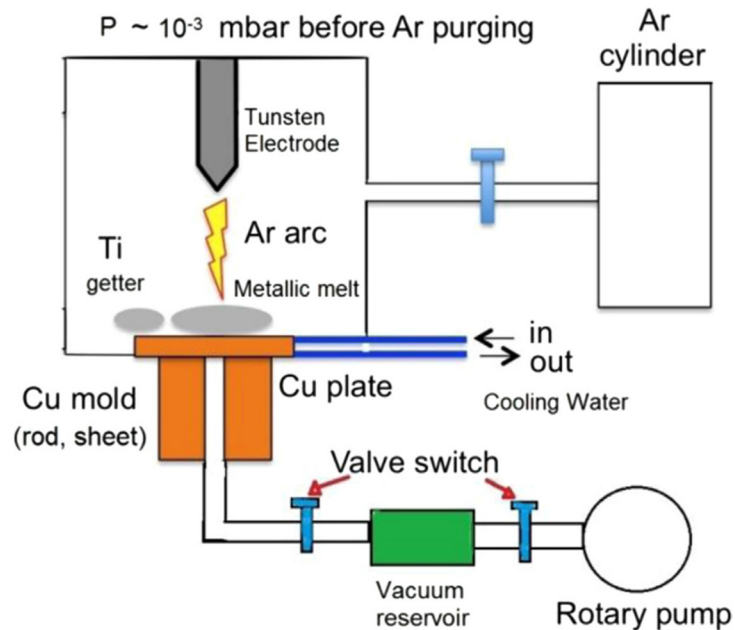
Figure 2.9. Schematic representation of VAM process and suction cast attached to it[50]

Vacuum arc melting (VAM) is the most common technique for producing HEAs, among other liquid state production techniques. In this technique, an arc is created between the electrode and the batch, placed in the copper crucible to melt it as shown in Figure 2.9. The alloys repetitively go under melting-solidification cycle to ensure the chemical homogeneity. The resulting microstructure is generally dendritic since the melting points of elements are different from each other, but it can be controlled by tailoring the composition. In 2019, a study by Yuan et al. was on the investigation of mechanical and biocompatible properties of the Ti-Zr-Nb-Ta alloy family with different compositions[8]. It has revealed that same constituents may show various morphologies depending on their stoichiometry as

shown in Figure 2.10. XRD results showed, each alloy has a single BCC structure, although their composition varies (Alloy 1: $Ti_{25}Zr_{25}Nb_{25}Ta_{25}$, Alloy 2: $Ti_{45}Zr_{45}Nb_5Ta_5$, Alloy 3 $Ti_{15}Zr_{15}Nb_{35}Ta_{35}$). Alloy 1 and alloy 3 showed dendrites enriched in Nb and Ta, while Ti and Zr go to interdendrites, which can be explained by prior solidification of elements with higher melting temperature. Also, increased amount of Nb and Ta creates nucleation of dendrites and leads to finer structure. Lower consumption of Nb and Ta in alloy 2 creates an equiaxed grain morphology.
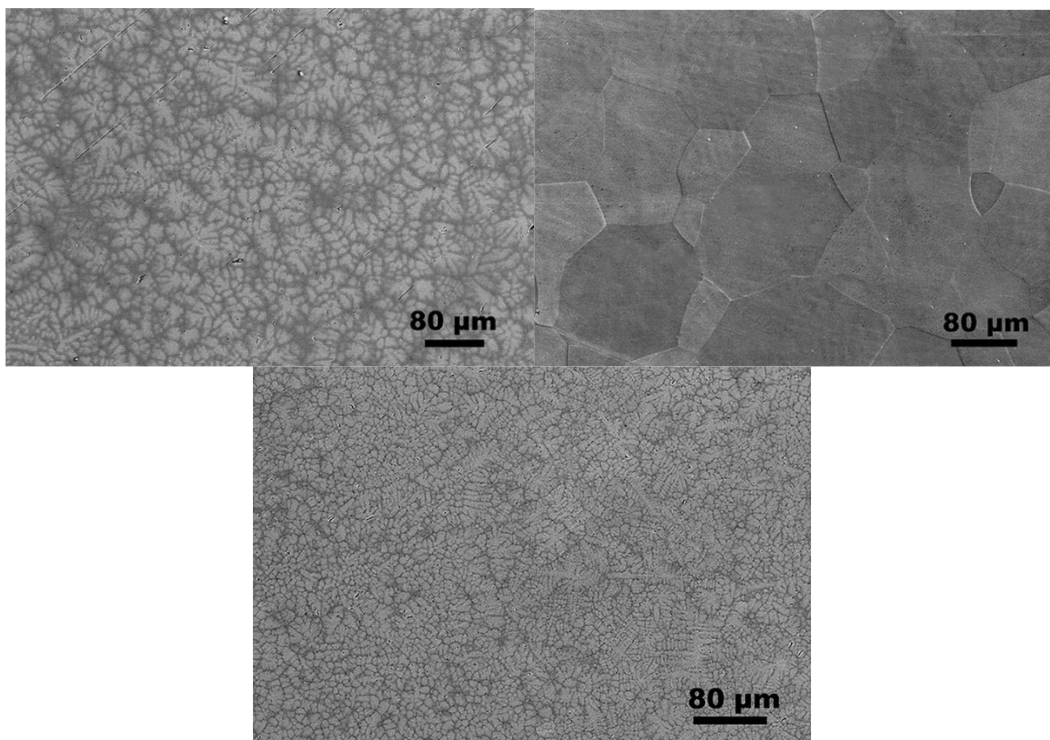
Figure 2.10. Optical images of a) $Ti_{25}Zr_{25}Nb_{25}Ta_{25}$, b) $Ti_{45}Zr_{45}Nb_5Ta_5$ and c) $Ti_{15}Zr_{15}Nb_{35}Ta_{35}$ HEAs[8]

The main disadvantage of arc melting is uncontrollable morphology. Small-scale production and slow cooling rate may create inhomogeneous and segregated microstructure from corner to center or casting defects like pores and cracks. Faster

cooling techniques such as suction-casting, splat quenching or melt spinning can suppress the formation of secondary phases. Singh et al. compared the microstructure of AlCoCrCuFeNi HEA in as-cast (slow cooling) and splat quenched (fast cooling) states[51]. In a splat-quenched state, high cooling rates $(10^6\text{-}10^7 \text{ K s}^{-1})$ leads to a simpler final structure; single BCC. In as-cast state, slower cooling (10-20 K s^{-1}) of the same alloy consists of B2 and L1$_2$ precipitates as shown in Figure 2.11.
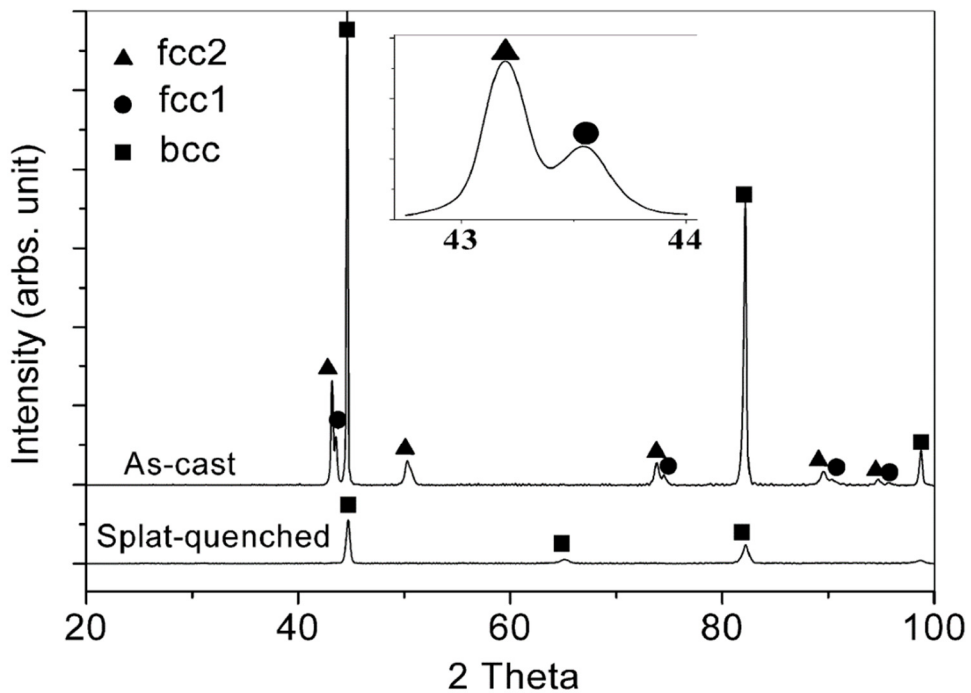
Figure 2.11. XRD of AlCoCrCuFeNi HEA for as-cast and splat-quenched productions[51]

2.2.3   Gas State Production

Gas state production techniques are used for the formation of HEA coatings and thin films on a substrate. The aim of these coatings is improvement of wear, corrosion or oxidation resistance. The major techniques are atomic layer deposition and vapor deposition techniques.
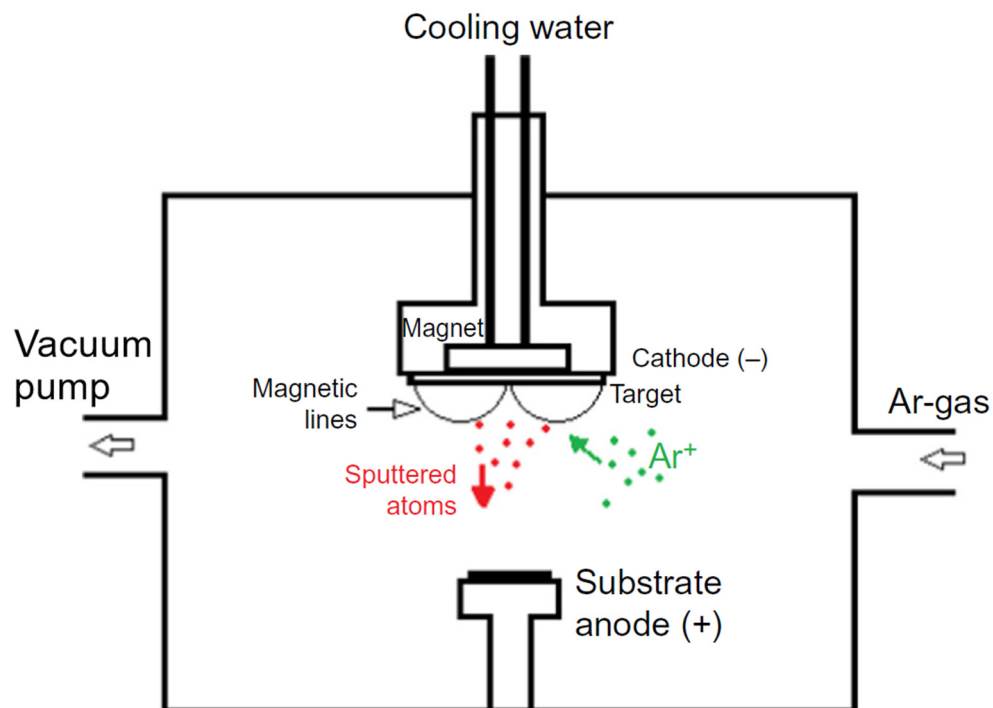
Figure 2.12. Schematic representation of the magnetron sputtering process[41]

The most common method is sputtering, which is a vapor deposition technique as represented in Figure 2.12. It is the deposition of target material atoms onto a substrate by the bombardment of charged particles. Sputtered atoms are randomly deposited on the substrate creating the entropy required for HEA. The deposition rate can be controlled by adjusting the power, voltage and argon pressure. Cheng et al. used magnetron sputtering to deposit $(AlCrMoTaTiZr)N_x$ films [52]. Results showed that these HEA films show thermal stability up to 1000 ºC, high hardness of 40.2 GPa and superior wear resistance, making it a candidate material for wear-resistant hard coating applications. In another work, $CoCrFeNiAl_{0.3}$ HEA thin film with a FCC structure is deposited by sputtering [9]. It showed ~200 GPa Young's modulus, 11.5 GPa hardness and better corrosion resistance than commercial 304 stainless steel, which can be commented as a good combination of strength and corrosion resistance.

2.2.4   Additive Manufacturing

Metal additive manufacturing techniques are based on the local melting and solidification of the metal powders with an energy source layer by layer. The advantage of these methods is having a local control on the microstructure for building or coating purposes with a net-shaped product. These techniques vary, depending on the type of energy source (heat, electron beam, arc or laser) and state of input materials (powder bed or feed). Depending on the state of input material, metal additive manufacturing methods are classified under two main categories: Powder Bed Fusion (PBF) and Directed Energy Deposition (DED), which are used to produce HEAs, successfully. The most common techniques of PBF are Selective Laser Melting (SLM) and Electron Beam Melting (EBM), while DED includes Laser Enhanced Net Shape (LENS), Laser Cladding and Direct or Laser Metal Deposition (DMD or LMD).

Production parameters, like input power and beam velocity are adjusted to control the microstructure of the alloy. Dobbelstein et al. studied production routes of TiZrNbTa alloys with Laser Metal Deposition (LMD) technique by various parameters and composition gradients[53]. EDS mapping of the cross-section on the product indicates that high feed speed results unmelted constituent elements like Ta and Nb (Figure 2.13a). Lower feed speed results a more homogeneous structure even though it is not fully homogenized (Figure 2.13b). Subsequently, the hatch distance is increased and a fully homogenized microstructure is achieved (Figure 2.13c), resulting in a new strategy for the modification of the conventional LMD process.
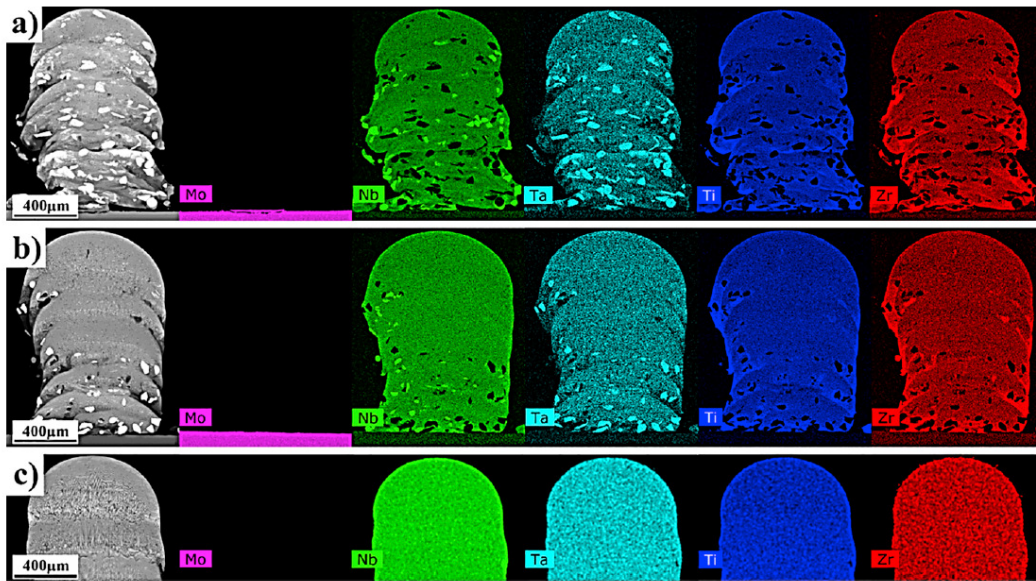
Figure 2.13. EDS mapping of the TiZrNbTa alloy produced with LMD a) High feed speed, b) Lower feed speed and c) Lower feed speed with higher hatch distance [53]

Another method is laser cladding, which is a coating method. It uses an automated probe with a laser beam and powder feeder, which work simultaneously for layer-by-layer production. Laser supply the energy required to melt the powder and deposit it into the substrate. The advantage is using a laser with a small spot size so that heat affected zone remains shallow, which prevents solidification problems like cracks. By coating, extraordinary properties of the HEAs may contribute to the final properties. Zhang et al. fabricated FeCoNiCrCuTiMoAlSiB$_{0.5}$ HEA coating by laser cladding, which has a hardness value of 1180 HV and elastic modulus of 187.1 GPa [54]. These extreme values can be explained by the combination of the nature of the HEA and the features of the additive manufacturing. The contribution of 10 elements highly distorted the lattice, especially with the interstitial boron addition, while additive manufacturing provides rapid solidification rates, resulting very fine grains.

The essential challenge for the additively manufactured HEAs is melting point difference among the constituent elements, especially for the RHEAs. Parameter optimization and alloy design must be adjusted accordingly. Also, post treatments, like annealing or HIP are compulsory for the homogenization of the structure, since the as-built state has a built orientation, unlike the as-cast state.

2.3   Microstructure of HEAs

2.3.1   Phases

By microstructural definition, HEAs consist of single or dual solid solution phases. These simple disordered phases are BCC and/or FCC depending on VEC of the system. VEC of a HEA can be calculated by rule of mixture of the valence values of the constituent elements (Eq.2.7). It has been found that when VEC<6.87, solid solution is BCC, while it is FCC when VEC>8. HEA consists of a dual FCC+BCC phase when the VEC is in the range of 6.87-8 [55].

$$VEC = \sum c_i \, (VEC)_i \qquad \qquad \text{Eq.2.7}$$

Depending on their application area, HEAs can be divided into 2 subgroups, which show different microstructures: transition metal HEAs (THEA) and refractory HEAs (RHEA). THEAs and RHEA are both designed for sufficient mechanical performance, but the difference is their application temperatures. Various transition metals (Cr, Mn, Fe, Co, Ni and Cu) are used for THEAs, while RHEAs consist of group IV, V and VI metals (Ti, V, Cr, Zr, Nb, Mo, Hf, Ta and W). There are many studies on the addition of B, C, N, Al and Si elements into both groups to improve properties [3], [56], [57].

Considering the valence electron values of component elements, THEAs can be in FCC and/or BCC intervals. On the other hand, RHEAs are definitely in the BCC range (VEC<6.87) because contained elements have valence of 4, 5 or 6, whose average is under 6.87. While VEC approaches 4, HCP precipitates are stable at low temperatures, which is the crystal structure of group 4 metals (Ti, Zr and Hf). HCP precipitates in RHEAs are rich in Ti and Hf and their appearance, size and distribution can be adjusted. For instance, very fast cooling rates can suppress the formation of secondary phases and change mechanical properties[58], [59].

When the formation parameters like ΔH_{mix}, Ω and δ are not satisfied, simple ordered structures such as B2 and $L1_2$ can precipitate in the solid solution matrix. It correlates with the thermodynamics, since large negative ΔH_{mix} leads to ordering. They are solid solutions whose structure is in the order of intermetallic compounds. However, since they are not completely ordered, they can be called as partially ordered structures. It is very challenging to analyze these intermetallic phases in case of the co-existence of ordered and disordered types of the same structure due to overlapping XRD peaks. For instance, BCC and ordered B2 [60] or FCC and ordered FCC ($L1_2$) are observed simultaneously on the same HEA [51].

Also, complex ordered intermetallic phases, like Laves (C14 or C15) or Sigma (σ), can also be observed, especially in RHEAs. The presence of Laves phase is often undesired since it highly decreases the ductility, however it's morphology and size can be controlled by post-treatments. In the literature, it is reported that the addition of Cr into RHEAs causes increasing affinity to Laves phase formation, regardless of composition[61][62][63]. This is explained by two characteristics of Cr: The first one is excessive lattice distortion due to relatively small atomic radii of the Cr with respect to other refractory constituent elements and high values of mixing. The second one is tendency to ordered phases due to negatively large values of mixing enthalpy between Cr and other constituent elements.

2.3.2 Morphology

During the production of HEA via liquid state techniques, phase segregation generally occurs due to elemental complexity and wide melting temperature interval. HEAs produced with VAM generally have dendritic morphology in their as-cast state. Determination of which elements go to dendrite or interdendrite is governed by ΔH_{mix} and the melting temperatures of the constituent elements. Micro segregation, grain size and morphology can be controlled by processing parameters like solidification rate or post treatments. HEAs are accepted to be at nonequilibrium metastable state in as-cast form, thus their production is generally followed by hot isostatic pressing and/or annealing treatment to reach the equilibrium state even though there is not any segregation. It is possible to control microstructure by adjusting the heat treatment parameters. However, there are also as-cast HEAs, whose properties are sufficient to be used in industrial applications. There is no standard annealing treatment for all HEAs due to different compositions. However, the annealing temperature is generally accepted as above half of the melting temperature and treatment duration is relatively long (2-24 h) due to slow phase transformation and diffusion rates, in other words, sluggish kinetics. Especially for RHEAs, the structure cannot reach its equilibrium state, even after 24-hour annealing treatments due to the low diffusivity of heavy atoms.

A study on dual-phase (BCC+FCC) AlCoCrCuFeNi HEA shows the effect of temperature on microstructure and mechanical properties[42]. Heat treatments upon 645 °C increase the ratio of strong BCC phase; yield strength increase drastically around 1750 MPa. On the contrary, heat treatments over 645 °C increase plastic strain up to 27%. Heat treatment can also form IC phases, but it can be a desired microstructure in some cases. Excellent elevated temperature properties of RHEAs are related to the formation of Laves phases by different heat treatments[64].

2.4 Properties of HEAs

2.4.1 Mechanical Properties

Mechanical properties of the HEAs spread on an extensive range due to extensive combinations of compositions (Figure 2.14). Constituent elements determine variables like composition, phases, their fractions and morphologies, which are closely related to mechanical properties. Moreover, production and post-production methods may change the properties by controlling the microstructure. Optimization of these parameters during the alloy design stage assigns the desired microstructure and properties. For instance, the intermetallic compound (IC) phase formation is accepted as the reason for embrittlement and deterioration of mechanical properties for HEAs. Mechanical behavior also depends on the defects like vacancies, dislocations, twins and grains. Since the most common manufacturing technique for HEAs is liquid state production, initially products are in as-cast state. In this state, HEAs may have defects like segregation, pores and residual stresses. To eliminate them, different post-production thermo-mechanical treatments like homogenization or hot isostatic pressing (HIP) can be applied and they make significant changes on mechanical properties by increasing homogeneity across the microstructure. For instance, Kang et al. has shown that ultra-high-strength equiatomic WNbMoTaV HEAs produced by mechanical alloying and spark plasma sintering method exhibit different mechanical properties[65]. Mechanical alloying leads to very fine grain size (1.83µm) and oxide formation (the result of powder process), which create grain boundary strengthening and precipitation hardening, respectively. These additional mechanisms are not observed in the case of liquid state production. With the addition of the main mechanism, solid solution strengthening, a very high compressive yield strength of 2612 MPa is achieved, accompanied by 8.8% failure strain.
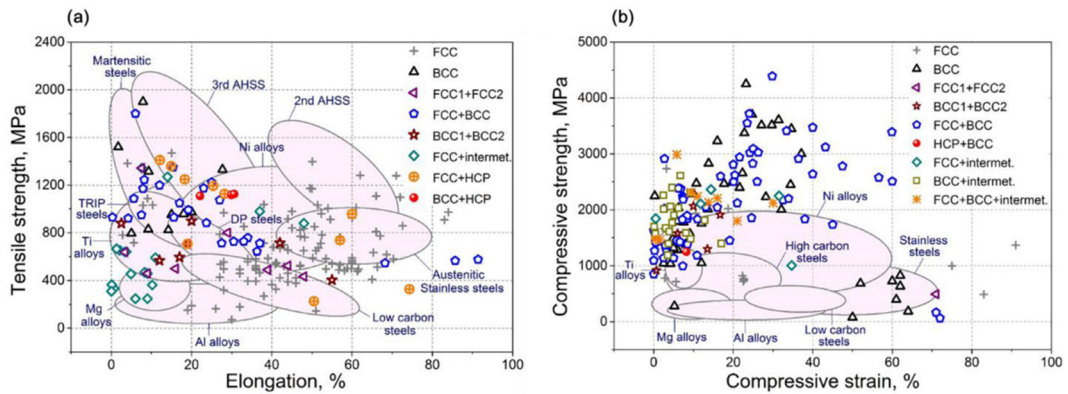
Figure 2.14. Review of reported HEAs and CCAs in the literature a) Tensile strength vs. fracture elongation, b) Compressive strength vs. compressive strain [66]

Classification of HEAs into two groups as Transition HEAs (THEA) and Refractory HEAs (RHEA) is valid for both microstructure and property aspects. THEAs behave in a ductile manner due to their FCC structure and exhibit a good combination of strength and ductility. However, their mechanical properties are only advantageous from cryogenic temperatures to around 600 °C, above which a sudden drop of strength occurs, similar to Nickel-based alloys[67], [68]. RHEAs exceed this limitation, while having less ductility and are designed to show satisfying performance at elevated temperatures.

2.4.1.1 Mechanical Properties of Refractory HEAs

Refractory high entropy alloys are expected to replace Nickel-based alloys and become the future materials for elevated temperature applications. Currently, Ni-based superalloys have the best creep and environmental resistance at elevated temperatures, among other refractory materials. RHEAs are a special subgroup that shows structural stability and resistance to thermal softening at elevated temperatures. These properties originate from two characteristics; One of them is sluggish diffusion kinetics, which is additionally supported by high density of

RHEAs. The other one is the low driving force to eliminate defects. The free energy requirement is small, since defect-free lattice of HEA is already highly distorted.

Mainly, there are 9 elements with high melting temperature, which are used for the production of RHEAs: Ti, V, Cr, Zr, Nb, Mo, Hf, Ta, W. Also, the substitution of these 9 elements by lighter ones (like Al and Si) will lead to better ductility and lower density[69]. Studied alloys are generally evaluated under as-cast conditions, also sometimes with the addition of annealed and HIP + annealed states.

Since the main 9 elements belong to groups IV, V and VI; their valence electron values are 4, 5 and 6, respectively. Therefore, possible RHEA will definitely have one or two BCC structure(s) instead of FCC. Similar to conventional BCC alloys, they have nonplanar screw dislocations, which require high-stress levels to glide, so that they are relatively stronger than FCC alloys[70]. There are also possibilities of having extra intermetallic phases like Laves, when Cr and/or V are present in alloy due to their relatively small atomic size and negatively large ΔH_{mix} values.

The biggest problem of RHEAs is the lack of room temperature ductility due to BCC structure, which brings high strength. That is the reason for the existence of a few publications about tensile properties and cold-rolling behavior of RHEAs. To overcome this problem, electron theory is considered in 2014[71]. The application of this theory showed that compositions with VEC value under 4.4 show intrinsic ductility[19]. Lowering the VEC does not have any effect on the type of structure since it is inevitably BCC for RHEAs. One study to use this theory was on TiZrHfNb RHEA[22]. The BCC alloy was prepared by arc melting and casting method, then homogenized at 1300 °C for 6 hours. UTS value is 879 MPa in the as-cast state and increases to 969 MPa in the homogenized state with 14.9% elongation. Additional studies showed that, VEC theory brings a tolerable amount of ductility with fracture strain between 8% and 18%[19], [21], [22].

Generally, interstitial elements (B, C, N or O) diffusive into grain boundaries and leads to embrittlement. Moreover, oxygen addition generally leads to undesired metallic oxide formation, which is another reason of embrittlement. However, it is recently revealed that a small amount of oxygen (2 at%) addition improves the strength and ductility simultaneously[20]. The key point of the study is that oxygen leads to the formation of ordered complex oxygen clusters instead of interstitial form or simple brittle metallic oxides. The dislocations cannot cut or bow these Ti-Zr-O rich clusters and dislocations change the movement characteristics from planar to wavy slip and create Frank-Read sources. These features create dislocation multiplication and pinning, which leads to appearance of dipolar walls and eventually delays necking and failure. This change in the mechanism leads increase yield strength from 750 MPa to 1110 MPa (48%) and elongation from 14.2% to 27.7% (95%) at the same time. This improvement can be seen in Figure 2.15 from base alloy (black) to oxygen-doped alloy (red), which is not valid for nitrogen doping (blue) due to different deformation mechanism. Another importance of this scientific progress is overcoming the strength-ductility trade-off.
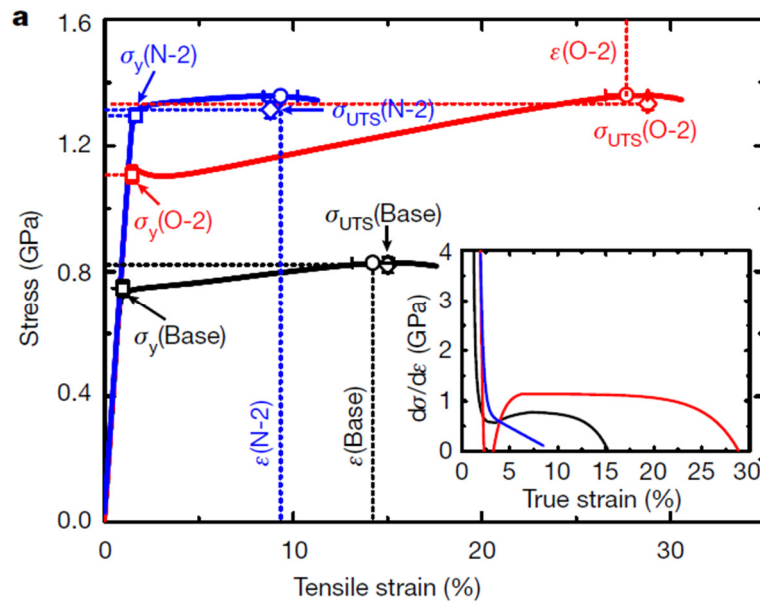
Figure 2.15. Tensile stress-strain curve of base (black) and oxygen-doped (red) alloys[20]

31

Yield stress values on different operating temperatures on different RHEA studies are plotted in Figure 2.16 [14]. Ni-based superalloys namely Inconel718 and Mar-M247 are also added for comparison. Naturally, yield stress decreases with increasing temperature for every alloy. It is evident that some of the RHEA compositions show better performance than conventional Ni-based superalloys.
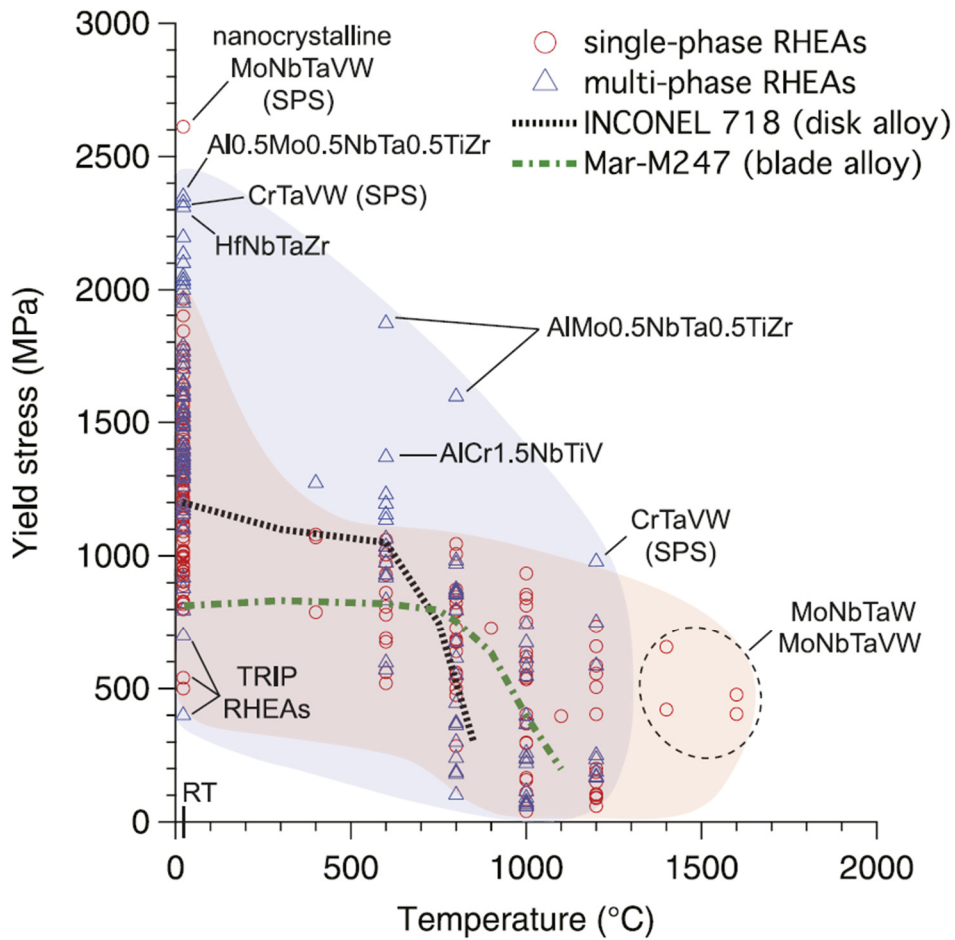
Figure 2.16. High temperature yield stress values of RHEAs and Ni-based superalloys[14]

2.4.2   Thermal Properties

HEAs show high structural stability at elevated temperatures and there are 2 factors for that. The first one is one of the 4 core effects of HEAs: sluggish kinetics. Especially for RHEAs, additional support of high atomic weight and melting temperature promotes the deceleration of the kinetics, which includes phase transformations, diffusivity, and grain growth. The second one is reduced driving force to eliminate defects. The energy difference between states with and without defects is low since the stable state is already severely distorted due to atomic size variation through the lattice. Therefore, the tendency to microstructural change is low even at high temperatures.

As explained above, the nature of the HEAs is highly suitable for HT applications. They can be considered for high temperature applications as an alternative to Ni-based superalloys for whose strength suddenly drops around 600 °C. HEAs are proposed to be resistant to softening due to their sluggish kinetics. In 2010, Senkov proposed the RHEA concept with NbMoTaW and VNbMoTaW alloys [16], [17]. Both alloys have a single BCC structure with dendritic morphology, which consists of W enrichment and Nb depletion. Quaternary and quinary alloys show 1058 MPa and 1246 MPa yield strength and exceptional hardness values of 454 HV and 535 HV at room temperature, respectively. As shown in Figure 2.17, they yield at high stress levels of 451 MPa and 656 MPa at 1400 °C, which is the melting point of Inconel718. Most importantly, HEAs do not soften and lose their strength above 600 °C, like Ni-based superalloys. Furthermore, both NbMoTaW and VNbMoTaW HEAs keep their dendritic BCC structure after deformation at 1400 °C, indicating a high tendency for phase stability. However, at room temperature, they fail in a brittle manner with undesired quasi-cleavage mode at strain of 2.1% and 1.7%. Even though they exhibit improved ductility at higher temperatures, low temperature brittleness limits their application at room temperature.
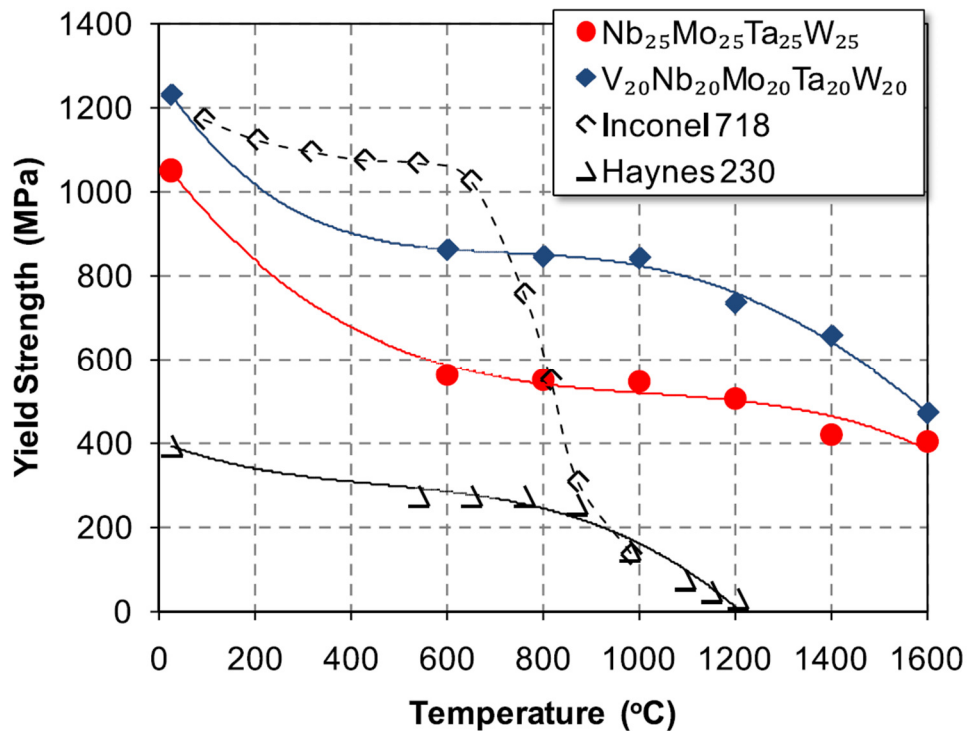
Figure 2.17. The comparison of the thermomechanical behavior of first two RHEAs and Ni-based refractory superalloys[17]

In another study, thermal properties of Aluminum containing $AlMo_{0.5}NbTa_{0.5}TiZr$ RHEA are investigated[64]. High mechanical performance with low ductility is observed at room temperature, with 2000 MPa yield strength, 591 HV hardness and 10% fracture strain. The alloy consists of 2 BCC structures with very close lattice parameters, which is formed as coherent, nano-lamellar mode inside equiaxed grains as shown in Figure 2.18. Microstructural investigation after the deformation revealed that the interface boundaries between lamellar structures obstruct the dislocation motion and bring a high strength at 1200 °C, even though this alloy contains Aluminum with a low melting point. Furthermore, $AlMo_{0.5}NbTa_{0.5}TiZr$ keeps high strength at temperatures up to 1200 °C, due to high thermal stability and no intermetallic formation.
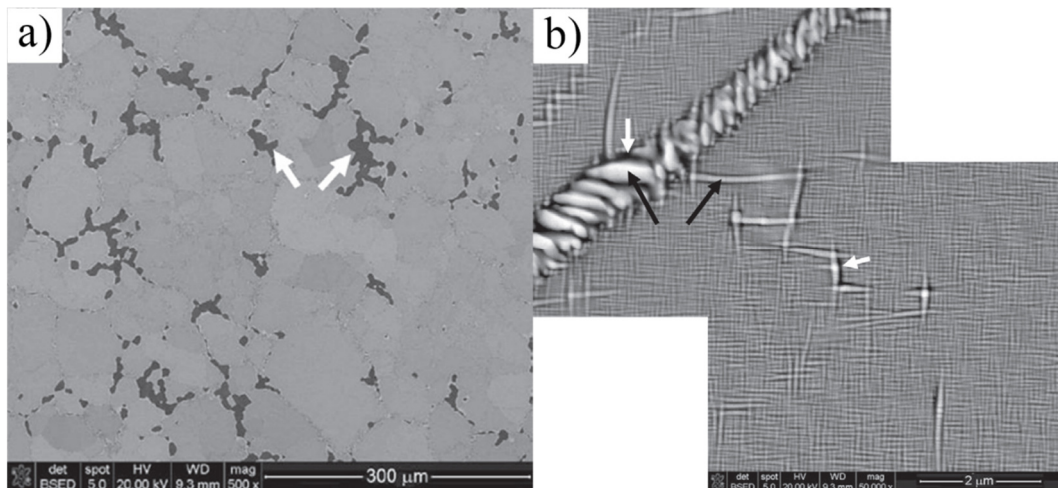
Figure 2.18. SEM-BS image of AlMo$_{0.5}$NbTa$_{0.5}$TiZr a) equiaxed grains b) basket-like lamellar structure inside the grains [64]

2.4.3   Radiation Properties

Nuclear energy is accepted as an alternative energy source, becoming popular with the advancements in radiation materials science in recent years. Currently, various materials are being used at reactors, such as ferritic/austenitic/martensitic steels, Nickel and Zirconium based superalloys, ceramics, and composites. However, they can withstand up to a specific dosage level and their engineering lifetimes are limited. The development of an advanced nuclear material with improved operating conditions would maximize energy efficiency and safety while minimizing operation costs and amount of toxic waste. Alternatively, improved radiation properties are crucial for particle accelerators, maintenance of nuclear waste and ion implantation applications[72], [73].

Radiation can be introduced into a system as neutrons, ions, electrons, or gamma rays. The main event of the irradiation is dislocating an atom from its lattice site (since they are metallic materials) with the energy transfer by any type of radiation

that supplies the threshold displacement energy. The target atom, called primary knock-on atom (PKA), leaves a vacancy on its site, and interstitially locate in another location, and this defect couple is called Frenkel pair. PKA creates a collision cascade and disturbs the other lattice atoms before locating interstitially. Branching into sub-cascades creates more defects than one cascade with the same total energy. For lighter metals, it is easier to turn into sub-cascades, thus an exponential increment in the defect formation [74]. During irradiation, the vacancy defects form clusters and eventually voids. All the microstructural changes and evolved defects such as defect clusters, dislocation loops and voids are driven by point defect formation, migration, and accumulation. Based on this event, the physical effects of irradiation are swelling (volume increase), change in shape, phase transformation and segregation. Depending on the dosage, these changes might increase the hardness by the factor of 5-10 and reduce the ductility leading to embrittlement[75].

To represent the effect of radiation, a term called displacement per atom (dpa) is used. Dpa is a better representation of the effect of radiation than the fluence. Dpa is a function of depth (x) can be defined as in Eq.2.8, where $F_d(x)$ is the energy distribution function, N is the number of displaced atoms, E_d is the threshold energy to displace an atom from its site and Φ is the fluence of the exposed radiation.

$$dpa(x) = 0.4 \frac{F_d(x)}{N \cdot E_d} \Phi$$

Eq.2.8

In Figure 2.19 three property changes are given with respect to displacement damage. Even though they have a certain correlation, nature of the damage is not uniform and depends on the materials properties.
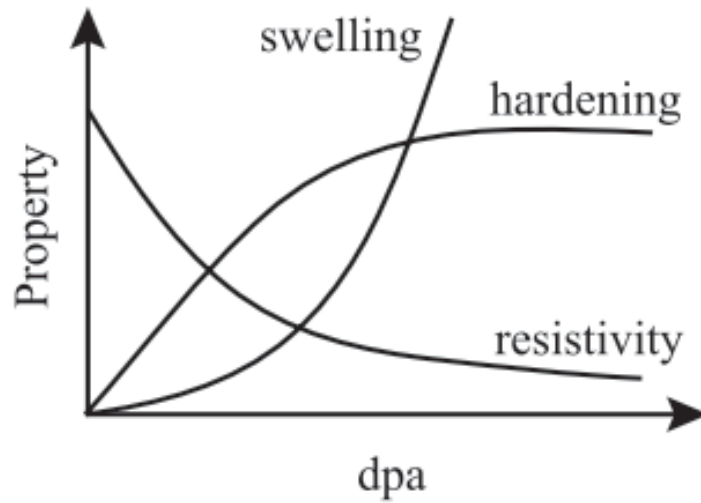
Figure 2.19. The change of the properties with respect to displacement per atom (dpa)[75]

HEAs are expected to be next-generation radiation-resistant materials due to their chemical complexity and unique properties[24], [28], [30]. The superior radiation resistance of HEAs is attributed to natural characteristics of HEAs: high mixing entropy, sluggish diffusion, severe lattice distortion and self-healing effect. First of all, high-temperature phase stability and strength are essential to attain a material with high radiation resistance since defect production by irradiation can be reduced. At elevated temperatures, large entropy of mixing increases the phase stability of the solid solution phase by reducing the Gibbs free energy. Therefore, improved phase stability at elevated temperatures reduces radiation degradation.

Sluggish kinetics and distorted lattice of HEAs are expected to stabilize defect migration and delay their coarsening. Several studies showed lower amount of dislocation loops and radiation-induced segregation related to these two core effects[23]–[27]. Radiation-induced segregation (RIS) is the redistribution of the constituent elements due to increased defect concentration and mobility that is caused by irradiation at elevated temperatures. In 2017, a study on alloys FeCo, FeCoNi, FeCoNiCr and FeCoNiCrMn was conducted to understand the effect of

37

chemical complexity on the radiation properties[27]. The samples were irradiated with 3 MeV Ni^{2+} ions with a fluence of 5 x 10^{16} ions/cm² at 500 °C. Distribution, size and fraction of the defects showed that chemical complexity extends the incubation period and delays the growth of faulted loops. Figure 2.20 shows that the size of the dislocation loops decreases with increasing chemical complexity. Also, the addition of principal elements slows down the kinetics and sluggish kinetics of HEA drastically suppressed the radiation-induced phase segregation. Moreover, increasing chemical complexity increases the distortion in the lattice, thus the transmittance of the energy slows down and the radiation damage is recovered by the self-healing effect.
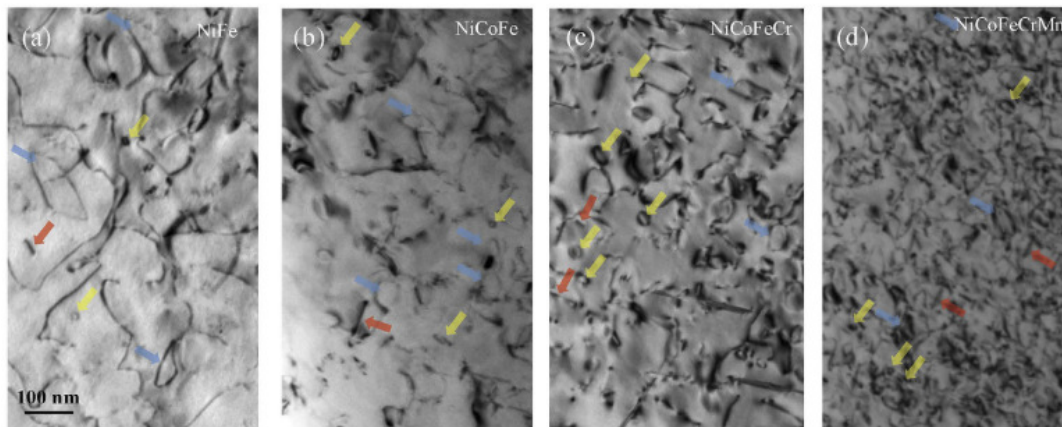
Figure 2.20. Bright-field images of the dislocation loops (Blue arrows are perfect loops, yellow arrows faulted loops and red arrows are edge-on faulted loops)[27]

There is also a unique phenomenon called self-healing in HEAs, which increases radiation resistance by lowering defect concentration[27]–[30]. A drastic decrease in the number of self-interstitial and vacancy defects (Frenkel pairs) are observed in HEAs, where these defects cause dislocation loops, volume swelling and eventually weakness in mechanical properties[30]. The origin of the self-healing effect is explained by the distorted lattice of the HEAs. In addition to atomic displacements, particle irradiation causes local thermal fluctuations called "thermal

38

spikes". Thermal energy does not dissipate on the severely distorted lattice of HEAs as effectively as conventional alloys. The scattering of phonons causes the heat energy accumulation, decreasing the mean-free path of heat transfer and eventually amorphization. Therefore, thermal spikes lead to a local melting-cooling process, which results in recrystallization. This event highly decreases the defect concentration. This unique event makes HEAs a great candidate for nuclear applications. To demonstrate self-healing effect, in-situ microstructural evolution of TiVNbTa alloy and pure V are compared[76]. Both alloys are irradiated under 1 MeV Kr^{2+} ions at 50K and 773 K. The defect analysis revealed that, even though they have the same defect cluster size, defect density is three times higher for pure V. Reduced defect concentration is attributed to the self-healing effect, since TiVNbTa alloy has compositional complexity to decelerate heat transport compared to pure V.

For the case of RHEAs, in addition to all HEA features that contribute to radiation resistance, two more supportive effects can be counted. The first one is heavy atomic weight in comparison to conventional nuclear materials. For heavier atoms, the threshold energy of replacing an atom is higher, therefore, defect mobility is lower and branching of cascades requires more energy[74], [26]. The second one is having a BCC structure since they are more radiation damage tolerant than FCC structures[73], [77]. Having a close-packed structure, like FCC, results in larger and more stabilized defect clusters, which reduces the probability of defect annihilation. In other words, RHEAs having BCC structure, allow vacancy and interstitial defects to cancel out each other and decrease the defect concentration. Moreover, Molecular Dynamics (MD) simulations of the same irradiation conditions exhibit the difference in the defect morphology of Cu (FCC) and Fe (BCC) metals, whose atomic weight is close to each other[77]. As seen in Figure 2.21, BCC structure has more homogenously distributed defects, while FCC has more defect clusters due to coalescence of the defect. The difference is correlated

with experimental TEM observations and explained by higher stacking fault energy of BCC structure.
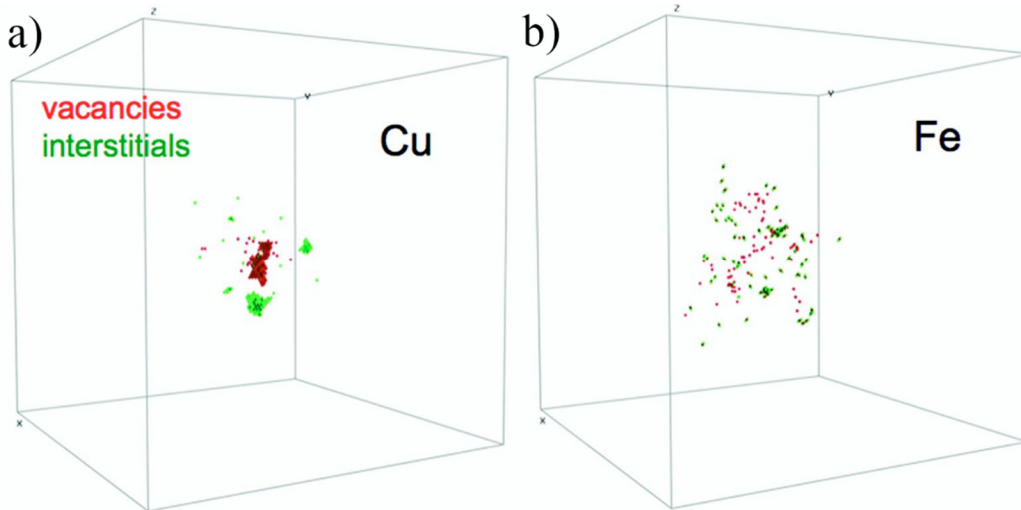
Figure 2.21. Comparison of defect configurations in a) fcc Cu and b) bcc Fe metals[77]

$Cr_{1.2}V_{2.5}MoWCo_{0.04}$ alloy is designed to investigate the microstructural behavior of RHEAs under irradiation[73]. The alloy consists of two BCC phases (V,Cr-rich and Mo,W-rich) with close lattice parameters in a dendritic morphology (Figure 2.22a). The combination of high mixing entropy, self-healing effect, BCC structure and presence of heavy elements results in a very low defect concentration. As a result, exceptional resistance against radiation hardening and embrittlement is observed. More importantly, even though the dendritic structure seemed as metastable, it contributed to stability by stabilizing the 1D and 2D defects, for instance by pinning dislocations. Therefore, radiation-induced segregation (RIS) did not occur, while to enrichment and depletion of the constituent elements is expected at elevated temperatures (Figure 2.22b).
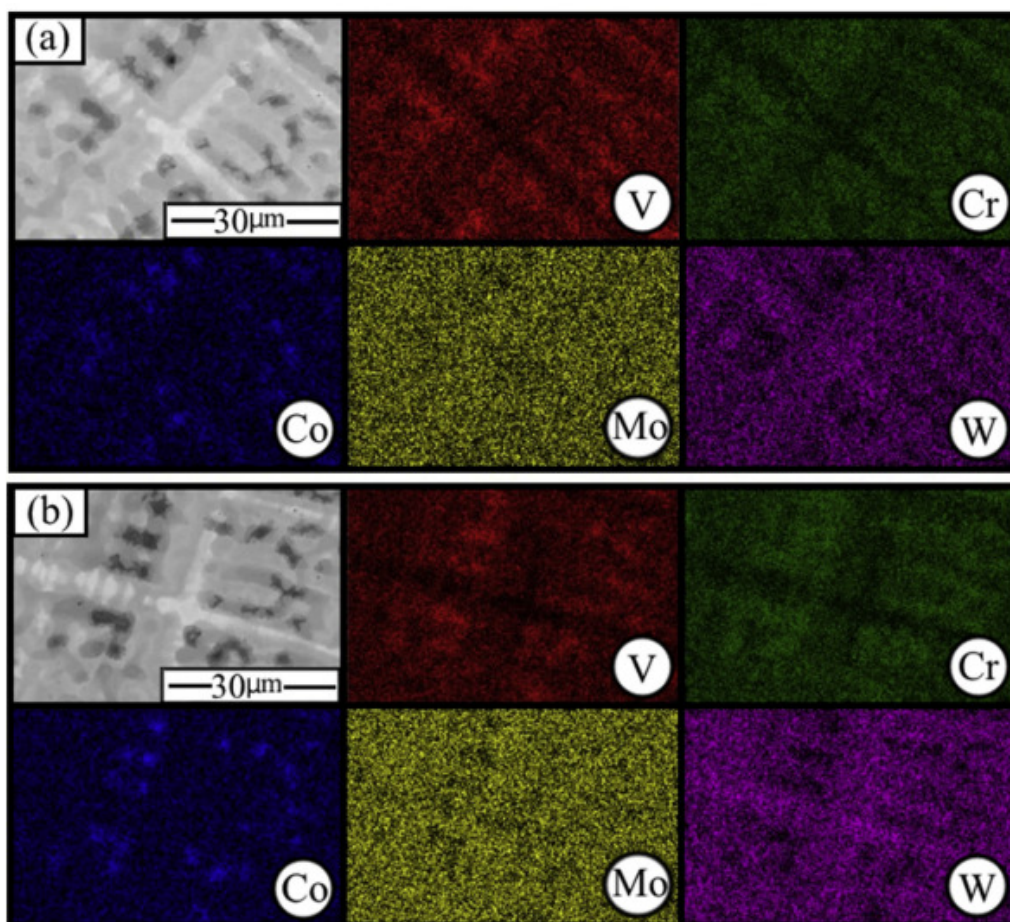
Figure 2.22. BS-SEM image and EDS mapping results of $Cr_{1.2}V_{2.5}MoWCo_{0.04}$ alloy a) before b) after irradiation [73]

CHAPTER 3

METHODS

3.1   Computational Methods

Before the production of alloys, final properties can be projected and adjusted by computational methods. Since HEAs offer unlimited compositions, it is essential to use computational methods for alloy design. Therefore, time, energy and material can be saved and alloy design process is accelerated.

Alloy design of HEAs requires specialized software to make complex calculations as HEAs have multi-component and more complex structures than conventional alloys. For instance, some thermophysical parameters like atomic size difference (δ) determines the microstructure, while it can be neglected for conventional alloys. Another example is phase diagrams, which need to be calculated for each HEA composition, while binary alloy systems have fixed phase diagrams showing the phase regions based on binary compositions. HEA Calculator and ThermoCalc software were used for this simulation to obtain thermodynamic and physical parameters, so that microstructure and final properties of the alloy can be projected.

Moreover, fluence and damage of the irradiation tests were computed by SRIM software. It is a special software for defining complex target materials and calculates the damage of irradiation under given conditions. The stoichiometry of each element can be adjusted for the modelling of the irradiated alloy.

3.1.1 HEA Calculator

Thermophysical parameters, such as atomic size difference (δ), enthalpy of mixing (ΔH_{mix}) and omega parameter (Ω) were calculated by Eq.2.1, Eq.2.2 and Eq.2.3, respectively. Theoretical properties such as melting temperature (T_m), density (ρ) and valence electron concentration (VEC) were calculated by rule of mixture, as shown in Eq.3.1. These properties are represented as X, while concentration of element "i" is shown as c_i in at% and X property of element "i" as X_i.

$$X = \sum c_i (X)_i \qquad \text{Eq.3.1}$$

To calculate all parameters, a simple calculation program, "HEA Calculator" is used, including all the properties of pure elements as a database[78]. The interface of software can be seen in Figure 3.1. It takes input as a composition and gives all the results as output. It also compares the results of δ, Ω and ΔH_{mix} with the ranges of HEA models and indicates if this composition will form a solid solution or not. If yes, the program states the type of crystal structure according to VEC theory.
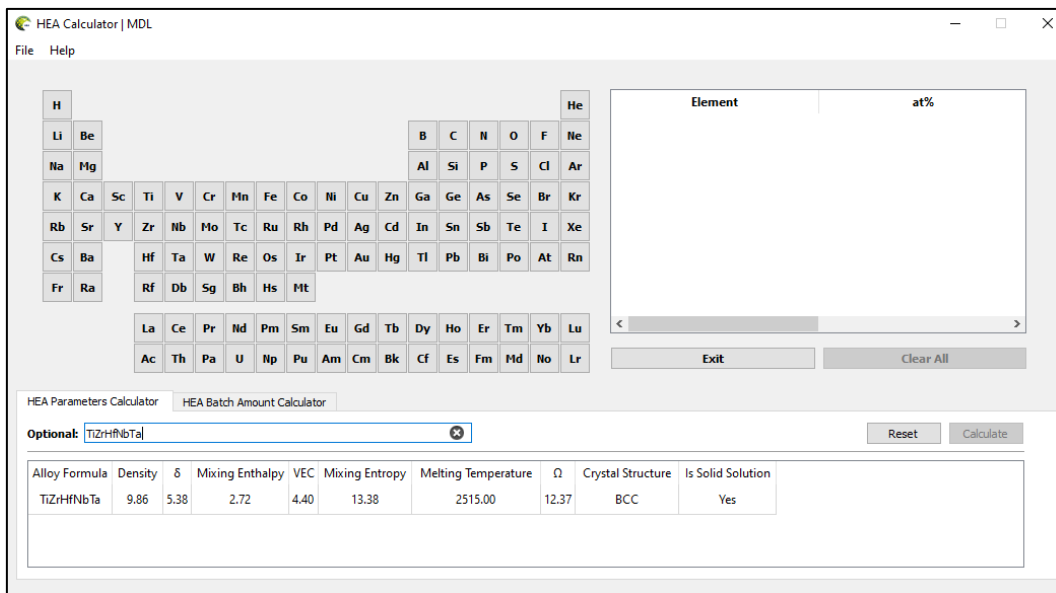
Figure 3.1. Screenshot of HEA Calculator software

3.1.2   CALPHAD Modelling

The final properties of any alloy directly depend on the microstructure. To estimate the microstructure at any temperature, phase diagrams are used before production. Since high entropy alloys have at least 5 component, quinary phase diagrams are too complex to plot and need to be calculated for each composition. Also, there are many binary, ternary and quaternary phase combinations to be considered. For this purpose, CALculation of PHAse Diagram (CALPHAD) method is used to plot phase diagrams by ThermoCalc software. It is reported to show reasonable agreement with experimental data on several studies[61], [79], [80]. CALPHAD method takes elemental composition and condition of the system (pressure, temperature) as input and calculates G-x plots for all possible phases for elemental, binary, ternary, quaternary and quinary systems (Figure 3.2). Then, according to the principle of Gibbs energy minimization, it plots the phase or property diagrams, providing information about present phases, their constituents and volume fractions at any temperature. Therefore, critical temperatures for phase transformations can be determined for any HEA system[81], [82]. For the CALPHAD calculations, the TCHEA2 v2.1 database of ThermoCalc, a specialized database that includes 20 elements and over 400 possible phase information, was used. This database consists of thermodynamic functions of Gibbs free energy as a function of the composition of the alloy, temperature and pressure[83].
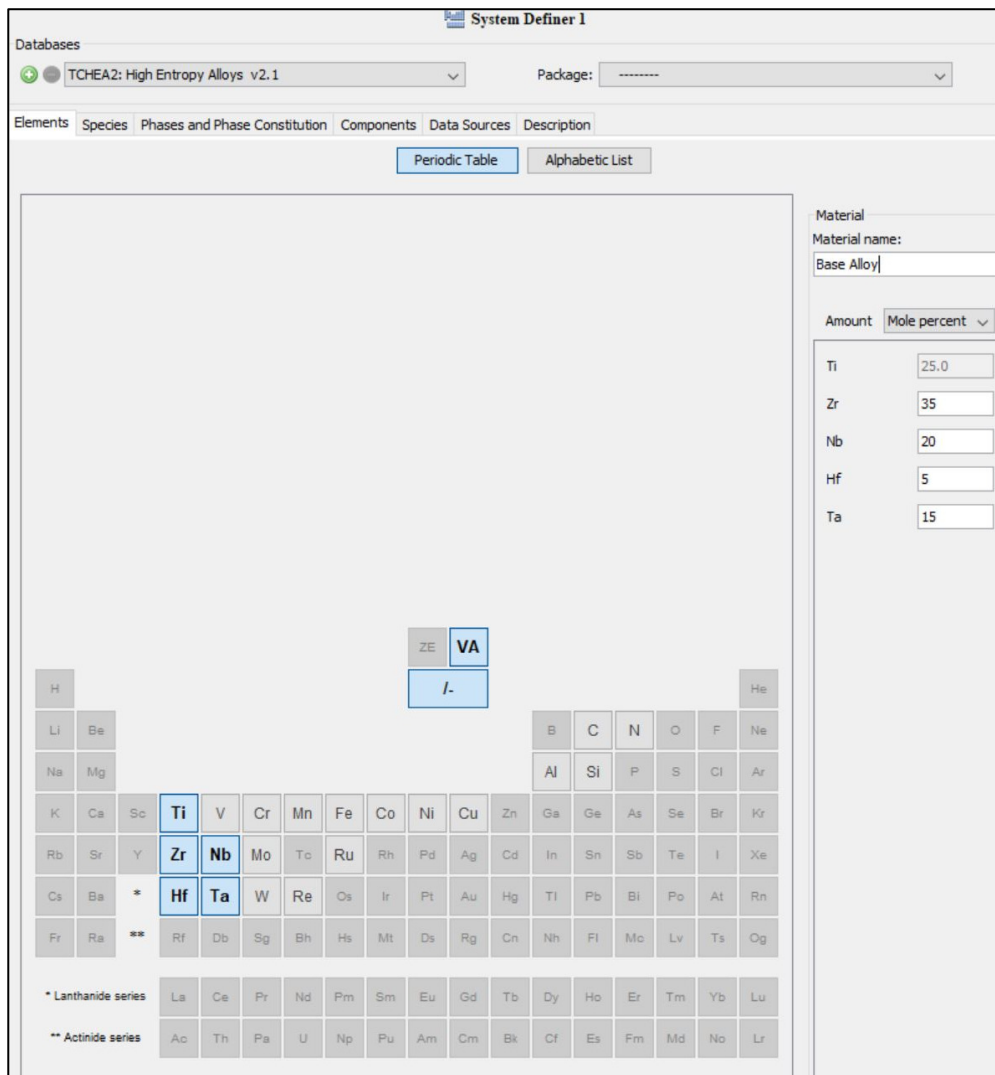
Figure 3.2. ThermoCalc software system definer

ThermoCalc also includes Scheil calculations, which can be used for simulating the non-equilibrium cooling behavior. It has two assumptions: no diffusion in solidified material and infinitely fast diffusion in liquid phase. The calculations take the composition as input and reveal the behavior of alloy and each element individually at each temperature step. The results show the existence and elemental distribution of possible phase segregations, originates from constitutional cooling.

3.1.3   Stopping and Range of Ions in Matter (SRIM)

The calculations that are related to radiation properties are conducted by SRIM (or TRIM) software. SRIM is a useful Monte Carlo based program to model the irradiation tests and calculate the damage on the target[84]. In other words, it simulates the path of each energetic ion inside the defined target by the interactions and energy losses on its path. By statistical algorithms, it can calculate final distribution of the projected ions according to the depth, damage on the target by atomic displacement, energy transferred to recoil atoms, number of vacancies that are created and number of backscattered ions. This information can be used to calculate the common unit of irradiation damage; displacement per atom (dpa).

SRIM enables to define the target layer by layer as pure element, compound or HEA (Figure 3.3). For the scope of this study, a single layer HEA with 3-micron thickness is defined with elemental stoichiometry and density. Threshold energy is accepted as 40 eV for all the elements of the target, based upon the ASTM E521 standards and lattice binding energy is accepted as zero[84]. The effect of oxygen into the modelling is checked and it is seen that oxygen doping does not make any significant difference in the modelling of damage and implanted ion distribution.

The projected ion is selected as iron (Fe) among the most commonly used ions (Fe, Cu, Ni) since it has the same crystal structure with the BCC target. The projection energy was 5 MeV. After the simulation, *Ion/Recoil Distribution* feature of the SRIM enables to calculate the total amount of Fe ions that are implanted into target. This calculation is critical since it is possible to see phase transformations if the amount of the projected ion exceeds a certain limit.
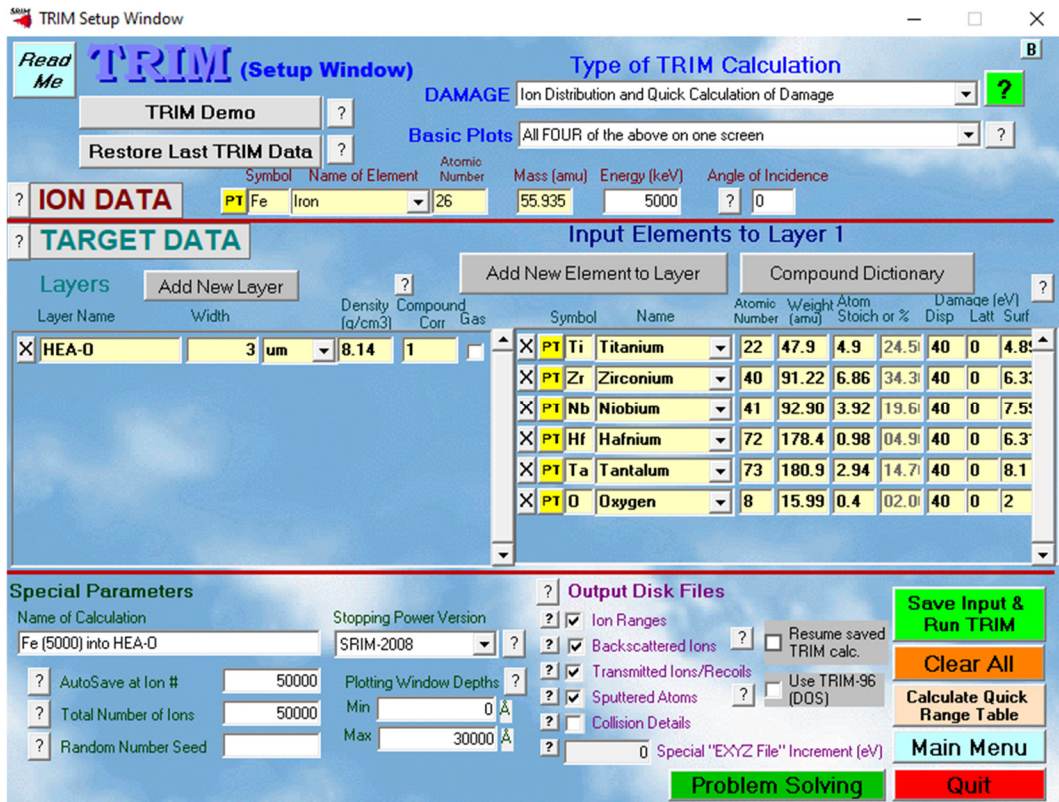
Figure 3.3. The user interface of the SRIM software with the input data

SRIM gives energy distribution function with respect to depth as the output. It can be converted into dpa vs depth according to Eq.2.8 by introducing the atomic density (N) and the fluence of the radiation (Φ). At this point, dpa levels were determined as 3, 10 and 30 and corresponding fluence levels were calculated so that irradiation experiments were conducted accordingly. In the end, the desired damage levels (dpa) can be positioned on the certain depths to be investigated.

3.2   Experimental Methods

Ti, Zr, Nb, Hf and Ta elements with purities over 99.5 wt% were used as raw materials in the form of pellets and granules. For the oxygen-doped samples, oxygen was introduced into the system as TiO_2 powder.

To produce designed HEAs MAM-1 Edmund Bühler model Vacuum Arc Melter was used (Figure 3.4). Since the torch temperature is high (>3000 °C), oxidation is a problem, so the chamber was flushed 3 times to decrease uncontrollable oxygen level. Also, smelting operations were conducted under a high purity argon atmosphere and with Titanium gettering for minimum oxygen and contamination. To improve chemical homogeneity, alloys were turned over and re-melted 5-8 times. Suction-casting equipment was attached under the crucible so that re-melted soft alloy can be sucked into the cylindrical copper mold with the power of a vacuum chamber. This attachment provided samples to have cylindrical geometry instead of button-like shape, so compression tests were conducted. For this purpose, samples were cut by precision cutter into dimensions of 4 mm diameter and 6 mm height.

The heat treatments were performed at the Protherm Tube Furnace at 800 °C and 1100 °C. After the vacuum level reached 10^{-2} mbar, samples were heated with a rate of 10 °C/min. When the treatments were over, the samples were furnace cooled down to room temperature.

For the irradiation experiments, samples were prepared as discs with the 3 mm diameter and 300-400 microns thickness. Then, they electropolished for a clean surface. Heavy ion irradiations were performed using the NEC 3.5 MeV Pelletron Tandem Ion Accelerator in the Ion Beam Materials Laboratory at LANL/USA. The samples were irradiated with the Fe^{++} ions with calculated dosages.

Figure 3.4. Vacuum Arc Melter a, b) Equipment c) Copper suction molds.

3.3 Characterization Tests

Phase information and structural analysis were performed by Bruker D8 X-Ray Diffractometer at room temperature and elevated temperatures (in-situ). Cu K_α radiation was used at 20^0-100^0 2θ range and the scanning rate was $1°/min$. High-temperature X-ray diffraction (HTXRD) tests were conducted with a platinum holder under a protective nitrogen atmosphere (Figure 3.5). The samples were precisely cut into dimensions of 1cm x 1cm and thickness was adjusted to 1 mm by grinding and polishing operations. Measurements started from room temperature, heated with 10 °C/min up to 200 °C, 400 °C, 600 °C, 800 °C, 1000 °C and 1100 °C. Holding time was 2 hours at each high temperature. Finally, the samples were quenched to room temperature, at which another measurement was taken.
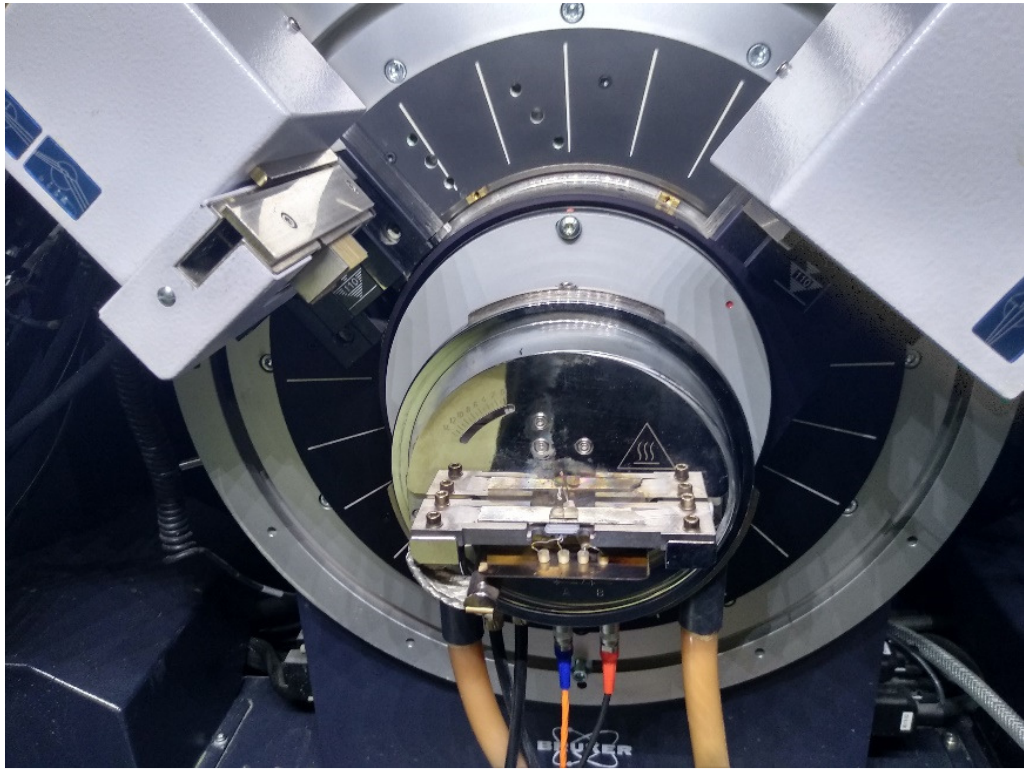
Figure 3.5. Bruker D8 X-Ray Diffractometer at HT-XRD configuration

Besides in-situ XRD analysis, Differential Scanning Calorimetry (DSC) was conducted for thermal analysis. DSC was in continuous heating mode under a protective nitrogen atmosphere with 10, 20, and 40 °C/min heating rates.

For the primary microstructural investigation, alloys were prepared for the optical microscopy by typical metallographic preparation. The cylindrical specimens were cut by a precision cutter. Subsequently, typical grinding, polishing, and etching (with Keller etchant) were performed. For the further structural analysis, samples were investigated under FEI-430 NanoSEM Scanning Electron Microscope (SEM) equipped with EDAX SSDD Apollo10 Energy Dispersive Spectroscopy (EDS) camera. The compositions of the alloys have been checked with EDS analysis, which was also used for EDS mapping for the elemental distribution.

Radiation damage was investigated under Transmission Electron Microscope (TEM). Samples were prepared using the Focused Ion Beam (FIB) technique with JEOL JIB4601F model equipment and investigated with JEOL-ARM200F TEM under 200 kV. In-situ TEM imaging and mapping analyses were performed at 300 kV with FEI TecnaiF30 Analytical TEM/STEM at Los Alamos National Lab/USA.

Mechanical properties were determined experimentally with micro and nano hardness and compression tests at room temperature. The micro hardness measurements were conducted using a Shimadzu-2 micro-Vickers hardness tester with a 1 kg load. Nano hardness measurements were taken from 10 random places to assess the radiation induced hardening. For the compression test, dimensions of cylindrical alloys were adjusted as 4mm diameter and 6 mm height. Since the samples have small dimensions for any extensometer, the strain values are given for the relative comparison of the stress values. The samples were deformed until the yield point is passed and deformation is corrected with measurements of the final dimensions. The compression tests were carried out under 100 kN load with a strain rate of 10^{-4}/s on four samples.

CHAPTER 4

ALLOY DESIGN & EXPERIMENTAL VERIFICATION

4.1   Results

4.1.1   Alloy Design

The motivation behind the adaptation of HEAs into refractory applications is their single solid solution structure without any intermetallic phase and promising thermal stability due to sluggish kinetics. Infinitely many compositions can be proposed randomly under the scope of HEA. However, there is no systematic study to maximize thermal properties and minimize the tendency for intermetallic compounds (IC). IC formation is crucial for refractory applications since it degrades mechanical and thermal properties drastically. For that purpose, a new alloy design approach will be developed based on the IC ranges of the two HEA models with the most accurate estimation percentages. All the models mentioned in literature, proposed SS ranges for HEA formation, but that SS ranges intersect with their IC ranges, which makes it not possible to know the exact formation probability of the IC phase. At this point, a critical uncertainty of structure occurs, which creates uncertainty for the properties and performance of the HEA.

Another critical design criterion is room temperature ductility, especially for RHEAs. To overcome embrittlement and IC formation tendency, the alloys have been designed, and properties have been tailored considering 4 aspects (Figure 4.1). The thermophysical parameters are adjusted for structural design and engineering concerns like density. Structural expectations are verified by

CALPHAD calculations, especially for elevated temperatures. VEC theory and oxygen addition are included to achieve room temperature ductility.
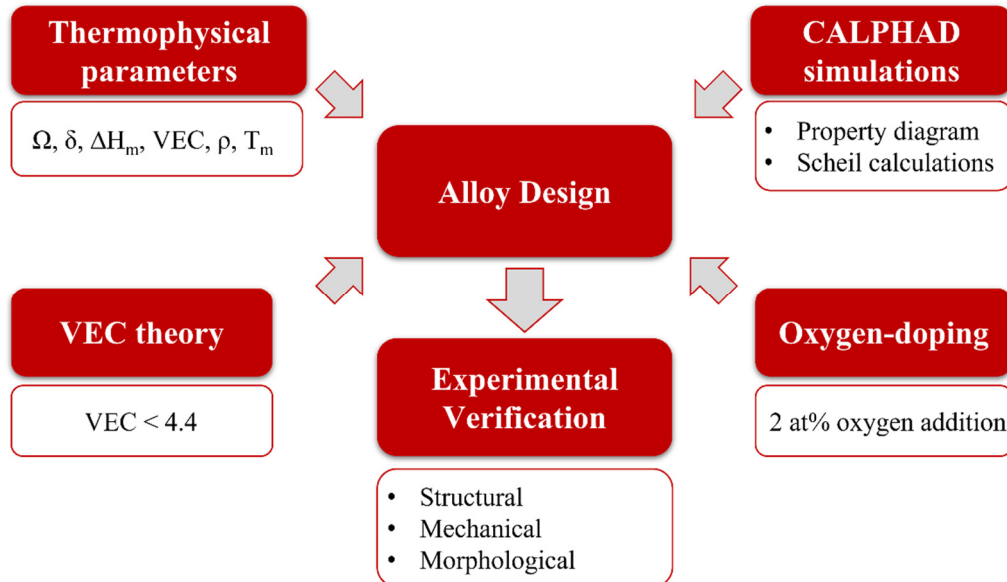
Figure 4.1. Overview of the alloy design strategy

4.1.1.1 Thermophysical Parameters

There are 9 elements (Ti, V, Cr, Zr, Nb, Mo, Hf, Ta and W) with high melting points to produce RHEAs. In this alloy design approach, all the possible 126 combinations of 9 elements in groups of 5 as equiatomic compositions were listed with their thermophysical properties (see Figure 4.2). A database was formed for the calculation of thermodynamic parameters and physical properties (ΔH_{mix}, δ, Ω, T_m, ρ and VEC). This database was composed of elemental (lattice parameter, density, Tm and VEC) and binary (ΔH_{mix}) properties of 9 elements, given in Table 4.1 and Table 4.2 taken from[81], [85]. ΔH_{mix}, ΔS_{mix} and Ω are calculated by Eq.2.2, Eq.2.5 and Eq.2.3, respectively, since rule of mixture (Eq.3.1) is not valid for thermodynamical terms. Mixing enthalpies are calculated by Miedema model[86].

Table 4.1 Properties of the constituent elements

Elements	Tm (K)	VEC	Density (gr/cm³)	Lattice parameter (Å)
Ti	1941	4	4.51	3.276
V	2183	5	6.11	3.039
Cr	2180	6	7.14	2.910
Zr	2128	4	6.51	3.582
Nb	2750	5	8.57	3.301
Mo	2896	6	10.28	3.147
Hf	2506	4	13.31	3.559
Ta	3290	5	16.65	3.303
W	3695	6	19.25	3.158

Table 4.2 Mixing enthalpies of the elemental binaries

	Ti	V	Cr	Zr	Nb	Mo	Hf	Ta	W
Ti	-	-	-	-	-	-	-	-	-
V	-1.65	-	-	-	-	-	-	-	-
Cr	-7.35	-2	-	-	-	-	-	-	-
Zr	-0.2	-3.63	-11.8	-	-	-	-	-	-
Nb	2	-1	-7.1	4	-	-	-	-	-
Mo	-3.5	0	0.4	-6	-5.6	-	-	-	-
Hf	0.15	-2.2	-9.15	-0.2	3.86	-3.87	-	-	-
Ta	1.4	-1	-6.65	2.74	0	-4.86	2.87	-	-
W	-5.64	-0.8	1	-8.9	-8.26	-0.2	-6.35	-7.3	-

	1	2	3	4	5	VEC	ΔS mix	Tm K	Density	δ	ΔH mix	Ω	√	Cost
1	Ti	V	Cr	Zr	Nb	4,8	13,39	2236	6,6	7,40	-4,60	6,51		98
2	Ti	V	Cr	Zr	Mo	5	13,39	2266	6,9	7,49	-5,72	5,30		91
3	Ti	V	Cr	Zr	Hf	4,6	13,39	2188	7,5	9,70	-6,08	4,81		323
4	Ti	V	Cr	Zr	Ta	4,8	13,39	2344	8,2	7,52	-4,82	6,51		139
5	Ti	V	Cr	Zr	W	5	13,39	2425	8,7	7,41	-6,56	4,95		90
6	Ti	V	Cr	Nb	Mo	5,2	13,39	2390	7,3	4,75	-4,13	7,75	√	99
7	Ti	V	Cr	Nb	Hf	4,8	13,39	2312	7,9	8,92	-3,91	7,91		330
8	Ti	V	Cr	Nb	Ta	5	13,39	2469	8,6	5,44	-3,74	8,85	√	147
9	Ti	V	Cr	Nb	W	5,2	13,39	2550	9,1	4,76	-4,93	6,93	√	98
10	Ti	V	Cr	Mo	Hf	5	13,39	2341	8,3	9,13	-4,67	6,71		324
11	Ti	V	Cr	Mo	Ta	5,2	13,39	2498	8,9	5,23	-4,03	8,29	√	140
12	Ti	V	Cr	Mo	W	5,4	13,39	2579	9,5	4,23	-3,16	10,93	√	91
13	Ti	V	Cr	Hf	Ta	4,8	13,39	2420	9,5	8,96	-4,09	7,91		372
14	Ti	V	Cr	Hf	W	5	13,39	2501	10,1	9,03	-5,44	6,16		323
15	Ti	V	Cr	Ta	W	5,2	13,39	2658	10,7	5,21	-4,80	7,41		139
16	Ti	V	Zr	Nb	Mo	4,8	13,39	2380	7,2	6,06	-2,49	12,78	√	104

Figure 4.2. First rows of the alloy scan, including 126 alloy candidates (all in appendix).

In order to determine the compositions forming a single solid solution, two models with the highest accuracy of estimation were used[39]. The model of Guo [34] accepts enthalpy of mixing (ΔH_{mix}) and minimizes it to stay within the limits of -11.6 kJ/mol and 3.2 kJ/mol in order to achieve an ideal-like completely random solution. On the other hand, the model of Yang [35] determines the Ω parameter, which should be larger than 1.1. This model takes mixing entropy (ΔS_{mix}) and melting temperature into consideration in addition to ΔH_{mix}. Both models accept the same topological/geometrical term, atomic size difference (δ), which is minimized to be lower than 6.6% for single solid solution tendency. Besides, design criteria of density below 10 g/cm^3 and melting temperature above 2000 °C have been added.

Most alloys containing Cr and V were eliminated due to a large atomic mismatch caused by their small atomic radii. While the calculated ΔH_{mix} values varied between -8 and 3 kJ/mol, except for Cr-containing alloys, the Ω parameter was larger than 1.1 for all cases because of their high melting temperature and low mixing enthalpy. On the other hand, high densities of W-containing RHEAs reduced the possible candidates to 20, as seen in Table 4.3.

Table 4.3 Possible RHEA candidates after first filtering (Cr-containing ones are shaded)

TiVCrNbMo	TiVCrMoW	TiVZrMoTa	TiCrZrNbTa	TiZrNbMoW
TiVCrNbTa	TiVZrNbMo	TiVZrMoW	TiCrNbMoTa	TiZrNbHfTa
TiVCrNbW	TiVZrNbTa	TiVNbMoTa	TiCrNbMoW	VCrNbMoTa
TiVCrMoTa	TiVZrNbW	TiVNbMoW	TiZrNbMoTa	VZrNbMoTa

Among these candidates, Cr-containing alloys were eliminated due to high negative values of ΔH_{mix} between Cr and other elements (Table 4.2) and relatively small radius of Cr (Table 4.1), which increases the atomic size difference parameter and creates distortion. Both effects increase the tendency towards forming the Laves phase, which is undesired and result in embrittlement and structural heterogeneity.

The remaining materials were further narrowed down based on their VEC value which is set to be below 4.4, in order to obtain some intrinsic ductility[19]. Therefore, group IV elements (Ti, Zr, Hf) are selected over group VI elements (Mo and W) to lower the VEC. With the addition of two group V elements with the highest melting points (Nb and Ta), the alloy system was determined to be Ti-Zr-Nb-Hf-Ta. The stoichiometry was further optimized as $Ti_{25}Zr_{35}Nb_{20}Hf_5Ta_{15}$ to maximize the melting temperature while staying in the solid solution range. The properties of the base alloy, such as lattice parameter, density, and melting temperature, are calculated based on the rule of mixtures as 3.406 Å, 8.28 g/cm^3, and 2117 °C, respectively (Table 4.4).

Table 4.4 The thermophysical properties of the base alloy ($Ti_{25}Zr_{35}Nb_{20}Hf_5Ta_{15}$)

Ω	δ	ΔH_{mix} (kJ/mol)	ΔS_{mix} (J/mol.K)	T_m (°C)	Density (g/cm^3)	VEC	a (Å)
10.15	4.54	2.88	12.2	2117	8.28	4.35	3.406

Further mechanical improvement is maintained by oxygen doping, which improves the strength and ductility at the same time by changing the dislocation movement mode with a small amount of addition (2 at%)[20]. Therefore, the designed composition was adjusted as 98 at% of the alloy, and 2 at% oxygen to form the oxygen-doped alloy. Designed ($Ti_{25}Zr_{35}Nb_{20}Hf_5Ta_{15}$) alloy is denoted as base alloy (BA) and ($Ti_{25}Zr_{35}Nb_{20}Hf_5Ta_{15}$)$_{98}O_2$ alloy is denoted as oxygen-doped alloy (OA).

4.1.1.2   CALPHAD

In addition to the thermophysical calculations, CALPHAD method was used for investigating the phases formed and their fractions. CALPHAD simulations have been performed only for the base alloy since oxygen is not included in the HEA database. The property diagram shows the predicted phases and their fractions up to 2200 °C in Figure 4.3a. $Ti_{25}Zr_{35}Nb_{20}Hf_5Ta_{15}$ composition has a solidus temperature of 1740 °C and a liquidus temperature of 1900 °C. There is a wide single-phase BCC region between 970 °C (solvus) and 1740 °C (solidus), indicating high thermal stability, which was one of the aims during alloy design. Thus, the existence of single-phase BCC in a wide gap makes this composition a good candidate for refractory applications above 1000 °C. Upon cooling, under 970 °C, a new BCC phase is stable (labeled as BCC#1) and coexists with BCC#2. While their phase fractions are 26% BCC#1 and 74% BCC#2 at 800 °C, BCC#2 is not stable below 540 °C. Also, the property diagram shows the HCP phase between room temperature to 600 °C. However, the formation of this phase is expected to be obstructed by sluggish kinetics as a typical HEA behavior.

For the investigation of non-equilibrium solidification, Scheil simulation was used between liquidus and solidus temperatures (Figure 4.3b). Scheil condition assumes zero diffusion in solidified material and infinitely fast diffusion in the liquid phase, showing a tendency to segregation due to constitutional cooling[87]. The results

showed the formation of a single BCC phase during the complete solidification. Solid and dotted lines represent the non-equilibrium (Scheil) and equilibrium solidification, respectively. The absence of any change in the slope indicates that no other phase formed during solidification. An early tendency for phase segregation starts at 1850 °C. Moreover, increased distancing of solid and dotted lines indicates the segregation, making the expected microstructure dendritic[81].
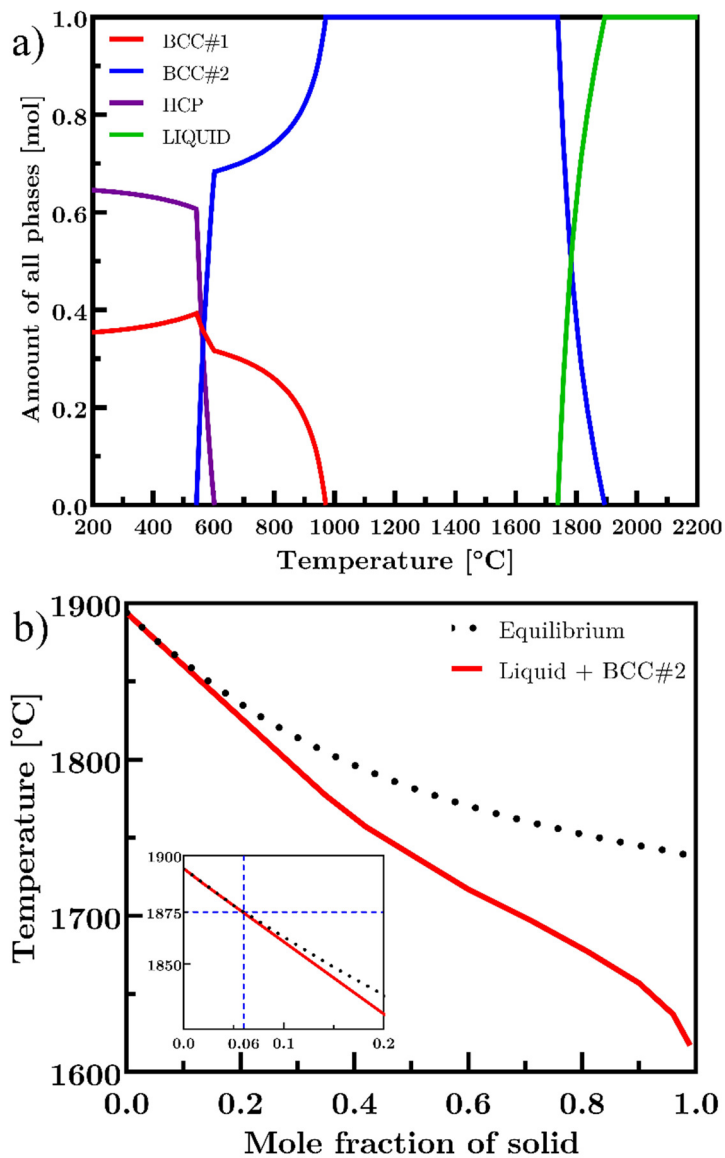
Figure 4.3. CALPHAD results of the base alloy a) property diagram b) Scheil diagram

For the investigation of the segregation behavior, the elemental composition of the liquid phase during non-equilibrium is plotted (Figure 4.4). During solidification, depletion of the elements with the highest melting points, namely Nb and Ta, from the liquid phase can be detected, while the liquid phase is enriched in Ti and Zr simultaneously. The amount of Hf remains the same during the solidification.
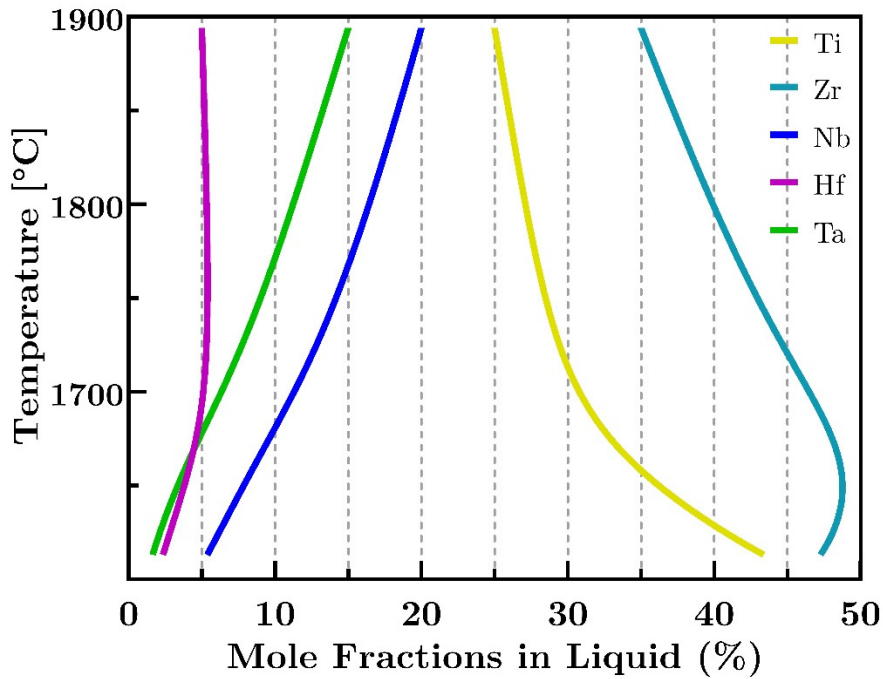
Figure 4.4. The composition of the liquid during non-equilibrium cooling

Furthermore, the compositional distribution of the BCC#1, BCC#2 and HCP phases are plotted in Figure 4.5. It is obvious that, nearly all of the Ti, Zr and Hf tend to form HCP phase, which is deficient in Nb and Ta. BCC##1 is enriched in Nb, Ta and slightly Ti, while BCC#2 is enriched in Ti, Zr and Hf by calculations.

Finally, Gibbs free energy of the base alloy is plotted in Figure 4.6. According to Eq.2.4, the temperature is expected to increase the entropic term and stability of the mixed solution. As expected, negatively increased results of Gibbs free energy indicated the increased stability of HEA formation at elevated temperatures.

60
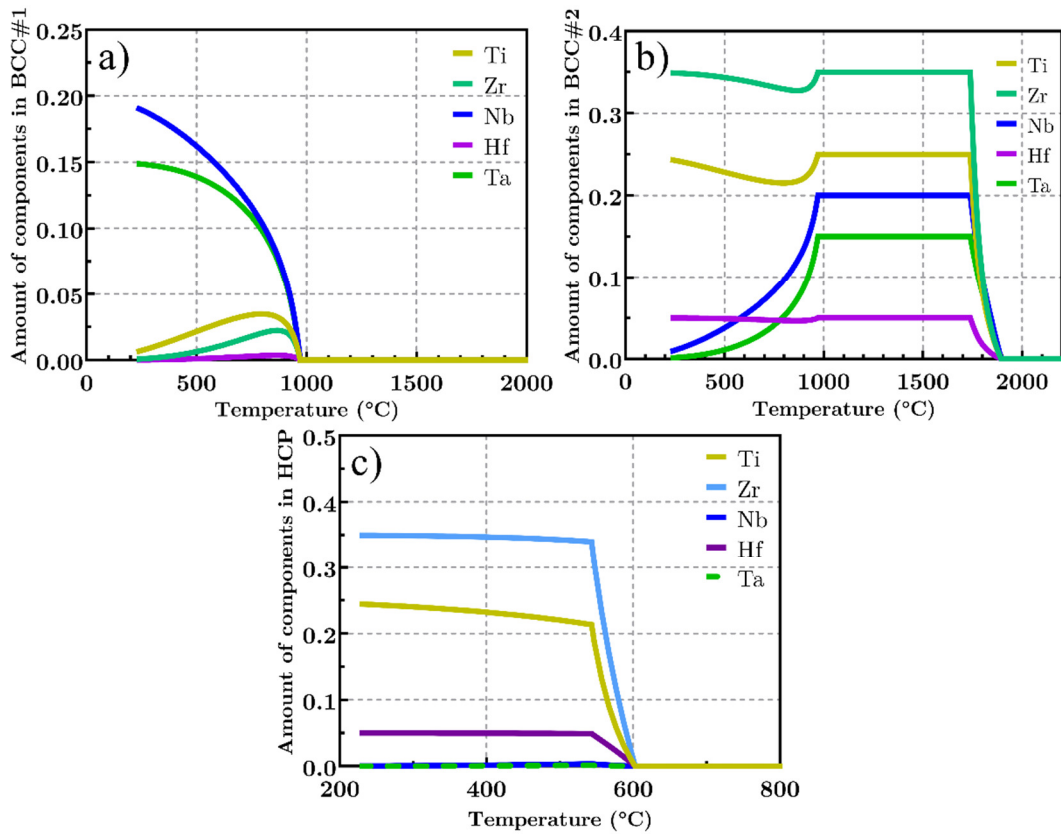
Figure 4.5. The elemental composition (mole) of the a) BCC#1 b) BCC#2 c) HCP phases
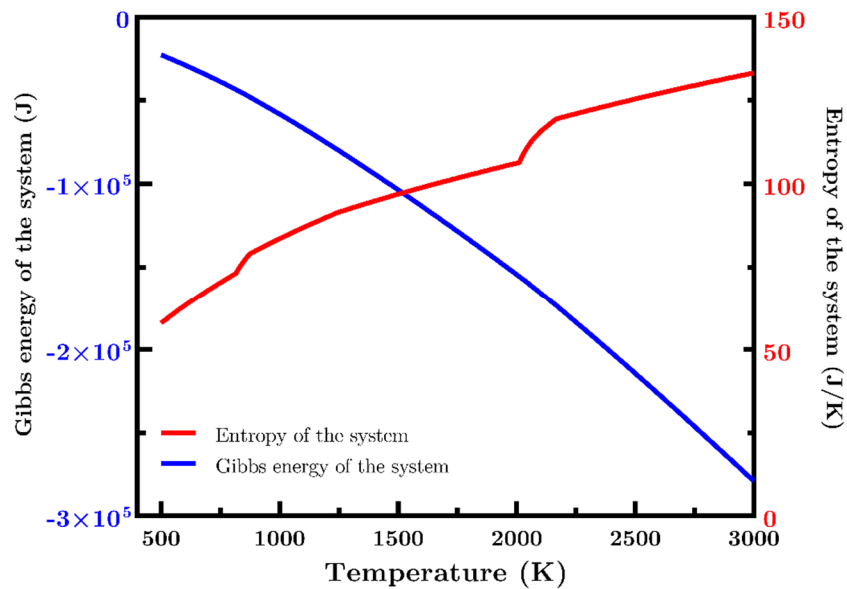
Figure 4.6. Gibbs free energy and entropy of the base alloy

4.1.2 Microstructure

Designed samples of base alloy (BA) and oxygen-doped alloy (OA) were produced by vacuum arc melting. In Figure 4.7a and b, optical microscopy images show the dendritic microstructure for BA and OA, a typical RHEA morphology in the as-cast state without any post-production heat treatment. It should be noted that the morphology becomes finer towards the outer regions of the sample due to faster cooling rates, resulting in a variation between the size of the dendrites between 5-30 microns. Figure 4.7a and b are taken from the middle parts, do not show any considerable difference in their morphology, like the shape and size of the dendrites. Backscattered electron (BS) images of OA represent compositional contrast in Figure 4.7c. The dendrite arms aligned in the direction of solidification are brighter than the interdendrites due to elements with higher atomic numbers.
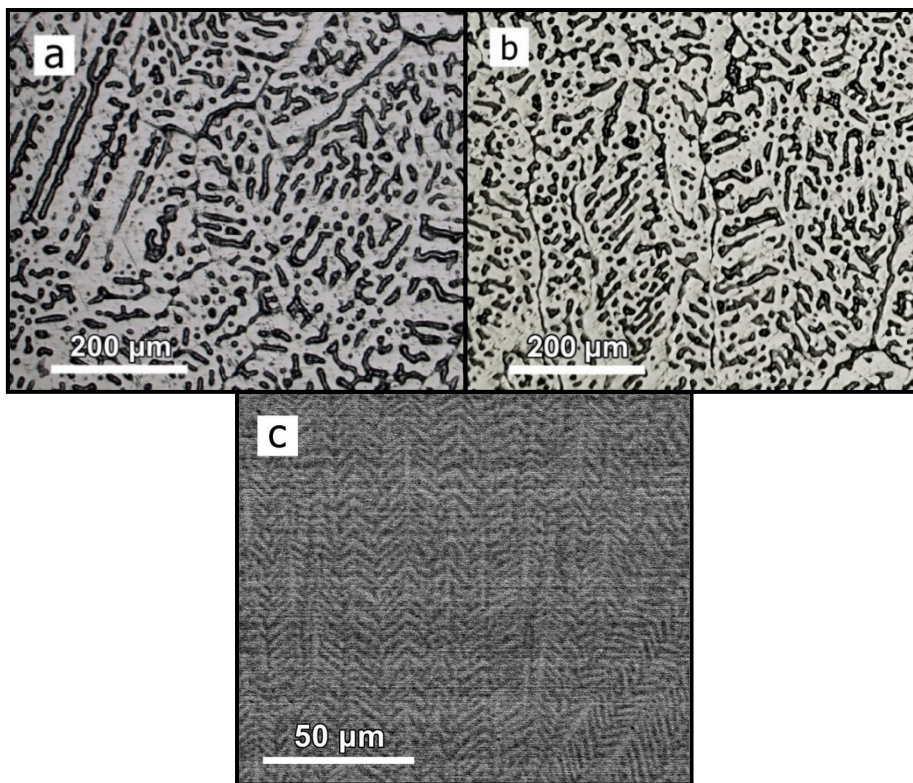
Figure 4.7 Optical images of etched a) BA b) OA, BS-SEM image of polished c) OA

The elemental compositions of BA and OA are taken from different regions with EDS analysis, including dendritic and interdendritic regions, as shown in Figure 4.7. The average results showed a good agreement with the designed stoichiometry (Table 4.5). As predicted by Scheil calculations, the elements with higher melting points (Nb and Ta) are primarily located in dendrites during the solidification, while lighter elements with lower melting points (Ti and Zr) are enriched in interdendritic regions. Moreover, elemental compositions of the dendritic and interdendritic regions of OA are further examined to investigate enrichment and depletion phenomena (Table 4.5). It should be noted that oxygen concentration is not provided due to the low accuracy of EDS analyses for lightweight elements.

Table 4.5 Comparison of compositions between planned and produced samples by EDS

		Ti	Zr	Nb	Hf	Ta
BA	Theoretical at%	25.0	35.0	20.0	5.0	15.0
	EDS at%	22.8±0.6	33.9±0.4	22.3±0.3	5.6±0.3	15.4±0.1
OA	Theoretical at%	25.0	35.0	20.0	5.0	15.0
	EDS at%	21.6±0.2	30.9±0.8	26.0±0.3	5.5±0.2	15.6±0.8
	Dendrite at%	21.1±0.5	28.8±1.1	26.6±0.3	6.2±1.6	17.1±0.4
	Interdendrite at%	25.2±0.6	34.1±1.3	22.4±0.2	5.4±0.5	12.3±1.2

X-ray diffraction experiments indicate that both alloys consist of a single BCC phase, as seen in Figure 4.8. It should be stated that this single-phase BCC is BCC#2 which is stable at high temperatures due to the fast cooling during vacuum arc melting. Single solid solution was expected from thermophysical parameters, and BCC structure was expected from the VEC value during the alloy design. VEC

value of the base alloy was 4.35, and oxygen doping slightly changed it to 4.38, which are both under BCC formation limit of 6.87. All peaks of both alloys are fitted into Gaussian function and it has been observed that the peaks of the oxygen-doped sample slightly shifted to lower diffraction angles, indicating a larger lattice parameter. This lattice expansion originates from the distortion caused by oxygen addition, as expected from the previous study[20]. The theoretical lattice parameters are calculated by the rule of mixture as 3.406 Å for BA and 3.408 Å for OA, similar to the results calculated from XRD peaks, which are also fitted into the Gaussian function. This, together with the lack of any additional superlattice reflections, indicates no ordering in the structure.
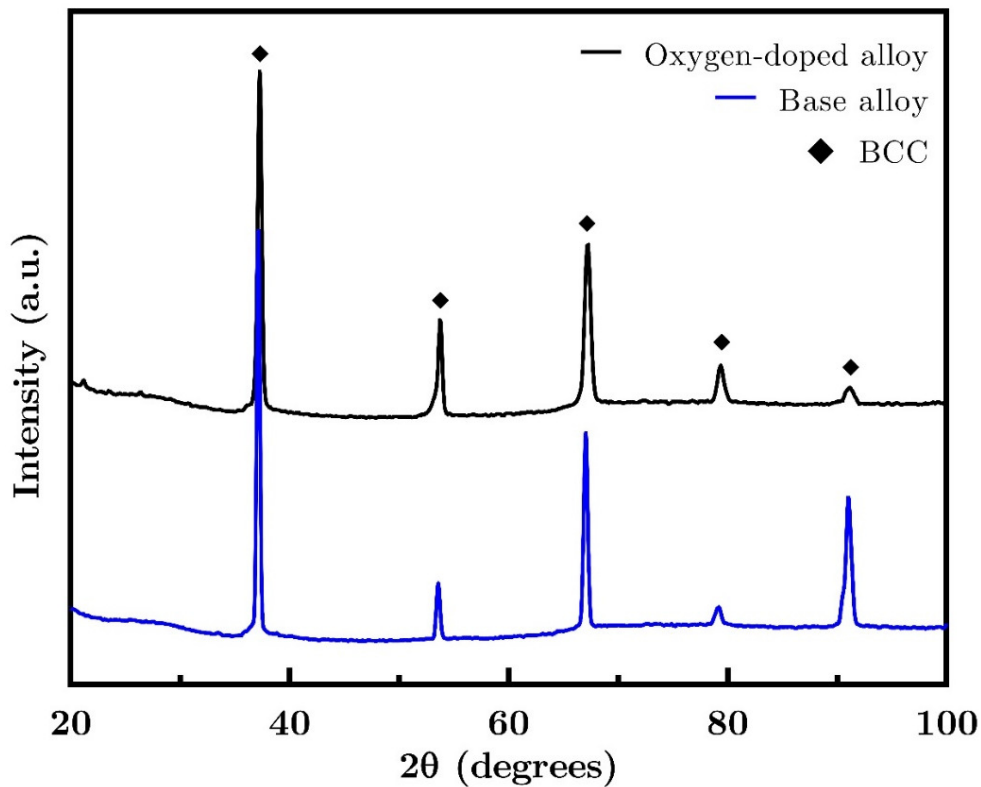
Figure 4.8. XRD diagrams of BA (blue) and OA (black)

Figure 4.9 shows a BFTEM in multibeam condition and a selected area electron diffraction (SAED) pattern along <111> zone axis of the oxygen-doped alloy in the as-cast state. BFTEM does not show the existence of any second phase. Besides, SAED confirms that the structure is a single BCC without any additional phases and showed an agreement with the XRD results. The absence of diffraction spots from an ordered structure, such as B2 (ordered BCC), proved that complete randomness is achieved.
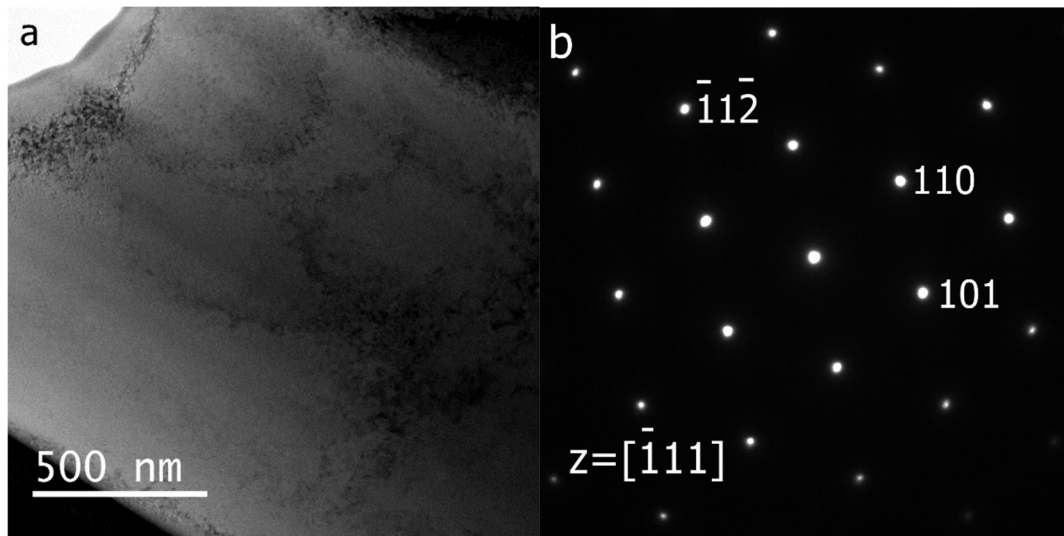
Figure 4.9. a) BFTEM image of oxygen-doped alloy b) SAED pattern along [111]

4.1.3 Mechanical Properties

Hardness values of the constituent elements are taken from[88], [89] and shown in Table 4.6. The theoretical hardness of the base alloy was calculated as 106 HV by using the rule of mixture (ROM). However, Vickers microhardness values of the base and oxygen-doped alloys are measured from ten random places as 321 HV and 440 HV for BA and OA, respectively. The results show an extensive improvement compared to elemental values, referencing the motivation behind

HEAs. The difference between BA and OA comes from the strength enhancement by the oxygen-doping effect.

Table 4.6 Mechanical properties of constituent elements and produced alloys

	Ti	Zr	Nb	Hf	Ta	ROM	BA	OA
Vickers Hardness (HV)	99	92	135	179	89	106	321±6	440±20
Yield Strength (MPa)	195	280	240	240	170	232	-	1240±50

Since oxygen doping has a considerable effect on hardness, further compression tests were conducted on 4 different OAs. Figure 4.10 shows one of the representative compression test results on oxygen doped alloy at room temperature. The yield strength is measured as 1240±50 MPa using the 0.2% offset method, as shown in Figure 4.10. The samples exhibited large ductility under compression as the specimens did not fracture until the test was stopped at 35% strain, exceeding 3000 MPa stress. It should be noted that there is a considerable improvement in yield strength compared to the calculated value of 232 MPa by the rule of mixture. When it is compared to elemental yield strength values from Table 4.6, rule of mixture (ROM) yield strength is multiplied by 5.3 when these elements form an oxygen-doped alloy. There is also a large improvement when the constituent element with the highest yield strength (Zr) and OA is compared, 280 MPa and 1240 MPa, respectively. In the same way, ROM hardness values are multiplied by 3 and 4.15 when the constituent elements form the base and oxygen-doped alloy, respectively.
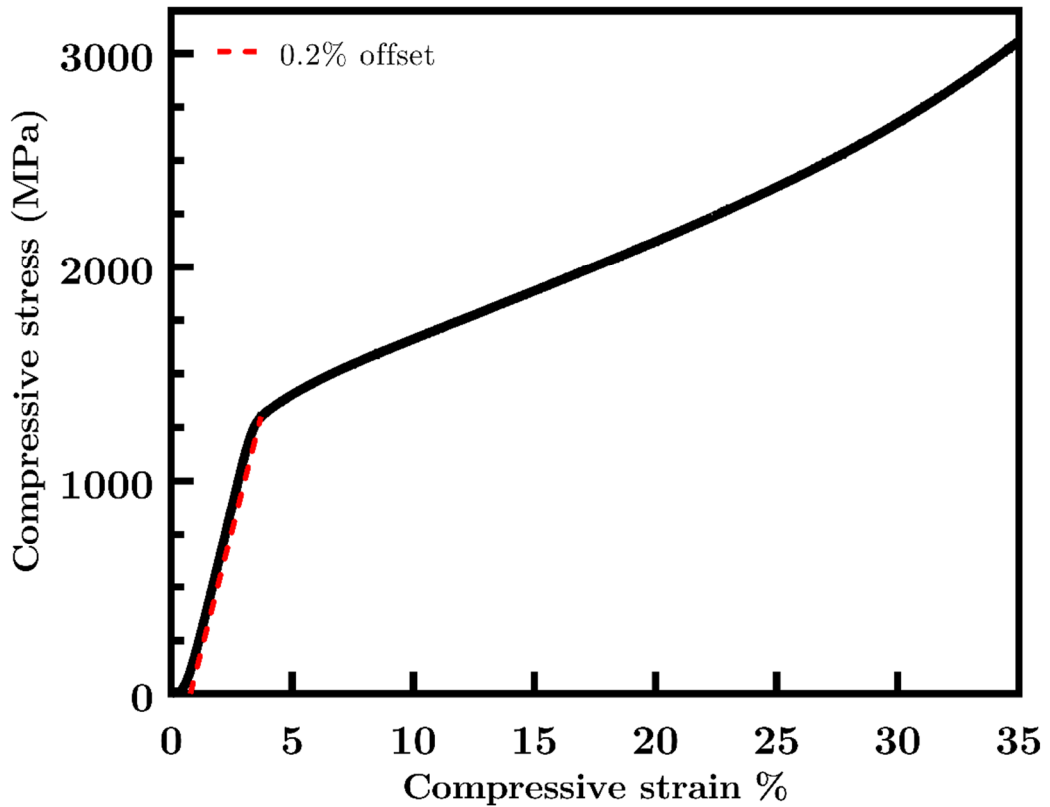
Figure 4.10. Compression test results of the oxygen-doped alloy

4.2 Discussion

4.2.1 Design Approach

Alloy design approaches of HEAs frequently use studies that focus on the estimation of the microstructure. In these studies, various models and parameters are proposed for the formation conditions of solid solution phase (SS) and intermetallic compounds (IC) [32]–[38]. These models are based on Hume-Rotary rules, which include geometrical and thermodynamical relations of the constituent elements.

67

One of the most accepted parameters for thermodynamical relations is the enthalpy of mixing (ΔH_{mix}). A significant negative value of ΔH_{mix} means attraction, which leads to short-range ordering (like IC) due to stronger bonds, while a large positive value means repulsion, which leads to phase segregation due to less miscibility. Considering this, in the present study, ΔH_{mix} is aimed to be kept around zero (like in ideal solutions) so that the distribution of atoms is in complete randomness. Similarly, various models agreed on the minimization of ΔH_{mix} through zero to obtain a HEA with SSS. However, they proposed different ΔH_{mix} ranges for the formation of SSS [32]–[34]. For the initial 126 different equiatomic compositions, ΔH_{mix} varies between -8 and 3 kJ/mol, which does not exceed any proposed solid solution formation limit. However, according to models that used ΔH_{mix} parameter, SS and IC formation ranges intersect [32]–[34]. For instance, Guo et al. proposed that ΔH_{mix} must be between -11.6 kJ/mol and 3.2 kJ/mol and $\delta < 6.6\%$ to form a single solid solution[34]. Also, in the same study, it is stated that an IC may form when $\delta > 4\%$, which overlaps with the single solid solution formation range. Therefore, it is not enough to satisfy the solid solution rule to eliminate the intermetallic phase (IC) for a HEA. Therefore, to eliminate the undesired IC phase, alloy design was adjusted within the given SS ranges and out of IC ranges in this study.

A more comprehensive approach is proposed by Yang et al., which adopts Ω parameter (Eq.2.3) as a function of ΔH_{mix}, ΔS_{mix} and T_m[35]. In this model, Gibbs free energy formula (Eq.2.4) is converted into Ω parameter, which needs to be maximized to stabilize a single disordered phase and suppress the formation of other phases. δ parameter is also considered in this model for topological agreement among the constituent elements. In this study, the solid solution formation range is determined as; $\Omega > 1.1$ and $\delta < 6.6\%$, which, again, intersects with IC range ($\Omega < 10$ or $\delta > 4\%$).

Since this study aims to improve structural stability and ductility, alloy design focuses on achieving the most stable single solid solution tendency and eliminating IC phases in all temperature ranges. Therefore, after determining the quinary element set (Ti-Zr-Nb-Hf-Ta) among 126 candidates, the composition was further optimized according to this approach. Instead of the proposed SS ranges of the above-stated models, new ranges for the thermophysical parameters were determined as $\Omega > 10$ and $\delta < 4\%$ to prevent the IC formation at any temperature.

4.2.2   Microstructure

The thermophysical approach used in this study has been shown to be a reliable tool to predict the formation of single-phase BCC for $Ti_{25}Zr_{35}Nb_{20}Hf_5Ta_{15}$ and $(Ti_{25}Zr_{35}Nb_{20}Hf_5Ta_{15})_{98}O_2$ RHEAs. The room temperature microstructure of the alloy consists of dendrites as expected since there is a difference in melting temperature of the constituent elements. Further heat treatments can tailor the microstructure. For instance, TiZrNbHfTa RHEA can be cold-worked and recrystallized to eliminate segregation and obtain coarse equiaxed grains[89]. However, in this study, only as-cast samples have been investigated to understand structural behaviors.

Atomic ordering must be checked for RHEAs, since the ordered BCC phase (known as B2 structure) causes embrittlement and cannot be detected by CALPHAD simulations. One of the methods is the comparison of the experimental and theoretical lattice parameters. The theoretical value of base alloy is calculated by the rule of mixture (Table 4.1), while the experimental lattice parameter is obtained from XRD data. Both experimental data and theoretical calculations result in similar lattice parameters, which infers the lack of ordering in the microstructure of BA[88], [90]. However, this method is not applicable for oxygen-doped alloy as the theoretical calculations do not consider the effect of doping on the lattice

parameter. Besides, XRD analyses for the base and oxygen-doped alloy have shown the absence of superlattice peaks, confirming the disordered structures. However, the presence of second phase particles with low amounts is hard to detect with the XRD technique. Therefore, further confirmation is achieved by the SAED diffractogram. Neither second phase formation nor additional superlattice peaks have been observed, indicating that the crystal structure of oxygen-doped alloy is completely disordered without any ordered phases to disturb mechanical properties.

The presence of oxygen cannot be calculated by EDS analysis due to low accuracy for lightweight elements. However, a slight change in the lattice parameter from 3.406 Å to 3.408 Å indicates lattice expansion due to doping of oxygen and increment is similar to the previous study of Lei et al. [20]. Additionally, the amount of oxygen is checked according to the Ti concentration in the system, which is introduced into the system with a certain pure Ti / TiO_2 ratio.

BS-SEM images of oxygen-doped alloy revealed the compositional contrast with dendritic morphology. Micro-segregation is common for HEAs since each constituent element has a different melting temperature. This causes heterogeneity in elemental distribution without the formation of a new phase[8]. EDS results showed that elements with higher melting points (Nb and Ta) are located in the dendrites, while interdendritic regions are rich in low melting temperature elements, Ti and Zr. Similarly, Scheil calculation predicted the presence of microsegregation (Figure 4.3b). Also, the calculated composition of the liquid phase during the non-equilibrium cooling indicated that starting from 1900 °C the liquid phase is depleted in Nb and Ta, pushing these into solidified dendrites and enriched with Ti and Zr. BS images and EDS results of oxygen doped-alloy match well with the non-equilibrium cooling simulations (Figure 4.3b and Figure 4.4), indicating that oxygen does not make any morphological and compositional change in the as-cast state.

4.2.3 Mechanical Properties

The total strength of the HEAs is dominated by solid solution strengthening since the modulus and lattice mismatches are higher compared to the conventional alloys. On the other hand, work hardening and grain boundary strengthening have a relatively weak effect [67], [89]. Consequently, the hardness measurement of the base alloy is three times higher than the calculated rule of mixture of the elemental hardness values (Table 4.6). High hardness values of the HEAs can be explained by severe lattice distortion, one of HEAs' core effects. Similarly, the considerable difference between elemental and base alloy values can be attributed to the cocktail effect, another core effect of HEAs. Due to large atomic size mismatch, lattices are always heavily distorted, which improves solid solution strengthening and causes much higher hardness values than the rule of mixture calculations. Lei et al. have shown that the strength increases by 40-45% with the addition of 2 at% oxygen into RHEAs [20], [31]. Similarly, in this study, the hardness value of base alloy increased from 312 HV to 440 HV with ~40% hardening after oxygen doping. Similarly, the same level of improvement is expected for compressive yield strength since Ti-Zr-Hf-Nb-Ta system HEAs show compressive yield strength between 840-929 MPa in equiatomic and non-equiatomic compositions in their as-cast state [8], [88], [91], [92].

When the rule of mixture (ROM) hardness value of constituent elements (106 HV) is compared to base and oxygen-doped alloy separately, it is multiplied by 3 and 4.2 for BA and OA respectively. This large improvement is demonstrated in Figure 4.11. Similar to the hardness values, the rule of mixture values of elemental yield strength (Table 4.6) is multiplied by 5.3 when these elements form an oxygen-doped HEA. The combination of oxygen improvement and cocktail effect resulted in high strength compared to elemental values.
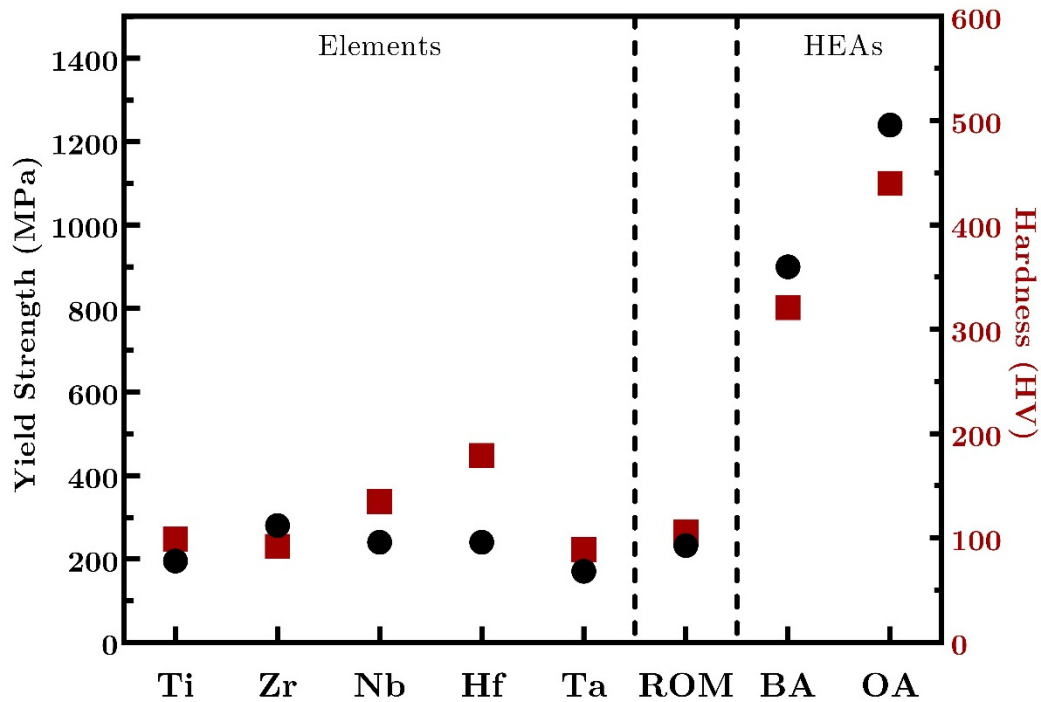
Figure 4.11. Mechanical property comparison between pure elements and designed HEAs

The most common problem with RHEAs for industrial applications is low ductility at room temperature, which originates from the brittle BCC phase of RHEAs. In this study, two different strategies have been used for the improvement of ductility. The first strategy utilizes the electron theory, which provides intrinsic ductility when applied to RHEAs[19]. Lowering VEC under 4.4 is reported to change the failure mode from screw dislocation glide to shear deformation[71]. Thus, alloy composition was determined considering this criterion. Another strategy is oxygen-doping. It has been recently shown that 2 at% oxygen addition results in a considerable improvement in strength and ductility simultaneously by creating complex oxygen clusters[20]. These clusters improve strength by pinning the dislocations and multiplying them while homogeneously distributing the passing dislocations. This way, necking is delayed, and ductility is improved. The combination of these two strategies with the absence of any brittle ordered phase

creates a ductile composition, which shows a fracture strain of more than 30% under compressive load. With a combination of high compressive strength and strain, oxygen-doped alloy has significant mechanical properties when it is compared to other RHEAs and conventional material groups in Figure 4.12.
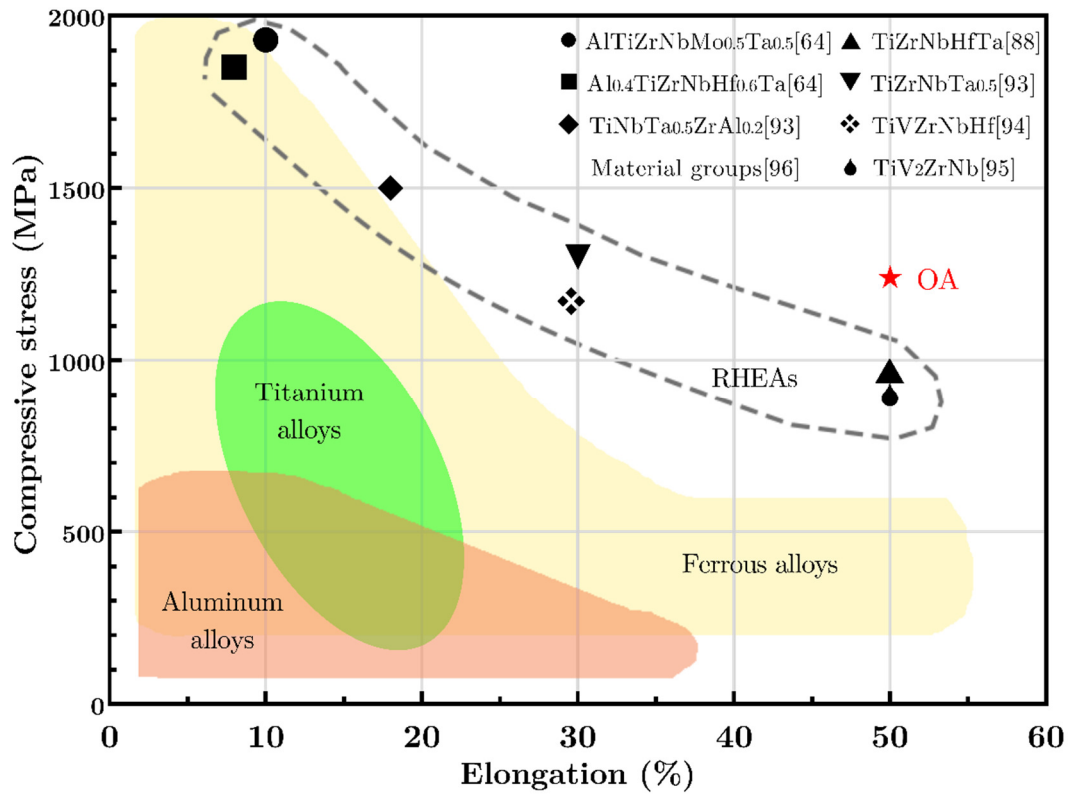
Figure 4.12. Comparison of compressive stress vs. strain values of the conventional material groups and other RHEA studies [64][88][93][94][95][96]

CHAPTER 5

HIGH TEMPERATURE CHARACTERIZATION

HEAs are considered as strong candidates for refractory applications due to their stability supporting core effects, sluggish kinetics and severe lattice distortion. Also, having heavy metals and increased entropy effect at elevated temperatures support the high structural stability. In this chapter, thermal characterization of the oxygen-doped alloy (OA) with $(Ti_{25}Zr_{35}Nb_{20}Hf_5Ta_{15})_{98}O_2$ composition will be investigated to reveal its thermal stability. Although oxygen-doped RHEAs show exceptional strength and ductility, there is no study for the thermal characterization of this material system[20], [31]. It is crucial to understand high-temperature behavior of the oxygen-doped RHEAs for the acceleration of the refractory applications. Even though base and oxygen-doped alloys contain a single BCC structure at room temperature as it has been designed. However, they might be in their metastable state and transform into a more stable structural state at higher temperatures. The appearance of the secondary phases can be advantageous or disadvantageous for the structural, thermal and mechanical properties. For instance, the coexistence of two BCC phases with close lattice parameters by morphological locking increases thermal stability[10] and mechanical properties like strength and ductility[64], while HCP precipitation decreases thermal stability due to weak HCP-BCC interface[97] or undesired intermetallic compounds (IC) decreases mechanical properties drastically[61][62]. Therefore, thermal characterization of the alloys is crucial for refractory applications.

In the previous chapter, base alloy (BA) and oxygen-doped alloy (OA) are designed, produced, and characterized in structural and mechanical manners with a well agreement between simulations and experiments. Since the effect of oxygen

cannot be considered in thermophysical calculations and CALPHAD simulations, the calculations are compatible only with base alloy. To understand high-temperature behavior of the oxygen-doped alloy, high-temperature tests are conducted on the oxygen-doped sample. The comparison of these test results is expected to reveal if oxygen creates any structural or thermal difference from base alloy or not. In this regard, another possible outcome of the thermal characterization tests is the investigation of the proper annealing routes. Therefore, in this chapter, only as-cast samples are experimentally characterized.

5.1 Results

DSC analyses on the oxygen-doped sample were performed to determine the phase transformations, as seen in Figure 5.1. DSC analyses were conducted in continuous heating mode and at different heating rates (10, 20, 40 °C/min) for resolution-sensitivity balance. The results display two exothermic peaks around 1000 °C and 1100 °C in all different heating rates. The critical temperature of the second peak does not change with the heating rate, which infers the existence of a second-order transformation[98]. Specific heat capacity (Cp) is measured as 301 J/kg.K at room temperature, similar to other measurements on HEAs[99], [100]. Mixing entropy is measured as 29.66 J/mol.K (3.57 R) from DSC tests and satisfied the HEA definition rule (ΔSmix > 1.61 R), while also correlating with CALPHAD entropy calculation in Figure 4.6. Further analyses were conducted using high-temperature XRD to understand appeared two reactions.
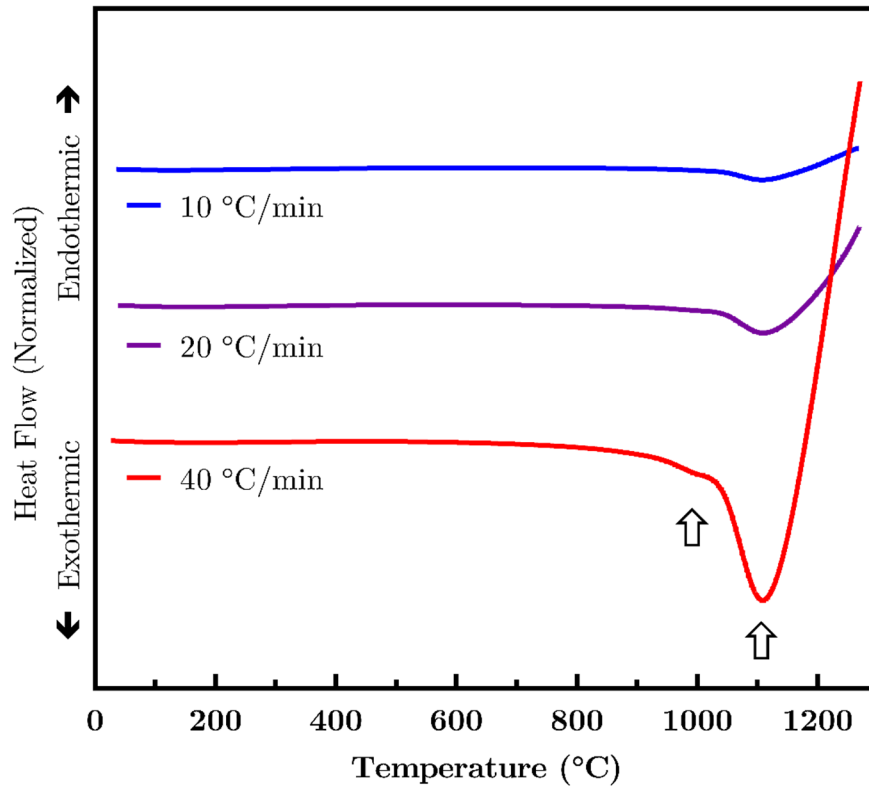
Figure 5.1. DSC results of the oxygen-doped alloy with different heating rates. Two exothermic peaks are indicated with arrows

High-temperature XRD results of the oxygen-doped alloy are shown in Figure 5.2a. Note that, for the homogenous distribution of heat, a thin specimen was used; therefore, XRD spectra contain the peaks of the Platinum holder (ICSD ID: 52250). Thus, Figure 5.2b is added for simplicity, which shows the strongest peaks between the diffraction angles of 34°-39°. It is known that the single-phase BCC structure is the primary phase at room temperature (see Figure 4.8 and Figure 5.2). There is no phase transformation between room temperature and 600 °C besides a slight sharpening of the peaks. At temperatures between 800 °C – 1000 °C, the strongest peak of room temperature BCC (labeled as BCC#2) existing between 37° - 38°, starts decomposing into two BCC phases, forming the room temperature BCC (labeled as BCC#1). This behavior has been observed on the property diagram of

77

the base alloy (see Figure 4.3a). This transformation also matches with the second DSC peak. The peaks of BCC#1 are located at lower diffraction angles, indicating a slightly higher lattice parameter than BCC#2 due to presence of elements with larger atomic radii (Nb and Ta). Starting from 1000 °C, BCC#1 disappears, and only BCC#2 is stable. At 1000 °C and 1100 °C, the diffractograms indicate a single BCC#2 phase, correlating with CALPHAD calculations. This correlation is expected to be continued by maintaining the single BCC phase up to melting temperature due to entropy-supported phase stability by elevated temperature.
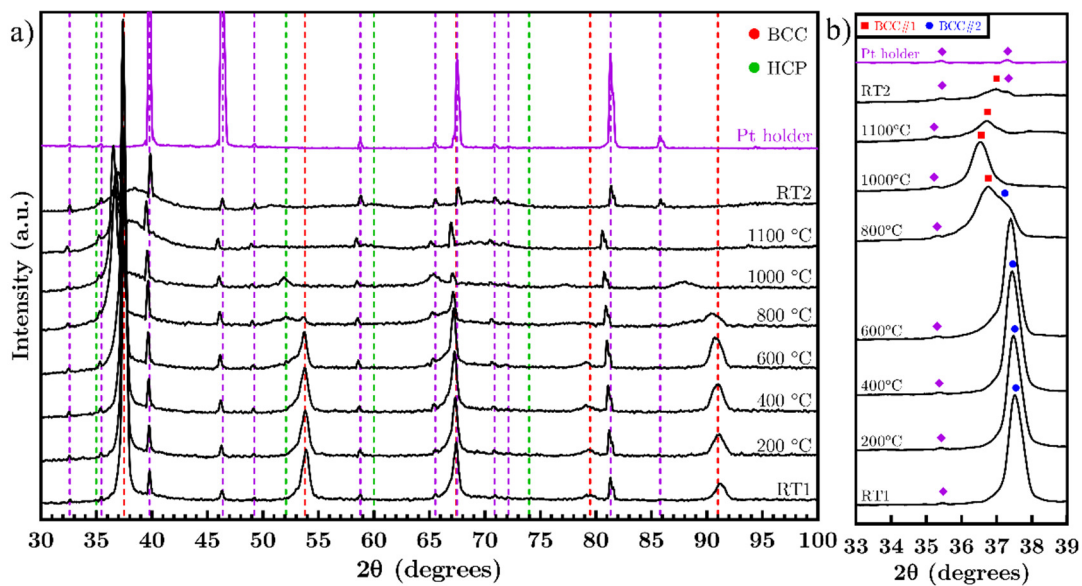
Figure 5.2. a) HT-XRD pattern of the OA between room temperature (RT1) - 1100 °C and cooled to room temperature (RT2) again b) Focus on the strongest peak between 34°-39°

Between 600 °C and 1000 °C, some of the HCP peaks appear and disappear, as shown in Figure 5.3, from the strongest peaks between 51°-53°. The transformation starts with the precipitation of the HCP phase in the main BCC#2 phase. At the temperatures above which the HCP phase is not stable, the transformation completes with the dissolution of the HCP phase into the BCC#2 phase. This transformation can be correlated with the first peak of the DSC test, which is verified as delayed HCP precipitation. It should be noted that the diffraction angles

78

decrease with increasing temperature, indicating the increasing lattice parameter by expansion at elevated temperatures.
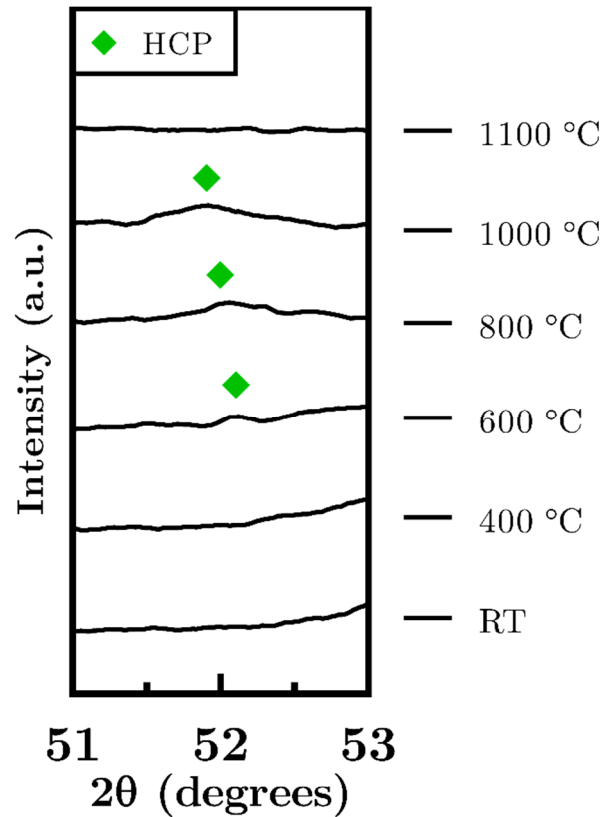
Figure 5.3. HT-XRD pattern of the oxygen-doped sample focused on the HCP peak between 51-53 degrees

For the further investigation of high-temperature behavior and phase transformations, in-situ TEM analysis is conducted, as shown in Figure 5.4. It can be seen that, between room temperature and 600 °C, there are not any changes and the oxygen-doped alloy protects its single BCC structure without any ordering. Starting from 600 °C, diffraction spots start to flatten, which becomes clearer at 900 °C. Moreover, at 900 °C, additional diffraction spots appear, which indicates formations of new phase(s). From the previous HT-XRD data, new phases are expected as new BCC#1 and HCP phases.
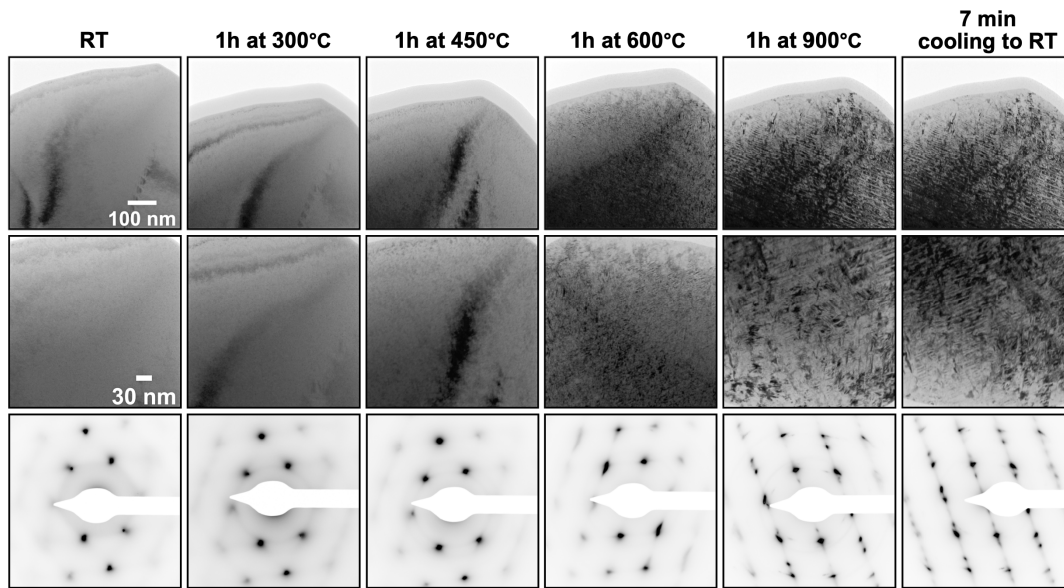
Figure 5.4. In-situ TEM images and SAED patterns of oxygen-doped alloy

To understand the new structures, the oxygen-doped alloy is air-cooled to room temperature from 900 °C. The present diffraction spots are investigated individually by dark-field TEM imaging, as shown in Figure 5.5a by color code. In addition to the main phase, BCC#2 (red), there are two new phases that appeared which are BCC#1 (yellow) and HCP (green and pink), as expected. The results showed that BCC#1 and HCP are formed in a lamellar morphology in region 1. To understand pink and blue diffraction spots, EDS mapping of regions 1 and 2 are conducted in Figure 5.5b and c, respectively. Only red and blue diffractions came from region 2, where EDS mapping is shown in Figure 5.5c. The elemental distribution is uniform in region 2, indicating that blue spots are the annealing twin of BCC#2. For region 1, BCC#1 is rich in Ti, Nb and Ta, while the HCP phase is rich in Zr and Hf, matching well with the CALPHAD calculations where BCC#1 is Ta and Nb rich with smaller amount of Ti and HCP rich in Zr and Ti with a smaller amount of Hf (Figure 4.5). It should also be stated that there are some Ti-Zr rich HCP precipitates formed as a result of 900 °C annealing, which is coherent with lamellar HCP phase in the diffraction diagram (Figure 5.5b).

80
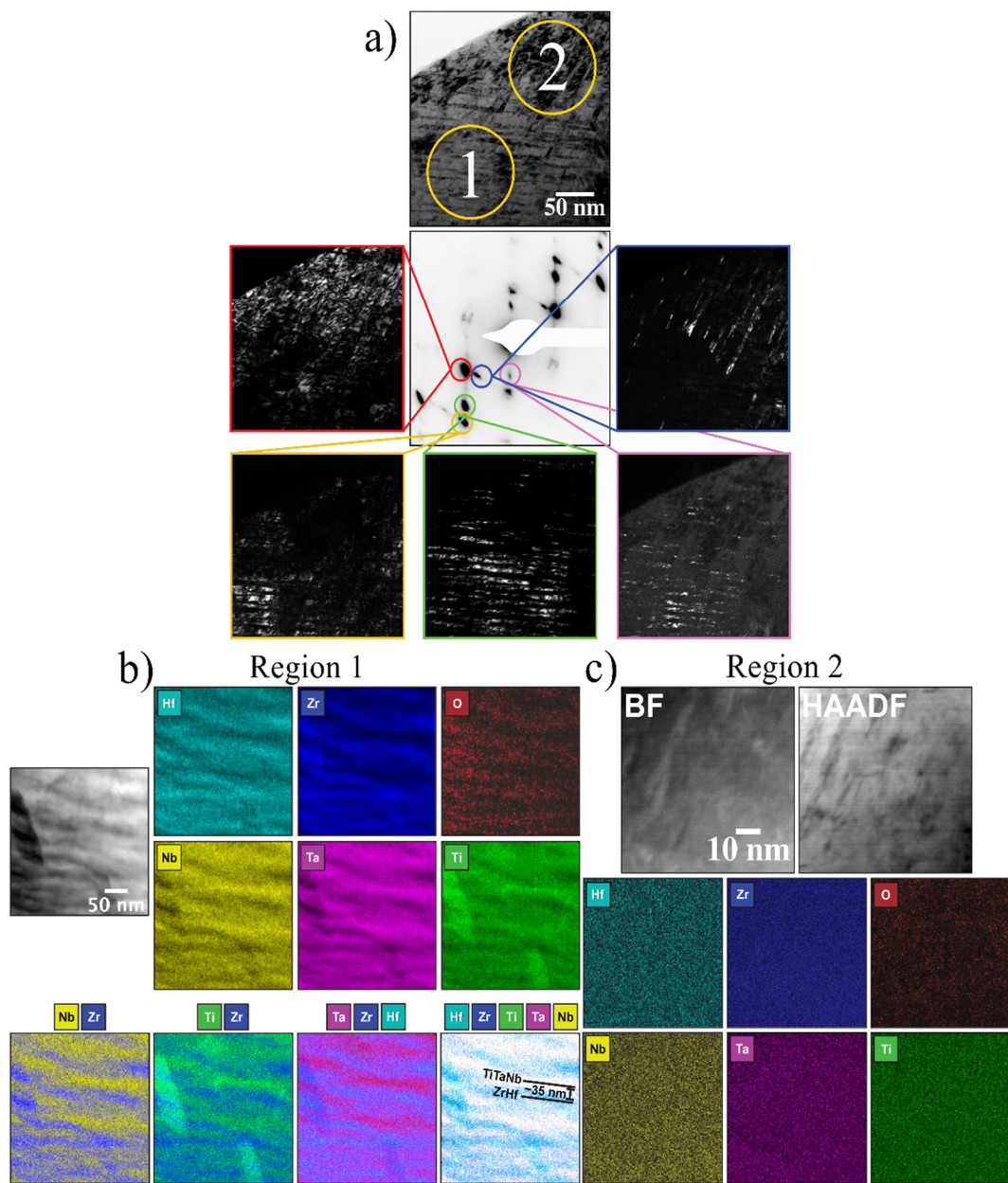
Figure 5.5. a) DF-TEM image of air-cooled oxygen-doped alloy from 900 °C. Elemental mapping of b) Region 1 c) Region 2

5.2   Discussion

RHEAs are considered strong candidates for refractory applications due to their high melting temperatures and structural stability as a result of sluggish kinetics and severe lattice distortion[44], [101]. Although oxygen-doped RHEAs show exceptional strength and ductility at room temperature, there is no study for the thermal characterization of this material system to investigate high-temperature behavior.

Experimental verification showed that base and oxygen-doped alloys contain a single BCC structure at room temperature as they are designed. However, thermochemical calculations on $Ti_{25}Zr_{35}Nb_{20}Hf_5Ta_{15}$ system have indicated the presence of other phases at room temperature. Thus, the structure might be at a metastable state and transform into a more stable structural state at higher temperatures. HT-XRD and HT-TEM analyses have shown no transformation between RT – 600 °C, except the slight sharpening of the peaks of XRD, which can be attributed to the elimination of strain by stress relief since the alloy is in an as-cast state. Between 600 °C and 1000 °C, HCP precipitation and BCC transformation can be observed in the means of two exothermic peaks as a result of the DSC test and proved by in-situ TEM later on. Generally, exothermic reactions during heating indicate the transformation of a metastable state into a more stable state which is obstructed during the cooling from the liquid[102].

According to CALPHAD calculations, the HCP phase is stable at lower temperatures. However, HT-XRD and HT-TEM results showed no HCP peaks below 600 °C, which indicates that the formation of the HCP phase is obstructed by sluggish kinetics of HEA at low temperatures. This kind of obstructed equilibrium phase can precipitate if a long time heat treatment is applied, which is sometimes the case after plastic deformation to create nucleation sites [58], [59],

[89]. Similarly, the long dwell times and slow cooling like furnace cooling during the HT-XRD and air cooling during the HT-TEM allowed HCP precipitation. DSC analysis also revealed the formation of HCP as an exothermic peak between 600 °C and 1000 °C due to stress relief in the system during precipitation.

There is a temperature trade-off to precipitate the HCP phase since it requires a high temperature to surpass the sluggish diffusion while it is stable at lower temperatures. The delayed precipitation temperature can be explained by considering the gradual and slow heat distribution inside the alloy. After the precipitation between 600 °C and 1000 °C depending on the annealing duration, HCP dissolves into the main BCC phase in HT-XRD. Pacheco et al. have shown that HCP phase (stable between 0-730 °C) precipitates after 48-hour annealing at 600 °C followed by water quenching or 1 hour at 1000 °C followed by slow cooling while it is obstructed when the treatment is performed for 1 hour at 600 °C and 1000 °C followed by water quenching[103]. In other words, the HCP phase precipitates at the as-cast state with increasing temperatures between 600 °C – 1000 °C, when sufficient time is provided by long treatment and/or slow cooling. The HCP phase is not stable at temperatures higher than 1000 °C and can be eliminated when the treatment is followed by fast cooling. For temperatures below 1000 °C, it is also possible to eliminate the formation of the HCP phase by short heat treatments or fast cooling.

The coexistence of two BCC phases at 800 °C in Figure 5.2 and at 900 °C in Figure 5.5 can be attributed to the slight difference in their Gibbs free energies[89]. This difference is predicted to be small since the two structure has similar compositions and similar lattice parameters. Additionally, since BCC#1 is compositionally rich in elements with larger atomic radii like Nb and Ta (it is composed of Ti, Ta and Nb), it has a slightly larger lattice parameter than BCC#2. During cooling after the complete solidification of BCC#2, no additional transformation occurs due to

sluggish kinetics of HEAs and BCC#2 becomes room temperature structure. BCC#1 was formed with heating treatment during HT-XRD; however, it dissolves back to main BCC#2 starting from 1000 °C since it is stable at lower temperatures. This coexistence is analyzed by fitting Gaussian equations in Figure 5.6, and their phase fractions are calculated as 83% BCC#1 and 17% BCC#2. Since room and elevated (>1000 °C) temperature structure is BCC#2, BCC#1 has been formed and dissolved again into main BCC#2 around 800 °C. To achieve a complete BCC transformation from BCC#2 to BCC#1, extensive durations (24-100 hours) are required at 800 °C due to sluggish kinetics of HEAs[25], [58], [105]. On the other hand, heating rates of DSC, HT-XRD and HT-TEM tests are kept as slow as possible and holding time at HT-XRD was 2 hours for each step to converge the stable state.
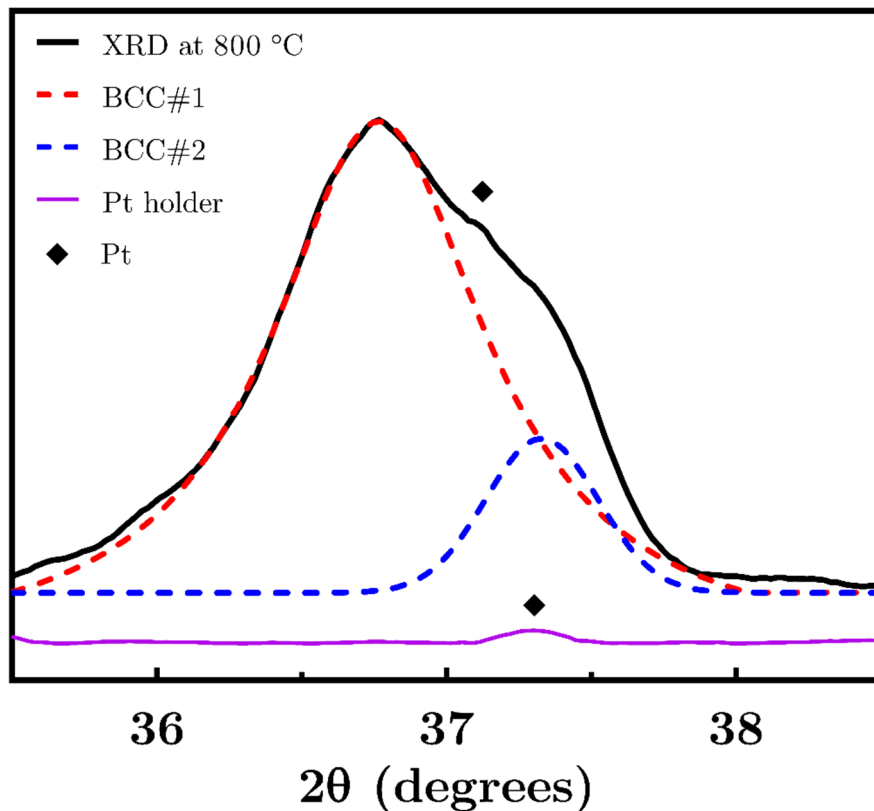
Figure 5.6. Deconvoluted XRD pattern of the strongest peak at 800 °C

As the non-equilibrium solidification model (Figure 4.3b) and BS-SEM images indicated, during the solidification between liquidus and solidus temperatures, elements with the highest melting points, Nb and Ta, solidify first into dendrites and are depleted from the liquid phase. The liquid phase is enriched in Ti and Zr before the complete solidification at solidus temperature. Consequently, BCC has a dendritic structure with Nb and Ta in dendritic cores, while Ti and Zr are present at interdendrites, as indicated by Scheil calculations. Therefore, the resulting BCC#2 phase has compositional fluctuations that cause various local lattice parameters, which can be seen from the wide distribution of the 1000 °C and 1100 °C peaks of the HT-XRD [82], [106]. Also, as the intensity is inversely related to the temperature, atomic vibrations decrease the signal/noise ratio, especially at elevated temperatures, causing a decrease in the intensity of all peaks[103]. Due to low intensity and sharpness, peaks are fitted better into the Gaussian function. Therefore, it has been reported that lattice parameter calculations cannot be reliable above 1000 °C[107]. Furthermore, the peaks of the holder and sample slightly shift towards the left with increasing temperature due to thermal expansion at high temperatures[43]. The peaks of the sample return to BCC#2 position after being quenched since it is the stable phase at room temperature (Figure 5.2).

In order to investigate the stability of $(Ti_{25}Zr_{35}Nb_{20}Hf_5Ta_{15})_{98}O_2$ system, ex-situ heat treatments were conducted at 800 °C and 1100 °C followed by furnace cooling with cooling durations of 8-10 hours and the phase content of these alloys is shown in Figure 5.7. 2-hour treatment at 800 °C results in dual BCC phases without HCP precipitation, indicating that precipitation cannot be activated at short-term treatments. However, 8-hour treatment at 800 °C induces HCP precipitation as sufficient annealing time is provided, including the furnace cooling duration. 2-hour and 8-hour treatments at 800 °C reveal that HCP precipitation requires a long treatment time, which is expected for HEA systems since their transformation kinetics are sluggish due to the complexity of the structure, containing five or more

elements. BCC transformation appears as a faster reaction since it probably has a spinodal decomposition mechanism, while HCP precipitation requires nucleation and growth kinetics[104], [108]. 8-hour and 24-hour treatments at 1100 °C indicate diffraction patterns with heavy HCP precipitation and a BCC phase. On the contrary, HT-XRD, together with CALPHAD calculations, exhibit a single BCC structure at 1100 °C for the base alloy. Even though the complete homogenization is achieved at the single BCC region at 1100 °C, an extended cooling duration resulted in the precipitation of the HCP phase. Therefore, it has been concluded that even though the oxygen-doped alloy consists of a single BCC phase at 1100 °C and above, HCP precipitation cannot be eliminated by furnace cooling, while a faster method would obstruct the formation of this phase.
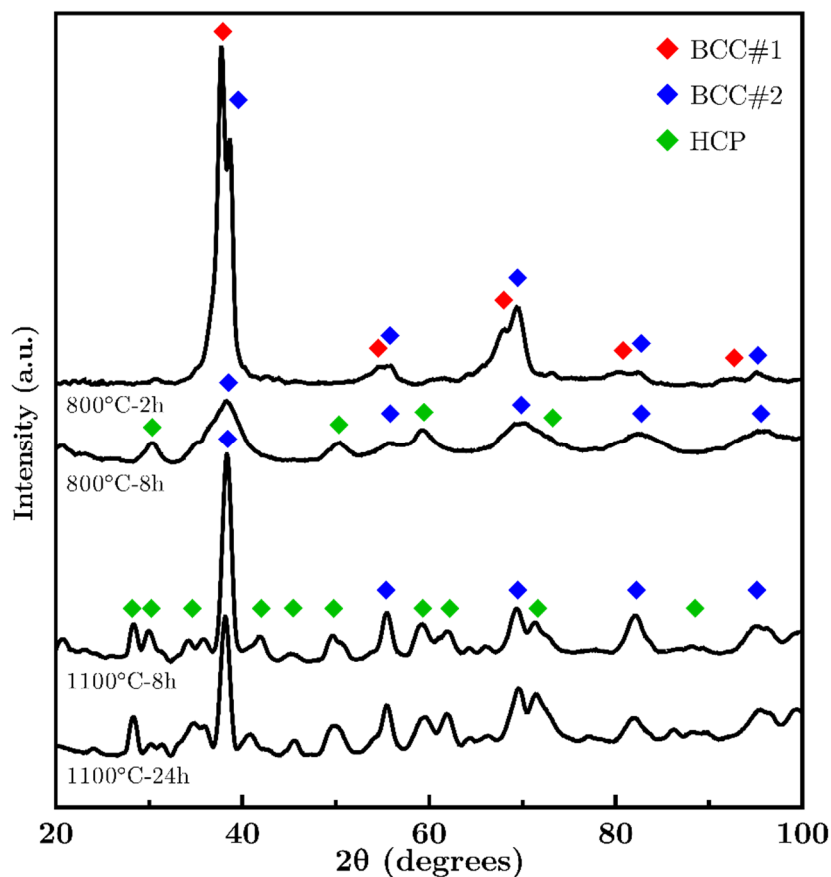
Figure 5.7. XRD diagrams of the OA after heat treatments at 800 °C and 1100 °C

Thermochemical calculations indicated that the $Ti_{25}Zr_{35}Nb_{20}Hf_5Ta_{15}$ system consists of stable single-phase BCC above ~980 °C. Since oxygen doping does not disturb the stability of the RT phase content, one can assume that $(Ti_{25}Zr_{35}Nb_{20}Hf_5Ta_{15})_{98}O_2$ RHEA has a single-phase region above 1000 °C, similar to the un-doped RHEA system. High configurational entropy is reasonable for high phase stability at elevated temperatures due to the high number of constituent elements. Also, it is supported by lattice distortion and low thermal diffusivity caused by contributed elements with high atomic weight and melting points like Hf and Ta. Since the metallic alloys generally exhibit a sudden drop of strength at 0.6 Tm, the melting points of the alloys are aimed to be higher than 1667 °C. During the alloy design stage, the elemental composition was tailored to maximize the theoretical melting point of the base alloy as 2117 °C. Besides, the CALPHAD calculations show that the final composition has a melting point of 1900 °C. Since the phase transformation temperatures for BA calculated by CALPHAD matches well with the experimentally determined phase transformations for OA, the melting temperature of OA is expected to be ~1900 °C.

CHAPTER 6

RADIATION PROPERTIES

RHEAs have high structural stability and sluggish kinetics, making them a candidate material for nuclear applications, which requires withstanding high dosage and temperature levels. Therefore, the effect of oxygen-doping on the radiation resistance of RHEAs is an important topic to be investigated. In this chapter, the structural stability of irradiated oxygen-doped RHEA will be investigated. Previously, the oxygen-doped alloy was designed and showed promising mechanical properties (high strength and ductility) and high-temperature stability without any drawbacks. It consists of a single BCC phase between room temperature and 600 °C without any ordered phase. In this study, the oxygen-doped alloy is irradiated with 3 dpa levels (3, 10 and 30 dpa) at room temperature and 450 °C. The resulting microstructures have been investigated with two-beam bright-field transmission electron microscopy (BF-TEM) and nano hardness techniques.

6.1   Results

Radiation experiments were conducted on oxygen-doped alloy due to its mechanical improvements and high-temperature stability. Before irradiation, experiments were simulated using Fe ions using SRIM software. The binding energies are taken as 40 eV for each metallic material. Dosage levels (ion/cm^2) are determined by the calculations from SRIM software according to expected dpa (displacement per atom): 3, 10 and 30 dpa as 4.3 x 10^{15}, 1.42 x 10^{16}, and 4.3 x 10^{16} ions/cm^2, respectively.

For the irradiation experiments, desired dpa levels will correspond to 0.75 microns of the sample so that 0.5 – 1 micron depth of the sample can be inspected. For example, for 30 dpa, the damage is shown in Figure 6.1 (the inspected region is shaded red), where the implanted Fe^{++} ion profile is superimposed. The irradiation temperatures are selected as room temperature (RT) and 450 °C, since 0.1Tm– 0.3Tm range is used for dislocation loop analysis.
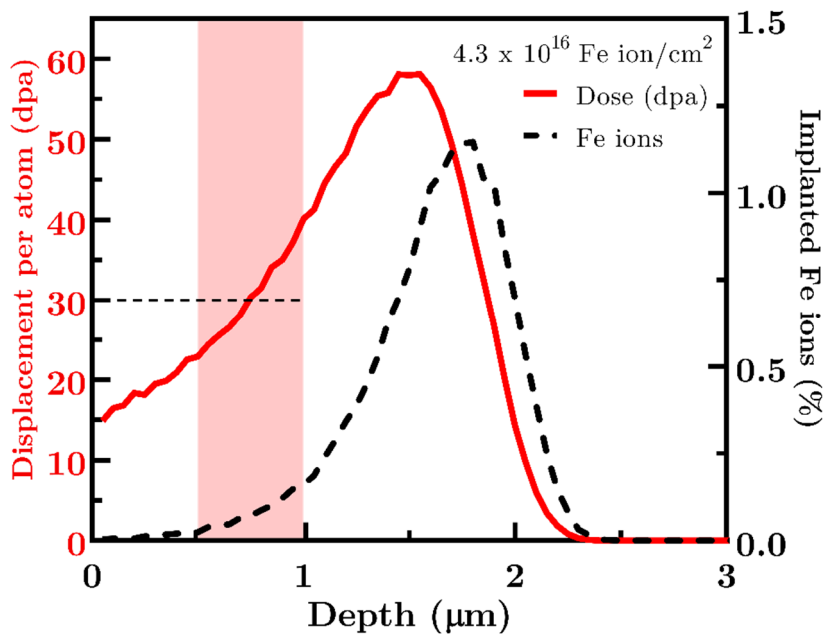
Figure 6.1. SRIM-simulated damage profile and distribution of implanted Fe ion into OA

Two-beam BF-TEM images of dislocation loops are shown for 6 conditions from the depth between 0.5 – 1 µm. Samples were tilted from [111] zone axis for 10 and 30 dpa and [100] zone axis for 3 dpa to g<011> two-beam condition. The dominant type of loops for the BCC metallic alloys are known as <100> and <111> types, so the dislocation loop analysis is focused on those two types of dislocations [109], [110]. The appearance and orientation of the dislocation loops are determined according to the criteria of Yao[110]. Three two-beam BF-TEM images from different regions for each condition have been investigated and dislocation loops are marked with either blue or red arrows depending on their types (Figure 6.2).

90
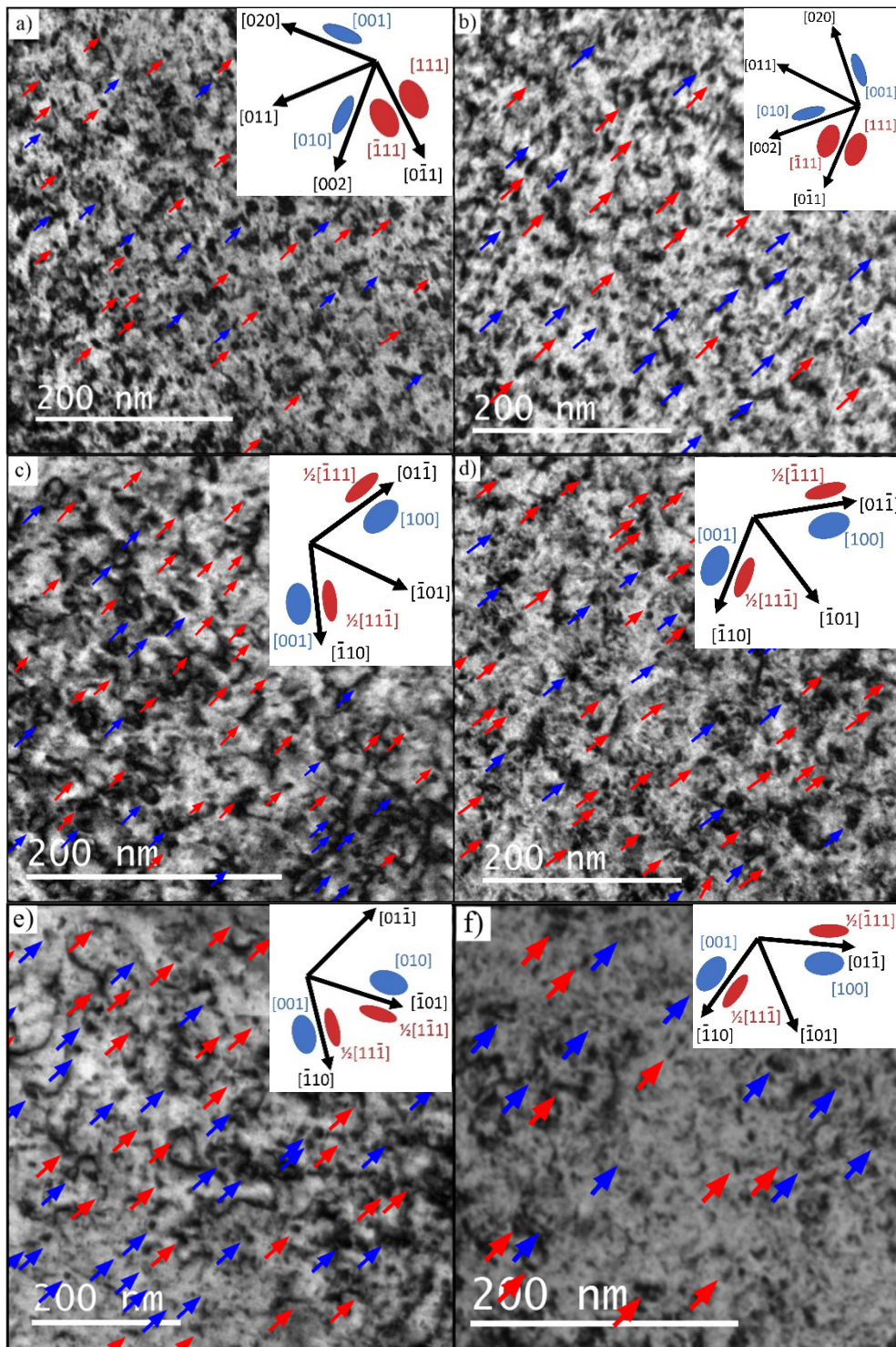
Figure 6.2. Two-beam BF-TEM images of oxygen-doped alloy, a) 3 dpa RT b) 3 dpa
450°C c) 10 dpa RT d) 10 dpa 450°C e) 30 dpa RT f) 30 dpa 450°C

The size of the marked <100> and <111> type dislocation loops were measured and their size distributions are presented in Figure 6.3. All the results are gathered in Figure 6.4 with averages and deviations.
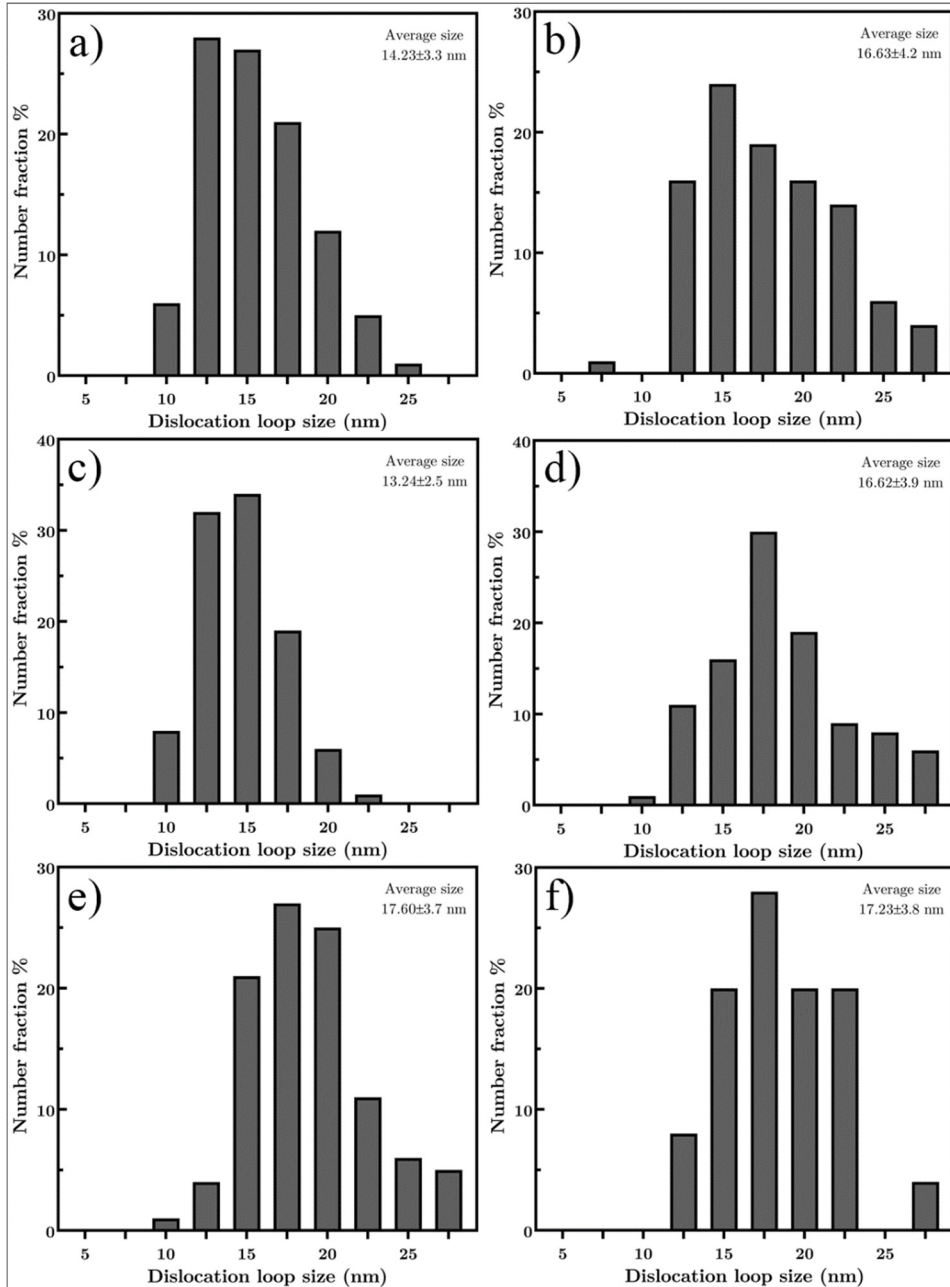
Figure 6.3. Dislocation loop size distributions in OA irradiated to a) 3 dpa at RT b) 3 dpa at 450°C c) 10 dpa at RT d) 10 dpa at 450°C e) 30 dpa at RT f) 30 dpa at 450°C.

From Figure 6.4, it is clear that the size of dislocation loops and black dots are increasing with increasing dpa and temperature. The smallest sizes are for 3 dpa-RT and 10 dpa-RT conditions; 14.23±3.3 nm and 13.24±2.5 nm, respectively. The sizes increase when the temperature is increased to 450 °C and became 16.63±4.2 nm and 16.62±3.9 nm for 3 and 10 dpa, respectively. The largest sizes are for 30 dpa conditions; 17.60±3.7 nm and 17.23±3.8 nm, for RT and 450 °C, respectively. It can be seen that dislocation loops sizes demonstrate a high deviation for all 6 conditions, since several regions are investigated. Marked a<100> and a<111> type dislocations are counted for 6 conditions at different maps and corrected with *g.b* invisibility criteria[110]. a<100> and <111> type dislocations are nearly equal to each other for all 6 conditions.
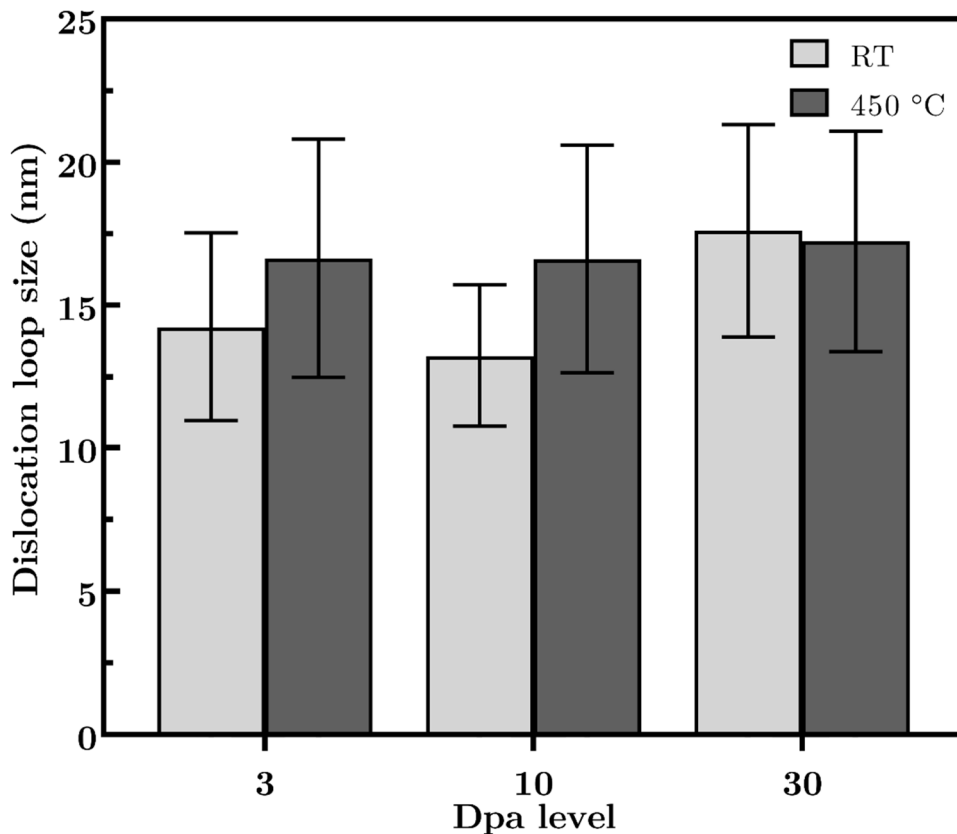
Figure 6.4. Dislocation loop sizes of irradiated oxygen-doped alloy

Total volume is calculated from the total area of the BF-TEM images, which are taken at 100 nm thickness. The number of dislocations is divided into total volume and dislocation number densities are calculated (Figure 6.5). Dislocation number densities increase with increasing dpa and temperature due to increased damage and defect-evolution kinetics. For room temperature conditions, the number of dislocation loops per m^3 increases as 2.96×10^{21}, 3.18×10^{21} and 3.29×10^{21} for 3, 10 and 30 dpa, respectively. For 450 °C irradiation conditions, number densities are 3.43×10^{21}, 3.38×10^{21} and 3.91×10^{21} for 3, 10 and 30 dpa. respectively. It reaches its highest value at 30 dpa-450 °C condition.
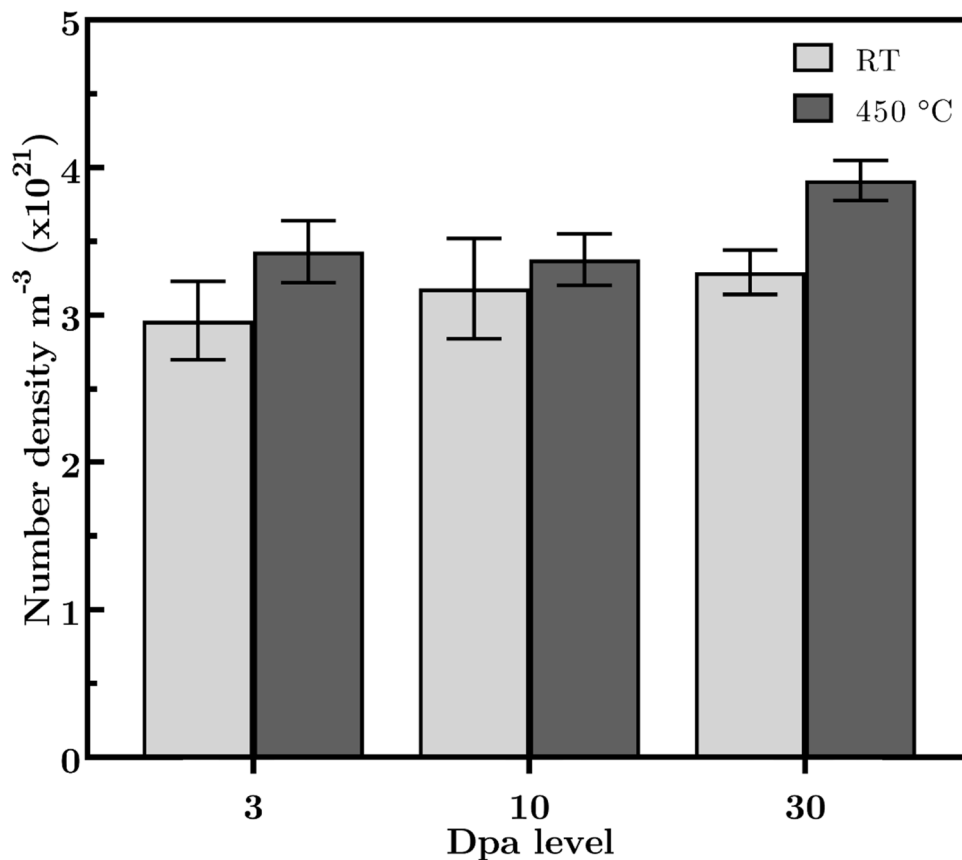
Figure 6.5. Dislocation number densities of irradiated oxygen-doped alloy
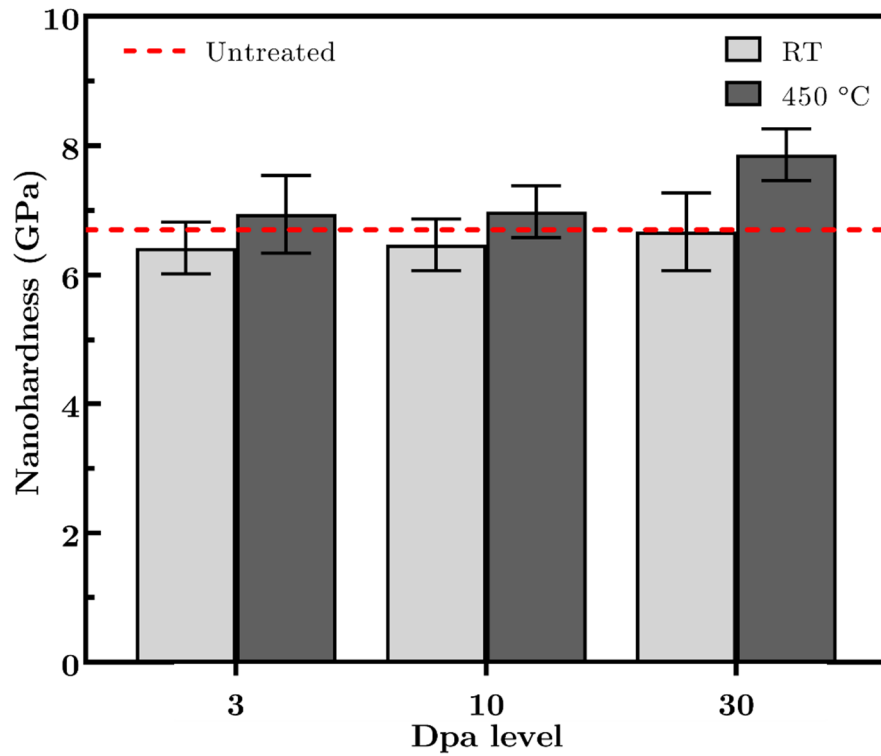
Figure 6.6. Nano hardness measurements of irradiated oxygen-doped alloy

Nanoindentation measurements were taken from the same irradiated regions, where dislocation loop analyses were conducted. The results are shown in Figure 6.6. Similar to dislocation number density, nano hardness measurements increase with increasing dpa and temperature. Nano hardness of untreated alloy is 6.75±0.5 GPa. For the irradiated samples, nano hardness values are revealed as 6.4±0.4, 6.5±0.4 and 6.7±0.6 GPa for 3, 10 and 30 dpa, respectively, for room temperature irradiations. For 450 °C, nano hardness values are 6.9±0.6, 7.0±0.4 and 7.9±0.4 GPa for 3, 10 and 30 dpa, respectively. The highest hardness value is measured at 30dpa-450 °C as 7.86±0.38 GPa, since it has the highest dpa and temperature.

Finally, no second phase particles, radiation-induced segregation and detectable voids are observed after radiation in all levels, indicating high structural stability for oxygen-doped alloy, $(Ti_{25}Zr_{35}Nb_{20}Hf_5Ta_{15})_{98}O_2$, even for high dosage and temperature levels.

6.2   Discussion

To examine irradiation damage, sample preparation damage must be excluded. To differentiate radiation damage and Ga damage from FIB sample preparation, different regions of the sample are investigated. An increasing trend of damage can be seen in Figure 6.7 and damages from irradiation and sample preparation are differentiated. Moreover, dislocation loops larger than 5 nm are considered for dislocation loop analysis. Since the small loops are excluded, the average dislocation loop size becomes larger.
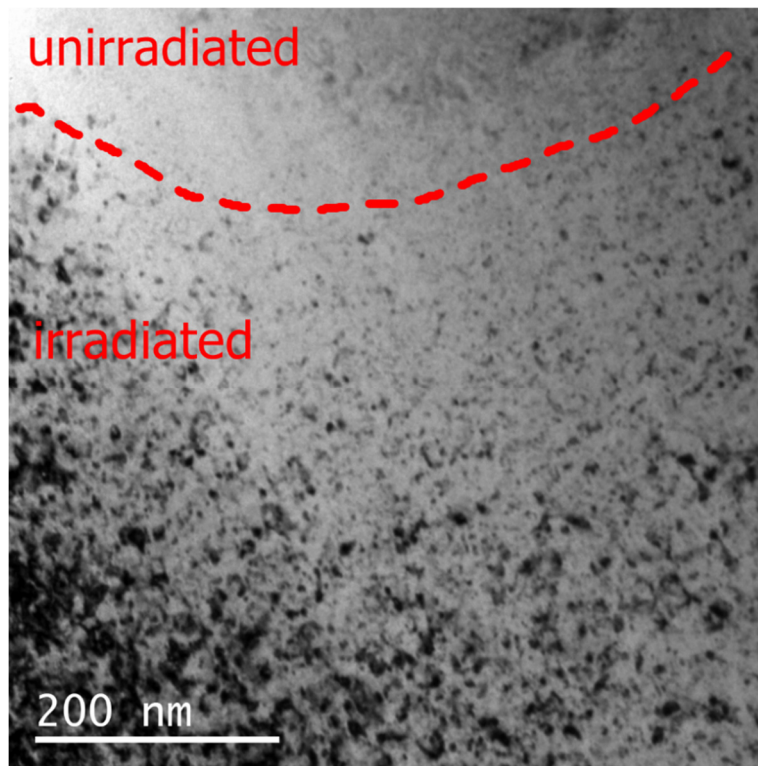
Figure 6.7. BF-TEM images of irradiated and unirradiated regions at 30 dpa-RT condition.

The distribution and concentration of the projected Fe^{++} ions are calculated in Figure 6.1. For the highest damage condition (30 dpa), Fe^{++} concentration reaches a maximum of 1.15 at%, which is a small addition and does not change the structure by varying thermophysical parameters like VEC.

Dislocation loop sizes follow an increasing trend with increasing dpa and temperature as expected. High damage increases the amount of lattice distortion, while temperature increases the kinetics, so that defects can grow[75]. However, there is a large deviation at the dislocation loop size distributions in Figure 6.3. The high variations on the dislocation loop sizes can be explained by local compositional differences. As it is discussed before, the lattice parameter shows a variation due to compositional fluctuations. Accumulation and depletion of different elements might create local compositional differences, even though it does not disturb the single BCC structure.

Deviations on the dislocation loop sizes lead to similar deviations on the nano hardness values since they are correlated with each other due to radiation-induced hardening[30]. These deviations might also be attributed to surface roughness and regional compositional fluctuations. Dislocation number density and correlating nano hardness values increase with increasing temperature, implying that temperature affects the defect evolution kinetics more dominantly than any heat treatment effect, like recovery. The drop of nano hardness for untreated alloy compared to irradiated alloys can be explained by the self-healing effect of HEAs, which is observed in previous studies on RHEAs[24], [73], [111], [112]. Self-healing is a unique phenomenon for HEAs, which consists of decreasing defect concentration due to local recovery by accumulated thermal energy on the distorted lattice of HEAs. Since dislocation loop density and nano hardness results are in agreement, the self-healing effect explains the drop of hardness after irradiation at low and moderate dosages, such as 3 and 10 dpa. Low or no hardening tendency of the oxygen-doped alloy is a promising feature for further nuclear applications, which requires long engineering life for plasma-facing components.

The oxygen doped alloy demonstrates a high radiation resistance since dislocation number density and nano hardness values slightly increased with increasing dosage

level. For instance, while the dpa level is multiplied by 10 (from 3 dpa to 30 dpa), dislocation number density and nano hardness increased only 11% and 4% for room temperature conditions. Also, nano hardness value drops for 3 and 10 dpa conditions due to self-healing effect, and there is a very small radiation-induced hardening for high dosage case, 30 dpa. There is also no phase transformation that occurred for all 6 conditions, indicating high structural stability for designed HEAs. To demonstrate, SAED pattern of the toughest irradiation condition (30 dpa) is shown in Figure 6.8, which can be compared to Figure 4.9b. To sum up, all effects indicate a strong radiation resistance for oxygen-doped RHEA.
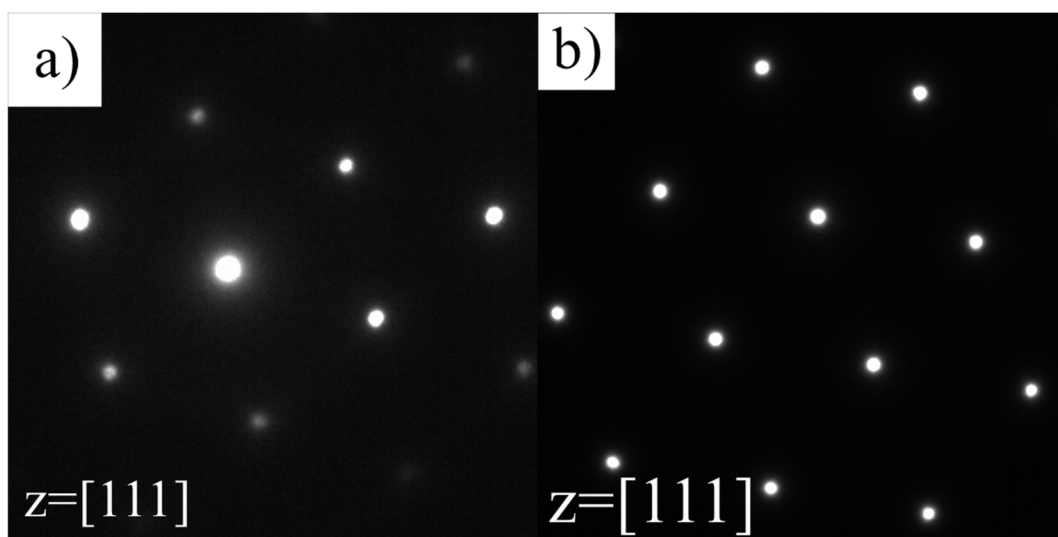
Figure 6.8. SAED patterns of OA, irradiated with 30 dpa at a) RT b) 450 °C

The radiation resistance of oxygen-doped RHEA, $(Ti_{25}Zr_{35}Nb_{20}Hf_5Ta_{15})_{98}O_2$, can be attributed to the chemical heterogeneity of HEAs, since it obstructs the dislocation loop growth. The RHEAs are already considered as radiation-resistant materials due to their sluggish kinetics and severely distorted lattices. Moreover, mixing entropy becomes more dominant at high temperatures and contributes to single-phase stability by decreasing the Gibbs free energy. Therefore, the high resistance of oxygen-doped alloy displayed a compatible material for nuclear applications, in addition to its mechanical properties and high-temperature stability.

CHAPTER 7

CONCLUDING REMARKS

In this study, two RHEAs are designed as oxygen undoped and doped conditions, with compositions of $Ti_{25}Zr_{35}Nb_{20}Hf_5Ta_{15}$ and $(Ti_{25}Zr_{35}Nb_{20}Hf_5Ta_{15})_{98}O_2$. For alloy design, seven thermophysical parameters ($\Delta Hmix$, $\Delta Smix$, Ω, δ, VEC, Tm and density) are optimized for maximum single solid solution tendency, which is required characteristic for sufficient mechanical properties and environmental resistance. Additionally, two ductility strategies, VEC theory and oxygen-doping, are considered in order to solve the common embrittlement problem of RHEAs to enable their use in structural applications. The designed compositions are produced by vacuum arc melting and XRD, SEM, and TEM techniques are performed for structural characterization. The alloys contain similar microstructures with a single BCC phase without any ordering in the as-cast state, as predicted by CALPHAD calculations. The microsegregation was predicted by CALPHAD calculations and verified with SEM BS-imaging and EDS results. It is revealed that 2 at% oxygen doping does not create any structural difference and disturbs the correlation with CALPHAD calculations for RHEAs. The hardness of the base and oxygen doped alloys was measured as 321 HV and 440 HV, respectively, indicating the mechanical improvement by oxygen-doping. The oxygen-doped alloy showed 1240±50 MPa compressive yield strength and high ductility. It is revealed that improved ductility of the oxygen-doped alloy was achieved by combining the alloy design strategies like oxygen effect, VEC theory and combination of multiple HEA formation models.

Furthermore, since it has been exhibited promising structural and mechanical properties, the high-temperature behavior of the oxygen-doped RHEA has been

investigated by in-situ and ex-situ XRD, DSC and TEM techniques. The oxygen-doped alloy maintained its single BCC phase up to 600 °C. Between 600 °C – 1000 °C, HCP transformation occurred while a single solid solution was observed above 1000 °C. At 1100 °C, HT-XRD results showed a single BCC, while ex-situ heat treatments revealed heavy HCP precipitation, inferring that it is possible to eliminate the precipitation by fast cooling. Most importantly, oxygen-doped RHEA does not contain any metallic oxide between 0 °C - 1100 °C. Therefore, it is revealed that in addition to improving strength and ductility simultaneously, oxygen-doping does not have any structural effect between RT - 1100 °C. From the alloy design stage, the aim of maximum single solid solution tendency was achieved since room and high-temperature structural characterization tests revealed high HEA tendency.

Finally, the irradiation response of oxygen-doped RHEA is investigated since it exhibited promising structural, mechanical, and high-temperature properties up to that point. Radiation experiments are simulated by SRIM software, and alloys are irradiated in 6 conditions accordingly and prepared for investigation by FIB. Two-beam condition BF-TEM images showed that dislocation loop sizes exhibit a wide deviation, attributed to the chemical heterogeneity of HEAs. Correlated results of dislocation loops density and nano hardness measurements showed reduced hardening for 3 and 10 dpa with respect to untreated state due to self-healing effect of HEAs. A small hardening is observed for the high 30 dpa case, which does not have any phase transformation, void formation, or structural changes similar to lower dpa levels. This structural stability is supported by low defect growth and hardening and eventually oxygen-doped alloy revealed as a promising candidate material for future nuclear applications with the addition of high structural resistance at elevated temperatures. Further studies on oxidation and big-scale production would accelerate the application of this system at refractory and nuclear applications.

REFERENCES

[1]   B. Cantor, I. T. H. Chang, P. Knight, and A. J. B. Vincent, "Microstructural development in equiatomic multicomponent alloys," *Mater. Sci. Eng. A*, vol. 375–377, no. 1-2 SPEC. ISS., pp. 213–218, 2004.

[2]   J.-W. Yeh *et al.*, "Formation of simple crystal structures in Cu-Co-Ni-Cr-Al-Fe-Ti-V alloys with multiprincipal metallic elements," *Metall. Mater. Trans. A*, vol. 35, no. 8, pp. 2533–2536, 2004.

[3]   C.-Y. Hsu, J.-W. Yeh, S.-K. Chen, and T.-T. Shun, "Wear Resistance and High-Temperature Compression Strength of Fcc CuCoNiCrAl0.5Fe Alloy with Boron Addition," *Metall. Mater. Trans. A, Phys. Metall. Mater. Sci.*, vol. 35, no. 5, pp. 1465–1469, 2004.

[4]   J. W. Yeh *et al.*, "Nanostructured high-entropy alloys with multiple principal elements: Novel alloy design concepts and outcomes," *Adv. Eng. Mater.*, vol. 6, no. 5, pp. 299-303+274, 2004.

[5]   J.-W. Yeh, "Recent Progress in High Entropy Alloy Research," *Sci. des Mater.*, vol. 31, no. 10, pp. 633–648, 2006.

[6]   R. Kozak, A. Sologubenko, and W. Steurer, "Single-phase heas - An overview," *Zeitschrift fur Krist.*, vol. 230, no. 1, pp. 55–68, 2015.

[7]   C. J. Tong *et al.*, "Mechanical performance of the AlxCoCrCuFeNi high-entropy alloy system with multiprincipal elements," *Metall. Mater. Trans. A Phys. Metall. Mater. Sci.*, vol. 36, no. 5, pp. 1263–1271, 2005.

[8]   Y. Yuan *et al.*, "Formation, structure and properties of biocompatible TiZrHfNbTa heas," *Mater. Res. Lett.*, vol. 7, no. 6, pp. 225–231, 2019.

[9]   L. Gao, W. Liao, H. Zhang, J. U. Surjadi, D. Sun, and Y. Lu,

"Microstructure, mechanical and corrosion behaviors of CoCrFeNiAl 0.3 High Entropy Alloy (HEA) films," *Coatings*, vol. 7, no. 10, pp. 1–7, 2017.

[10] V. Soni, O. N. Senkov, J. P. Couzinie, Y. Zheng, B. Gwalani, and R. Banerjee, "Phase stability and microstructure evolution in a ductile refractory hea Al10Nb15Ta5Ti30Zr40," *Materialia*, vol. 9, p. 100569, 2020.

[11] A. D. Pogrebnjak *et al.*, "Irradiation resistance, microstructure and mechanical properties of nanostructured (TiZrHfVNbTa)N coatings," *J. Alloys Compd.*, vol. 679, pp. 155–163, 2016.

[12] M. A. Hemphill *et al.*, "Fatigue behavior of Al 0.5CoCrCuFeNi high entropy alloys," *Acta Mater.*, vol. 60, no. 16, pp. 5723–5734, 2012.

[13] J. M. Wu, S. J. Lin, J. W. Yeh, S. K. Chen, Y. S. Huang, and H. C. Chen, "Adhesive wear behavior of AlxCoCrCuFeNi high-entropy alloys as a function of aluminum content," *Wear*, vol. 261, no. 5–6, pp. 513–519, 2006.

[14] O. N. Senkov, D. B. Miracle, K. J. Chaput, and J. P. Couzinie, "Development and exploration of refractory high entropy alloys - A review," *J. Mater. Res.*, vol. 33, no. 19, pp. 3092–3128, 2018.

[15] T. E. Whitfield *et al.*, "An assessment of the thermal stability of refractory high entropy superalloys," *J. Alloys Compd.*, 2020.

[16] O. N. Senkov, G. B. Wilks, D. B. Miracle, C. P. Chuang, and P. K. Liaw, "Refractory heas," *Intermetallics*, vol. 18, no. 9, pp. 1758–1765, 2010.

[17] O. N. Senkov, G. B. Wilks, J. M. Scott, and D. B. Miracle, "Mechanical properties of Nb 25Mo25Ta25W25 and V20Nb20Mo20Ta20W20 refractory high entropy alloys," *Intermetallics*, vol. 19, no. 5, pp. 698–706, 2011.

[18] O. N. Senkov, D. Isheim, D. N. Seidman, and A. L. Pilchak, "Development of a refractory hesa," *Entropy*, vol. 18, no. 3, pp. 1–13, 2016.

[19] S. Sheikh *et al.*, "Alloy design for intrinsically ductile refractory high-

entropy alloys," *J. Appl. Phys.*, vol. 120, no. 16, 2016.

[20] Z. Lei *et al.*, "Enhanced strength and ductility in a high-entropy alloy via ordered oxygen complexes," *Nature*, vol. 563, no. 7732, pp. 546–550, 2018.

[21] G. Dirras *et al.*, "Elastic and plastic properties of as-cast equimolar TiHfZrTaNb hea," *Mater. Sci. Eng. A*, vol. 654, pp. 30–38, 2016.

[22] Y. D. Wu *et al.*, "Refractory HfNbTiZr hea with excellent structural stability & tensile properties," *Mater. Lett.*, vol. 130, pp. 277–280, 2014.

[23] C. M. Barr *et al.*, "Exploring radiation induced segregation mechanisms at grain boundaries in equiatomic CoCrFeNiMn high entropy alloy under heavy ion irradiation," *Scr. Mater.*, vol. 156, pp. 80–84, 2018.

[24] A. Kareer, J. C. Waite, B. Li, A. Couet, D. E. J. Armstrong, and A. J. Wilkinson, "Short communication: 'Low activation, refractory, high entropy alloys for nuclear applications,'" *J. Nucl. Mater.*, vol. 526, pp. 0–5, 2019.

[25] N. A. P. K. Kumar, C. Li, K. J. Leonard, H. Bei, and S. J. Zinkle, "Microstructural stability and mechanical behavior of FeNiMnCr hea under ion irradiation," *Acta Mater.*, vol. 113, pp. 230–244, 2016.

[26] J. Duan, L. He, Z. Fu, A. Hoffman, K. Sridharan, and H. Wen, "Microstructure, strength and irradiation response of an ultra-fine grained FeNiCoCr multi-principal element alloy," *J. Alloys Compd.*, vol. 851, 2021.

[27] C. Lu *et al.*, "Radiation-induced segregation on defect clusters in single-phase concentrated SS alloys," *Acta Mater.*, vol. 127, pp. 98–107, 2017.

[28] T. Egami, W. Guo, P. D. Rack, and T. Nagase, "Irradiation resistance of multicomponent alloys," *Metall. Mater. Trans. A Phys. Metall. Mater. Sci.*, vol. 45, no. 1, pp. 180–183, 2014.

[29] S. Q. Xia, X. Yang, T. F. Yang, S. Liu, and Y. Zhang, "Irradiation Resistance in AlxCoCrFeNi HEAs," *Jom*, vol. 67, no. 10, pp. 2340–2344,

2015.

[30] S. qin Xia, Z. Wang, T. fei Yang, and Y. Zhang, "Irradiation Behavior in HEAs," *J. Iron Steel Res. Int.*, vol. 22, no. 10, pp. 879–884, 2015.

[31] Z. Lei *et al.*, "Snoek-type damping performance in strong and ductile high-entropy alloys," *Sci. Adv.*, vol. 6, no. 25, pp. 1–9, 2020.

[32] S. Guo and C. T. Liu, "Phase stability in high entropy alloys: Formation of solid-solution phase or amorphous phase," *Prog. Nat. Sci. Mater. Int.*, vol. 21, no. 6, pp. 433–446, 2011.

[33] Y. Zhang, Y. J. Zhou, J. P. Lin, G. L. Chen, and P. K. Liaw, "Solid-solution phase formation rules for multi-component alloys," *Adv. Eng. Mater.*, vol. 10, no. 6, pp. 534–538, 2008.

[34] S. Guo, Q. Hu, C. Ng, and C. T. Liu, "More than entropy in heas: Forming solid solutions or amorphous phase," *Intermetallics*, vol. 41, pp. 96–103, 2013.

[35] X. Yang and Y. Zhang, "Prediction of high-entropy stabilized solid-solution in multi-component alloys," *Mater. Chem. Phys.*, vol. 132, no. 2–3, pp. 233–238, 2012.

[36] Z. Wang, Y. Huang, Y. Yang, J. Wang, and C. T. Liu, "Atomic-size effect and solid solubility of multicomponent alloys," *Scr. Mater.*, vol. 94, pp. 28–31, 2015.

[37] A. K. Singh, N. Kumar, A. Dwivedi, and A. Subramaniam, "A geometrical parameter for the formation of disordered solid solutions in multi-component alloys," *Intermetallics*, vol. 53, pp. 112–119, 2014.

[38] Y. F. Ye, Q. Wang, J. Lu, C. T. Liu, and Y. Yang, "Design of heas: A single-parameter thermodynamic rule," *Scr. Mater.*, vol. 104, pp. 53–55, 2015.

[39] J. H. Li and M. H. Tsai, "Theories for predicting simple solid solution high-entropy alloys: Classification, accuracy, and important factors impacting accuracy," *Scr. Mater.*, vol. 188, pp. 80–87, 2020.

[40] B. Fultz, "Vibrational thermodynamics of materials," *Prog. Mater. Sci.*, vol. 55, no. 4, pp. 247–352, 2010.

[41] B. S. Murty, J. W. Yeh, and S. Ranganathan, *High-Entropy Alloys*. 2014.

[42] L. H. Wen, H. C. Kou, J. S. Li, H. Chang, X. Y. Xue, and L. Zhou, "Effect of aging temperature on microstructure and properties of AlCoCrCuFeNi high-entropy alloy," *Intermetallics*, vol. 17, no. 4, pp. 266–269, 2009.

[43] C. L. Lu, S. Y. Lu, J. W. Yeh, and W. K. Hsu, "Thermal expansion and enhanced heat transfer in heas," *J. Appl. Crystallogr.*, vol. 46, no. 3, pp. 736–739, 2013.

[44] E. J. Pickering and N. G. Jones, "High-entropy alloys: a critical assessment of their founding principles and future prospects," *Int. Mater. Rev.*, vol. 61, no. 3, pp. 183–202, 2016.

[45] K. Y. Tsai, M. H. Tsai, and J. W. Yeh, "Sluggish diffusion in Co-Cr-Fe-Mn-Ni high-entropy alloys," *Acta Mater.*, vol. 61, no. 13, pp. 4887–4897, 2013.

[46] Y. Zhang, X. Yang, and P. K. Liaw, "Alloy design and properties optimization of high-entropy alloys," *Jom*, vol. 64, no. 7, pp. 830–838, 2012.

[47] S. Noh, B. K. Choi, S. H. Kang, and T. K. Kim, "Influence of mechanical alloying atmospheres on the microstructures and mechanical properties of 15Cr ods steels," *Nucl. Eng. Technol.*, vol. 46, no. 6, pp. 857–862, 2014.

[48] C. Wang, W. Ji, and Z. Fu, "Mechanical alloying and spark plasma sintering of CoCrFeNiMnAl high-entropy alloy," *Adv. Powder Technol.*, vol. 25, no. 4, pp. 1334–1338, 2014.

[49] J. Málek *et al.*, "The effect of processing route on properties of HfNbTaTiZr

high entropy alloy," *Materials (Basel).*, vol. 12, no. 23, pp. 1–15, 2019.

[50] S. Zameer Abbas, F. Ahmad Khalid, and H. Zaigham, "Indentation and deformation behavior of FeCo-based bulk metallic glass alloys," *Mater. Sci. Eng. A*, vol. 654, pp. 426–435, 2016.

[51] S. Singh, N. Wanderka, B. S. Murty, U. Glatzel, and J. Banhart, "Decomposition in multi-component AlCoCrCuFeNi high-entropy alloy," *Acta Mater.*, vol. 59, no. 1, pp. 182–190, 2011.

[52] K. H. Cheng, C. H. Lai, S. J. Lin, and J. W. Yeh, "Structural and mechanical properties of multi-element (AlCrMoTaTiZr)Nx coatings by reactive magnetron sputtering," *ThinSolidFilms*, vol. 519, no. 10, pp. 3185–90, 2011.

[53] H. Dobbelstein, E. L. Gurevich, E. P. George, A. Ostendorf, and G. Laplanche, "Laser metal deposition of compositionally graded TiZrNbTa refractory high-entropy alloys using elemental powder blends," *Addit. Manuf.*, vol. 25, no. July 2018, pp. 252–262, 2019.

[54] H. Zhang, Y. He, and Y. Pan, "Enhanced hardness and fracture toughness of the laser-solidified FeCoNiCrCuTiMoAlSiB0.5 high-entropy alloy by martensite strengthening," *Scr. Mater.*, vol. 69, no. 4, pp. 342–345, 2013.

[55] S. Guo, C. Ng, J. Lu, and C. T. Liu, "Effect of valence electron concentration on stability of fcc or bcc phase in high entropy alloys," *J. Appl. Phys.*, vol. 109, no. 10, 2011.

[56] C. C. Juan *et al.*, "Enhanced mechanical properties of HfMoTaTiZr and HfMoNbTaTiZr refractory heas," *Intermetallics*, vol. 62, pp. 76–83, 2015.

[57] X. Yang, Y. Zhang, and P. K. Liaw, "Microstructure & compressive properties of NbTiVTaAlx HEAs," *Procedia Eng.*, vol. 36, pp. 292–298, 2012.

[58] N. D. Stepanov, N. Y. Yurchenko, S. V. Zherebtsov, M. A. Tikhonovsky,

and G. A. Salishchev, "Aging behavior of the HfNbTaTiZr high entropy alloy," *Mater. Lett.*, vol. 211, pp. 87–90, 2018.

[59]   Y. Ma *et al.*, "Hexagonal closed-packed precipitation enhancement in a NBTIHFZR refractory HEA," *Metals (Basel).*, vol. 9, no. 5, 2019.

[60]   C. J. Tong *et al.*, "Microstructure characterization of AlxCoCrCuFeNi high-entropy alloy system with multiprincipal elements," *Metall. Mater. Trans. A Phys. Metall. Mater. Sci.*, vol. 36, no. 4, pp. 881–893, 2005.

[61]   O. N. Senkov, S. V. Senkova, C. Woodward, and D. B. Miracle, "Low-density, refractory multi-principal element alloys of the Cr-Nb-Ti-V-Zr system: Microstructure and phase analysis," *Acta Mater.*, vol. 61, no. 5, pp. 1545–1557, 2013.

[62]   O. N. Senkov and C. F. Woodward, "Microstructure and properties of a refractory NbCrMo0.5Ta0.5TiZr alloy," *Mater. Sci. Eng. A*, vol. 529, no. 1, pp. 311–320, 2011.

[63]   B. Zhang, M. C. Gao, Y. Zhang, and S. M. Guo, "Senary refractory high-entropy alloy CrxMoNbTaVW," *Calphad Comput. Coupling Phase Diagrams Thermochem.*, vol. 51, pp. 193–201, 2015.

[64]   O. N. Senkov, S. V. Senkova, and C. Woodward, "Effect of aluminum on the microstructure and properties of two refractory high-entropy alloys," *Acta Mater.*, vol. 68, pp. 214–228, 2014.

[65]   B. Kang, J. Lee, H. J. Ryu, and S. H. Hong, "Ultra-high strength WNbMoTaV HEAs with fine grain structure fabricated by powder metallurgical process," *Mater. Sci. Eng. A*, vol. 712, no. Sep17, pp. 616–624, 2018.

[66]   E. P. George, W. A. Curtin, and C. C. Tasan, "High entropy alloys: A focused review of mechanical properties and deformation mechanisms,"

Acta Mater., vol. 188, pp. 435–474, 2020.

[67]   F. Otto, A. Dlouhý, C. Somsen, H. Bei, G. Eggeler, and E. P. George, "The influences of temperature and microstructure on the tensile properties of a CoCrFeMnNi HEA," *Acta Mater.*, vol. 61, no. 15, pp. 5743–5755, 2013.

[68]   B. Gludovatz, A. Hohenwarter, D. Catoor, E. H. Chang, E. P. George, and R. O. Ritchie, "A fracture-resistant high-entropy alloy for cryogenic applications," *Science (80-.).*, vol. 345, no. 6201, pp. 1153–1158, 2014.

[69]   N. D. Stepanov, N. Y. Yurchenko, E. S. Panina, M. A. Tikhonovsky, and S. V. Zherebtsov, "Precipitation-strengthened refractory Al0.5CrNbTi2V0.5 HEA," *Mater. Lett.*, vol. 188, no. September 2016, pp. 162–164, 2017.

[70]   L. Lilensten *et al.*, "Study of a bcc multi-principal element alloy: Tensile and simple shear properties and underlying deformation mechanisms," *Acta Mater.*, vol. 142, pp. 131–141, 2018.

[71]   L. Qi and D. C. Chrzan, "Tuning ideal tensile strengths and intrinsic ductility of bcc refractory alloys," *Phys. Rev. Lett.*, vol. 112, no. 11, pp. 1–5, 2014.

[72]   F. Romanelli, "Fusion Electricity A roadmap to the realisation of fusion energy 28 European countries signed an agreement to work on an energy source for the future," *Fusion Electr. - EFDA*, pp. 1–75, 2012.

[73]   D. Patel, M. D. Richardson, B. Jim, S. Akhmadaliev, R. Goodall, and A. S. Gandy, "Radiation damage tolerance of a novel metastable refractory hea V2.5Cr1.2WMoCo0.04," *J. Nucl. Mater.*, vol. 531, p. 152005, 2020.

[74]   D. J. Bacon, F. Gao, and Y. N. Osetsky, "Primary damage state in fcc, bcc and hcp metals as seen in molecular dynamics simulations," *J. Nucl. Mater.*, vol. 276, no. 1, pp. 1–12, 2000.

[75]   G. S. Was, *Fundamentals of Radiation Materials Science*. 2007.

[76] C. Parkin *et al.*, "In situ microstructural evolution in face-centered and body-centered cubic complex concentrated solid-solution alloys under heavy ion irradiation," *Acta Mater.*, vol. 198, pp. 85–99, 2020.

[77] S. J. Zinkle, "Fusion materials science: Overview of challenges and recent progress," *Phys. Plasmas*, vol. 12, no. 5, pp. 1–8, 2005.

[78] "HEA Calculator software v.0.1-alpha. http://doi.org/10.5281/zenodo.3590319 (accessed 20 Dec 2019)." .

[79] N. Zhou, S. Jiang, T. Huang, M. Qin, T. Hu, and J. Luo, "Single-phase high-entropy intermetallic compounds (HEICs): bridging high-entropy alloys and ceramics," *Sci. Bull.*, vol. 64, no. 12, pp. 856–864, 2019.

[80] O. N. Senkov, C. Zhang, A. L. Pilchak, E. J. Payton, C. Woodward, and F. Zhang, "CALPHAD-aided development of quaternary multi-principal element refractory alloys based on NbTiZr," *J. Alloys Compd.*, vol. 783, pp. 729–742, 2019.

[81] H. W. Yao *et al.*, "NbTaV-(Ti,W) refractory HEAs: Experiments and modeling," *Mater. Sci. Eng. A*, vol. 674, pp. 203–211, 2016.

[82] R. Sonkusare *et al.*, "Phase equilibria in equiatomic CoCuFeMnNi high entropy alloy," *Mater. Chem. Phys.*, vol. 210, pp. 269–278, 2018.

[83] "Thermo-Calc Software, TCHEA2: TCS High Entropy Alloy Database v2.1. http://www.thermocalc.com/media/35873/tchea2_extended_info.pdf (accessed 28 Jan 2020)."

[84] R. E. Stoller, M. B. Toloczko, G. S. Was, A. G. Certain, S. Dwaraknath, and F. A. Garner, "On the use of SRIM for computing radiation damage exposure," *Nucl. Instruments Methods Phys. Res. Sect. B Beam Interact. with Mater. Atoms*, vol. 310, pp. 75–80, 2013.

[85] O. N. Senkov, S. V. Senkova, and C. Woodward, "Effect of aluminum on

the microstructure and properties of two refractory high-entropy alloys," *Acta Mater.*, vol. 68, pp. 214–228, 2014.

[86] F. Boer, R. Boom, W. Mattens, A. Miedema, and A. Niessen, "Cohesion in Metals : Transition Metal Alloys," *North-Holland, Amsterdam*, 1989.

[87] E. Scheil, "Bemerkungen zur schichtkristallbildung," *Int. J. Mater. Res.*, vol. 34, no. 3, pp. 70–72, 1942.

[88] O. N. Senkov, J. M. Scott, S. V. Senkova, D. B. Miracle, and C. F. Woodward, "Microstructure & room temperature properties of TaNbHfZrTi HEA," *J. Alloys Compd.*, vol. 509, no. 20, pp. 6043–6048, 2011.

[89] O. N. Senkov and S. L. Semiatin, "Microstructure and properties of a rhea after cold working," *J. Alloys Compd.*, vol. 649, pp. 1110–1123, 2015.

[90] H. W. Yao, J. W. Qiao, J. A. Hawk, H. F. Zhou, M. W. Chen, and M. C. Gao, "Mechanical properties of refractory high-entropy alloys: Experiments and modeling," *J. Alloys Compd.*, vol. 696, pp. 1139–1150, 2017.

[91] M. Feuerbacher, M. Heidelmann, and C. Thomas, "Plastic deformation of ZrNbTiTaHf heas," *Philos. Mag.*, vol. 95, no. 11, pp. 1221–1232, 2015.

[92] G. Dirras *et al.*, "Microstructural investigation of plastically deformed Ti20Zr20Hf20Nb20Ta20 high entropy alloy by XRD and transmission electron microscopy," *Mater. Charact.*, vol. 108, pp. 1–7, 2015.

[93] Y. Cao, Y. Liu, B. Liu, and W. Zhang, "Precipitation behavior during hot deformation of powder metallurgy Ti-Nb-Ta-Zr-Al high entropy alloys," *Intermetallics*, vol. 100, no. March, pp. 95–103, 2018.

[94] E. Fazakas *et al.*, "Experimental and theoretical study of Ti20Zr20Hf 20Nb20X20 (X = V or Cr) refractory high-entropy alloys," *Int. J. Refract. Met. Hard Mater.*, vol. 47, pp. 131–138, 2014.

[95] O. N. Senkov, S. V. Senkova, D. B. Miracle, and C. Woodward,

"Mechanical properties of low-density, refractory MPEAs of the Cr-Nb-Ti-V-Zr system," *Mater. Sci. Eng. A*, vol. 565, pp. 51–62, 2013.

[96] D. Cebon, M. F. Ashby, C. Bream, and L. Lee-Shothaman, "CES EduPack software," *Granta Des. Limited, Cambridge, UK*, 2009.

[97] B. Schuh *et al.*, "Thermodynamic instability of a nanocrystalline, single-phase TiZrNbHfTa alloy and its impact on the mechanical properties," *Acta Mater.*, vol. 142, pp. 201–212, 2018.

[98] S. Laube *et al.*, "Controlling crystallographic ordering in Mo–Cr–Ti–Al HEAs to enhance ductility," *J. Alloys Compd.*, vol. 823, p. 153805, 2020.

[99] Y. Brif, M. Thomas, and I. Todd, "The use of high-entropy alloys in additive manufacturing," *Scr. Mater.*, vol. 99, pp. 93–96, 2015.

[100] J. Wang, J. Li, Q. Wang, J. Wang, Z. Wang, and C. T. Liu, "The incredible excess entropy in heas," *Scr. Mater.*, vol. 168, pp. 19–22, 2019.

[101] C. Lee *et al.*, "Lattice distortion in a strong and ductile refractory high-entropy alloy," *Acta Mater.*, vol. 160, pp. 158–172, 2018.

[102] R. Wang *et al.*, "Novel metastable engineering in single-phase high-entropy alloy," *Mater. Des.*, vol. 162, pp. 256–262, 2019.

[103] V. Pacheco *et al.*, "Thermal Stability of the HfNbTiVZr High-Entropy Alloy," *Inorg. Chem.*, vol. 58, no. 1, pp. 811–820, 2019.

[104] C. R. M. Afonso, P. L. Ferrandini, A. J. Ramirez, and R. Caram, "High resolution transmission electron microscopy study of the hardening mechanism through phase separation in a β-Ti-35Nb-7Zr-5Ta alloy for implant applications," *Acta Biomater.*, vol. 6, no. 4, pp. 1625–1629, 2010.

[105] J. Y. He *et al.*, "Precipitation behavior and its effects on tensile properties of FeCoNiCr high-entropy alloys," *Intermetallics*, vol. 79, pp. 41–52, 2016.

[106] M. Zhang, X. Zhou, X. Yu, and J. Li, "Synthesis and characterization of refractory TiZrNbWMo high-entropy alloy coating by laser cladding," *Surf. Coatings Technol.*, vol. 311, pp. 321–329, 2017.

[107] S. Alvi, O. A. Waseem, and F. Akhtar, "High Temperature Performance of Spark Plasma Sintered W0.5(TaTiVCr)0.5 Alloy," *Metals (Basel).*, vol. 10, no. 11, p. 1512, 2020.

[108] V. Soni, O. N. Senkov, J. P. Couzinie, Y. Zheng, B. Gwalani, and R. Banerjee, "Phase stability and microstructure evolution in a ductile refractory hea Al10Nb15Ta5Ti30Zr40," *Materialia*, vol. 9, no. December 2019, p. 100569, 2020.

[109] J. Chen, P. Jung, W. Hoffelner, and H. Ullmaier, "Dislocation loops and bubbles in oxide dispersion strengthened ferritic steel after helium implantation under stress," *Acta Mater.*, vol. 56, no. 2, pp. 250–258, 2008.

[110] B. Yao, D. J. Edwards, and R. J. Kurtz, "TEM characterization of dislocation loops in irradiated bcc Fe-based steels," *J. Nucl. Mater.*, vol. 434, no. 1–3, pp. 402–410, 2013.

[111] S. Chang, K. K. Tseng, T. Y. Yang, D. S. Chao, J. W. Yeh, and J. H. Liang, "Irradiation-induced swelling and hardening in HfNbTaTiZr refractory high-entropy alloy," *Mater. Lett.*, vol. 272, p. 127832, 2020.

[112] Y. Lu *et al.*, "A promising new class of irradiation tolerant materials: Ti2ZrHfV0.5Mo0.2 HEA," *J. Mater. Sci. Technol.*, vol. 35, no. 3, pp. 369–373, 2019.

A. Alloy Selection Calculations

During alloy design section, all the possible 126 combinations of the 9 refractory elements are calculated in quaternary compositions. Valence electron concentration (VEC), melting point (Tm), density, atomic size difference (δ), mixing enthalpy (ΔH_{mix}) and omega parameter (Ω) are calculated and highlighted in red or green in order to applied criterion. Finally, the compositions that obey single solid solution criterion (ones with all highlighted green) are ticked.

#	1	2	3	4	5	VEC	Tm K	Density (g/cm³)	δ	ΔH_{mix}	Ω	SS?
1	Ti	V	Cr	Zr	Nb	4,8	2236	6,57	7,40	-4,60	6,51	
2	Ti	V	Cr	Zr	Mo	5,0	2266	6,91	7,49	-5,72	5,30	
3	Ti	V	Cr	Zr	Hf	4,6	2188	7,52	9,70	-6,08	4,81	
4	Ti	V	Cr	Zr	Ta	4,8	2344	8,18	7,52	-4,82	6,51	
5	Ti	V	Cr	Zr	W	5,0	2425	8,70	7,41	-6,56	4,95	
6	Ti	V	Cr	Nb	Mo	5,2	2390	7,32	4,75	-4,13	7,75	√
7	Ti	V	Cr	Nb	Hf	4,8	2312	7,93	8,92	-3,91	7,91	
8	Ti	V	Cr	Nb	Ta	5,0	2469	8,60	5,44	-3,74	8,85	√
9	Ti	V	Cr	Nb	W	5,2	2550	9,12	4,76	-4,93	6,93	√
10	Ti	V	Cr	Mo	Hf	5,0	2341	8,27	9,13	-4,67	6,71	
11	Ti	V	Cr	Mo	Ta	5,2	2498	8,94	5,23	-4,03	8,29	√
12	Ti	V	Cr	Mo	W	5,4	2579	9,46	4,23	-3,16	10,93	√
13	Ti	V	Cr	Hf	Ta	4,8	2420	9,54	8,96	-4,09	7,91	
14	Ti	V	Cr	Hf	W	5,0	2501	10,06	9,03	-5,44	6,16	
15	Ti	V	Cr	Ta	W	5,2	2658	10,73	5,21	-4,80	7,41	
16	Ti	V	Zr	Nb	Mo	4,8	2380	7,20	6,06	-2,49	12,78	√
17	Ti	V	Zr	Nb	Hf	4,4	2302	7,80	7,66	0,18	170,4	
18	Ti	V	Zr	Nb	Ta	4,6	2458	8,47	5,63	0,43	77,32	√
19	Ti	V	Zr	Nb	W	4,8	2539	8,99	5,87	-3,85	8,82	√
20	Ti	V	Zr	Mo	Hf	4,6	2331	8,14	8,32	-3,38	9,24	
21	Ti	V	Zr	Mo	Ta	4,8	2488	8,81	6,13	-2,67	12,46	√

22	Ti	V	Zr	Mo	W	5,0	2569	9,33	6,19	-4,88	7,04	√
23	Ti	V	Zr	Hf	Ta	4,4	2410	9,42	7,50	-0,28	117,2	
24	Ti	V	Zr	Hf	W	4,6	2491	9,94	8,09	-4,71	7,08	
25	Ti	V	Zr	Ta	W	4,8	2647	10,61	5,92	-4,00	8,87	
26	Ti	V	Nb	Mo	Hf	4,8	2455	8,56	7,68	-1,89	17,39	
27	Ti	V	Nb	Mo	Ta	5,0	2612	9,22	3,93	-2,27	15,38	√
28	Ti	V	Nb	Mo	W	5,2	2693	9,74	3,37	-3,94	9,14	√
29	Ti	V	Nb	Hf	Ta	4,6	2534	9,83	7,13	0,71	47,86	
30	Ti	V	Nb	Hf	W	4,8	2615	10,35	7,49	-3,18	11,00	
31	Ti	V	Nb	Ta	W	5,0	2772	11,02	3,76	-3,56	10,42	
32	Ti	V	Mo	Hf	Ta	4,8	2563	10,17	7,67	-2,03	16,94	
33	Ti	V	Mo	Hf	W	5,0	2644	10,69	7,89	-3,85	9,19	
34	Ti	V	Mo	Ta	W	5,2	2801	11,36	3,83	-3,77	9,95	
35	Ti	V	Hf	Ta	W	4,8	2723	11,97	7,47	-3,28	11,10	
36	Ti	Cr	Zr	Nb	Mo	5,0	2379	7,40	6,85	-5,62	5,66	
37	Ti	Cr	Zr	Nb	Hf	4,6	2301	8,01	8,51	-4,13	7,46	
38	Ti	Cr	Zr	Nb	Ta	4,8	2458	8,68	6,56	-3,67	8,96	√
39	Ti	Cr	Zr	Nb	W	5,0	2539	9,20	6,70	-6,76	5,03	
40	Ti	Cr	Zr	Mo	Hf	4,8	2330	8,35	9,07	-6,64	4,70	
41	Ti	Cr	Zr	Mo	Ta	5,0	2487	9,02	6,94	-5,73	5,81	
42	Ti	Cr	Zr	Mo	W	5,2	2568	9,54	6,93	-6,75	5,09	
43	Ti	Cr	Zr	Hf	Ta	4,6	2409	9,62	8,38	-4,51	7,15	
44	Ti	Cr	Zr	Hf	W	4,8	2490	10,14	8,87	-7,75	4,30	
45	Ti	Cr	Zr	Ta	W	5,0	2647	10,81	6,78	-6,83	5,19	
46	Ti	Cr	Nb	Mo	Hf	5,0	2455	8,76	8,38	-4,83	6,81	
47	Ti	Cr	Nb	Mo	Ta	5,2	2611	9,43	4,90	-5,00	6,99	√
48	Ti	Cr	Nb	Mo	W	5,4	2692	9,95	4,33	-5,48	6,58	√
49	Ti	Cr	Nb	Hf	Ta	4,8	2533	10,04	7,95	-3,20	10,61	
50	Ti	Cr	Nb	Hf	W	5,0	2614	10,56	8,22	-5,89	5,94	
51	Ti	Cr	Nb	Ta	W	5,2	2771	11,22	4,79	-6,06	6,12	
52	Ti	Cr	Mo	Hf	Ta	5,0	2563	10,38	8,39	-4,89	7,02	
53	Ti	Cr	Mo	Hf	W	5,2	2644	10,90	8,54	-5,52	6,41	
54	Ti	Cr	Mo	Ta	W	5,4	2800	11,57	4,75	-5,23	7,16	
55	Ti	Cr	Hf	Ta	W	5,0	2722	12,17	8,22	-5,92	6,15	
56	Ti	Zr	Nb	Mo	Hf	4,6	2444	8,64	6,71	-1,50	21,85	
57	Ti	Zr	Nb	Mo	Ta	4,8	2601	9,30	4,58	-1,60	21,72	√

58	Ti	Zr	Nb	Mo	W	5,0	2682	9,82	5,01	-5,17	6,95	√
59	Ti	Zr	Nb	Hf	Ta	4,4	2523	9,91	5,38	2,66	12,70	√
60	Ti	Zr	Nb	Hf	W	4,6	2604	10,43	6,38	-3,13	11,15	
61	Ti	Zr	Nb	Ta	W	4,8	2761	11,10	4,23	-3,23	11,46	
62	Ti	Zr	Mo	Hf	Ta	4,6	2552	10,25	6,50	-1,84	18,62	
63	Ti	Zr	Mo	Hf	W	4,8	2633	10,77	7,24	-5,55	6,35	
64	Ti	Zr	Mo	Ta	W	5,0	2790	11,44	5,02	-5,19	7,19	
65	Ti	Zr	Hf	Ta	W	4,6	2712	12,05	6,14	-3,43	10,59	
66	Ti	Nb	Mo	Hf	Ta	4,8	2677	10,66	6,24	-1,21	29,66	
67	Ti	Nb	Mo	Hf	W	5,0	2758	11,18	6,73	-4,39	8,42	
68	Ti	Nb	Mo	Ta	W	5,2	2914	11,85	2,61	-5,11	7,63	
69	Ti	Nb	Hf	Ta	W	4,8	2836	12,46	5,93	-2,76	13,74	
70	Ti	Mo	Hf	Ta	W	5,0	2866	12,80	6,67	-4,37	8,78	
71	V	Cr	Zr	Nb	Mo	5,2	2427	7,72	7,44	-5,24	6,20	
72	V	Cr	Zr	Nb	Hf	4,8	2349	8,33	9,72	-4,68	6,73	
73	V	Cr	Zr	Nb	Ta	5,0	2506	9,00	7,49	-4,23	7,93	
74	V	Cr	Zr	Nb	W	5,2	2587	9,52	7,37	-6,16	5,62	
75	V	Cr	Zr	Mo	Hf	5,0	2379	8,67	10,09	-6,15	5,18	
76	V	Cr	Zr	Mo	Ta	5,2	2535	9,34	7,62	-5,25	6,47	
77	V	Cr	Zr	Mo	W	5,4	2616	9,86	7,35	-5,11	6,86	
78	V	Cr	Zr	Hf	Ta	4,8	2457	9,94	9,68	-4,96	6,63	
79	V	Cr	Zr	Hf	W	5,0	2538	10,46	9,95	-7,04	4,82	
80	V	Cr	Zr	Ta	W	5,2	2695	11,13	7,53	-6,13	5,88	
81	V	Cr	Nb	Mo	Hf	5,2	2503	9,08	9,11	-4,27	7,85	
82	V	Cr	Nb	Mo	Ta	5,4	2660	9,75	5,10	-4,45	8,00	√
83	V	Cr	Nb	Mo	W	5,6	2741	10,27	4,02	-3,77	9,73	
84	V	Cr	Nb	Hf	Ta	5,0	2582	10,36	8,96	-3,58	9,66	
85	V	Cr	Nb	Hf	W	5,2	2663	10,88	9,01	-5,12	6,96	
86	V	Cr	Nb	Ta	W	5,4	2820	11,54	5,09	-5,30	7,12	
87	V	Cr	Mo	Hf	Ta	5,2	2611	10,70	9,20	-4,23	8,26	
88	V	Cr	Mo	Hf	W	5,4	2692	11,22	9,13	-3,71	9,72	
89	V	Cr	Mo	Ta	W	5,6	2849	11,89	4,67	-3,43	11,13	
90	V	Cr	Hf	Ta	W	5,2	2771	12,49	9,09	-5,05	7,34	
91	V	Zr	Nb	Mo	Hf	4,8	2493	8,96	8,36	-2,34	14,24	
92	V	Zr	Nb	Mo	Ta	5,0	2649	9,62	6,12	-2,46	14,44	√
93	V	Zr	Nb	Mo	W	5,2	2730	10,14	6,16	-4,86	7,52	

94	V	Zr	Nb	Hf	Ta	4,6	2571	10,23	7,57	0,87	39,55	
95	V	Zr	Nb	Hf	W	4,8	2652	10,75	8,14	-3,76	9,45	
96	V	Zr	Nb	Ta	W	5,0	2809	11,42	5,92	-3,86	9,73	
97	V	Zr	Mo	Hf	Ta	4,8	2601	10,57	8,27	-2,58	13,47	
98	V	Zr	Mo	Hf	W	5,0	2682	11,09	8,70	-5,14	6,98	
99	V	Zr	Mo	Ta	W	5,2	2838	11,76	6,29	-4,79	7,93	
100	V	Zr	Hf	Ta	W	4,8	2760	12,37	8,03	-3,96	9,32	
101	V	Nb	Mo	Hf	Ta	5,0	2725	10,98	7,68	-1,89	19,32	
102	V	Nb	Mo	Hf	W	5,2	2806	11,50	7,88	-3,91	9,61	
103	V	Nb	Mo	Ta	W	5,4	2963	12,17	3,72	-4,64	8,54	
104	V	Nb	Hf	Ta	W	5,0	2885	12,78	7,49	-3,23	11,96	
105	V	Mo	Hf	Ta	W	5,2	2914	13,12	7,92	-3,79	10,28	
106	Cr	Zr	Nb	Mo	Hf	5,0	2492	9,16	9,11	-5,67	5,88	
107	Cr	Zr	Nb	Mo	Ta	5,2	2649	9,83	6,93	-5,58	6,36	
108	Cr	Zr	Nb	Mo	W	5,4	2730	10,35	6,89	-6,79	5,38	
109	Cr	Zr	Nb	Hf	Ta	4,8	2571	10,44	8,44	-3,43	10,05	
110	Cr	Zr	Nb	Hf	W	5,0	2652	10,96	8,91	-6,86	5,17	
111	Cr	Zr	Nb	Ta	W	5,2	2809	11,62	6,77	-6,76	5,56	
112	Cr	Zr	Mo	Hf	Ta	5,0	2600	10,78	9,03	-5,84	5,96	
113	Cr	Zr	Mo	Hf	W	5,2	2681	11,30	9,39	-7,21	4,98	
114	Cr	Zr	Mo	Ta	W	5,4	2838	11,97	7,03	-6,65	5,71	
115	Cr	Zr	Hf	Ta	W	5,0	2760	12,57	8,83	-7,00	5,28	
116	Cr	Nb	Mo	Hf	Ta	5,2	2724	11,19	8,40	-4,82	7,57	
117	Cr	Nb	Mo	Hf	W	5,4	2805	11,71	8,53	-5,64	6,65	
118	Cr	Nb	Mo	Ta	W	5,6	2962	12,38	4,64	-6,17	6,43	
119	Cr	Nb	Hf	Ta	W	5,2	2884	12,98	8,24	-5,93	6,51	
120	Cr	Mo	Hf	Ta	W	5,4	2913	13,33	8,58	-5,46	7,15	
121	Zr	Nb	Mo	Hf	Ta	4,8	2714	11,06	6,59	-1,13	32,16	
122	Zr	Nb	Mo	Hf	W	5,0	2795	11,58	7,31	-5,04	7,42	
123	Zr	Nb	Mo	Ta	W	5,2	2952	12,25	5,04	-5,50	7,18	
124	Zr	Nb	Hf	Ta	W	4,8	2874	12,86	6,24	-2,81	13,71	
125	Zr	Mo	Hf	Ta	W	5,0	2903	13,20	7,15	-5,13	7,57	
126	Nb	Mo	Hf	Ta	W	5,2	3027	13,61	6,71	-4,75	8,53	